Vibrational properties of

low-dimensional inorganic layered materials

vorgelegt von
Diplom-Physiker
Matthias Staiger
geboren in Filderstadt

von der Fakultät II - Mathematik und Naturwissenschaften
der Technischen Universität Berlin
zur Erlangung des akademischen Grades

Doktor der Naturwissenschaften
Dr. rer. nat.

genehmigte Dissertation

Promotionsausschuss:

Vorsitzender:	Prof. Dr. Michael Lehmann
Gutachter:	Prof. Dr. Christian Thomsen
	PD Dr. Tobias Korn

Tag der wissenschaftlichen Aussprache: 27.02.2017

Berlin 2017

Abstract

The family of low-dimensional inorganic layered materials covers a wide spectrum of properties, structurally and electronically. Ever since their synthesis as nanotubes and their preparation as mono- and few-layers these inorganic analogues to carbon nanotubes and graphene, respectively, have attracted a lot of interest both because of their importance for fundamental research as well as for their potential use in nanoelectronic applications.
In this thesis I aimed to get insight into the vibrational and electronic properties of low-dimensional transition metal dichalcogenides and their intercalation in misfit layer compounds. The experimental method of choice was Raman and Resonance Raman spectroscopy and research was greatly supported by electron microscopy characterization that allowed me to have precise structural information prior to Raman measurements. Case studies were performed on quasi zero-dimensional MoS_2 inorganic fullerene-like structures, quasi one-dimensional WS_2 and SnS_2 nanotubes, on quasi two-dimensional WS_2 and MoS_2 mono- and few-layers as well as on the intercalation and misfit layer $PbNbS_2$, SnS-SnS_2 and $(PbS)_{1.14}NbS_2$ nanotubes where boundaries between the different dimensionalities become blurred.
Despite the variety of materials, the Raman spectroscopic investigations performed in this thesis made evident that there are a few recurring fingerprint Raman features that allow to draw conclusions about the vibrational and electronic properties far beyond the focus of the case studies. Looking at the main out-of-plane mode in particular, by recording Resonance Raman profiles in the region of the A exciton, I was able to show for WS_2 nanotubes how the nanotube diameter affects the first optical transition energies by virtue of the changes in nanotube curvature with diameter. The Raman intensity ratio of a sideband to the out-of-plane mode was followed for different excitation energies and pressure and temperature changes and its development was proven to be due to slightly different resonance conditions of the two modes. The same out-of-plane mode and its sidebands were the main subject of my work on few-layer WS_2 where I established experimentally a "N modes for N layers" rule. I was able to trace back the appearance of formally infrared-active modes in the Raman spectra to the peculiar in-plane orientation of the A excitonic wavefunction in group VIB transition metal dichalcogenides.
In the investigated intercalation and misfit layer compounds the Raman features were shown to be composed of a superposition of Raman modes of their constituents. Here, the main out-of-plane mode was observed to barely change in comparison with the respective parent material. Instead, in $PbNbS_2$ and $(PbS)_{1.14}NbS_2$ nanotubes the in-plane modes were at the center of the Raman studies and seen to shift up drastically. The underlying reason for these shifts has to be found in the nature and strength of interlayer interactions and a range of mechanisms is discussed in the last part of my thesis. I was able to refute some of the common beliefs in trying to explain the unusual frequency shifts. I developed an approach that looks at the redistribution of charges in the intercalant layer during the vibrational displacement of atoms in the transition metal dichalcogenide layer that can serve as an alternative explanation for the hitherto unexplained phenomenon.

Kurzfassung

Ziel der vorliegenden Dissertation war es, genauere Einblicke in die Schwingungs- und elektronischen Eigenschaften niederdimensionaler Übergangsmetalldichalkogenide und aus ihnen gebildeter Misfitmaterialien zu erlangen. Dazu wurde als experimentelle Methode die Raman- und Resonanz-Raman-Spektroskopie gewählt, wobei die genaue elektronenmikroskopische Charakterisierung der Materialien vor der Aufnahme von Ramanspektren einen wesentlichen Teil am Forschungserfolg hatte. Als Fallstudien dienten quasi-nulldimensionale fullerenähnliche Strukturen aus Molybdändisulfid, quasi-eindimensionale WS_2- und SnS_2-Nanoröhren, quasi-zweidimensionale ein- und weniglagige Schichten aus Wolfram- und Molybdändisulfid sowie Dichalkogenidnanoröhren mit eingelagerten Atomen und in Form von Misfitschichten wie $PbNbS_2$, SnS-SnS_2 und $(PbS)_{1.14}NbS_2$, bei denen die Grenzen zwischen den Dimensionalitäten verschwimmen. Trotz der großen Bandbreite an untersuchten Materialien brachten die Ramanspektrokopischen Untersuchungen zutage, dass sich mit der Untersuchung einiger weniger wiederkehrender charakteristischer Ramanmoden weitreichende Aussagen über die Schwingungs- und elektronischen Eigenschaften treffen lassen. Einer Ramanmode, in der die Schwefelatome aus der Lagenebene herausschwingen (*out-of-plane*) galt besonderes Augenmerk: Bei der Analyse von Resonanz-Raman-Profilen von WS_2-Nanoröhren verschiedenen Durchmessers konnte ich zeigen, auf welche Weise die Dicke der Nanoröhren Auswirkungen auf die Energie der ersten optischen Übergänge hat und die Abhängigkeit auf die unterschiedliche Stärke der Kurvatur in den einzelnen Nanoröhrenlagen zurückführen. Desweiteren gelang es mir nachzuweisen, dass die Veränderung der relativen Intensität einer Nachbarmode zur eben beschriebenen Hauptmode in Abhängigkeit von Anregungsenergie, Temperatur und Druck jeweils der Tatsache geschuldet ist, dass für die benachbarten Moden in Nanoröhren leicht unterschiedliche Resonanzbedingungen gelten. Dieselbe Haupt- und Seitenmode lag im Fokus meiner Arbeit an weniglagigem WS_2, bei der ich eine „N Moden für N Lagen“-Regel etablieren konnte. Es gelang mir das Auftauchen formal infrarotaktiver Moden in den Ramanspektren durch die besondere Orientierung der Wellenfunktion des A-Exzitons in der Ebene der WS_2-Lagen zu erklären.
Die Ramanmoden in den untersuchten Misfitmaterialien setzen sich aus einer Überlagerung der Schwingungsmoden der einzelnen Materialbausteine zusammen. Während sich die *out-of-plane*-Mode in den Kompositmaterialien im Vergleich zu dem jeweiligen Elternmaterial kaum verändert zeigte, galt das Augenmerk hier den *in-plane*-Moden, bei denen die Schwingungsrichtung der Schwefelatome innerhalb der Lagenebene liegt. Speziell in $PbNbS_2$- und $(PbS)_{1.14}NbS_2$-Nanoröhren konnte ich eine drastische Erhöhung der Ramanfrequenz im Vergleich zu NbS_2 feststellen. Der zu Grunde liegende Mechanismus für das ungewöhnlich starke Ausmaß der Verschiebung ist in der Stärke und der Natur der elektronischen Wechselwirkung der Lagen untereinander zu suchen. In der Literatur findet sich eine Vielzahl an möglichen Erklärungsansätzen, die ich im abschließenden Teil der vorliegenden Dissertation diskutiere und teilweise widerlege. Ich schlage einen alternativen Mechanismus vor, der den Ursprung in der Umverteilung der Ladungen innerhalb der interkalierten Lagen während der Schwingungsvorgänge innerhalb der Übergangsmetalldichalkogenidlagen sucht.

List of publications

1. *Excitonic resonances in WS_2 nanotubes.*
M. Staiger, P. Rafailov, K. Gartsman, H. Telg, M. Krause, G. Radovsky, A. Zak, and C. Thomsen
Physical Review B **86**, 165423 (2012)
DOI: https://doi.org/10.1103/PhysRevB.86.165423

2. *Splitting of monolayer out-of-plane A_1' Raman mode in few-layer WS_2.*
M. Staiger, R. Gillen, N. Scheuschner, O. Ochedowski, F. Kampmann, M. Schleberger, C. Thomsen, and J. Maultzsch
Physical Review B **91**, 195419 (2015)
DOI: https://doi.org/10.1103/PhysRevB.91.195419

3. *Raman spectroscopy of intercalated and misfit layer nanotubes.*
M. Staiger, V. Bačić, R. Gillen, G. Radovsky, K. Gartsman, R. Tenne, T. Heine, J. Maultzsch and C. Thomsen
Physical Review B **94**, 035430 (2016)
DOI: https://doi.org/10.1103/PhysRevB.94.035430

4. *Interlayer resonant Raman modes in few-layer MoS_2.*
N. Scheuschner and R. Gillen and M. Staiger, and J. Maultzsch
Physical Review B **91**, 235409 (2015)
DOI: https://doi.org/10.1103/PhysRevB.91.235409

5. *Electronic structure tuning of diamondoids through functionalization.*
T. Rander, M. Staiger, R. Richter, T. Zimmermann, L. Landt, D. Wolter, J.E. Dahl, R.M.K. Carlson, B.A. Tkachenko, N.A. Fokina, P.R. Schreiner, T. Möller, and C, Bostedt
The Journal of Chemical Physics **138**, 024310 (2013)
DOI: http://dx.doi.org/10.1063/1.4774268

6. *Chiral index dependence of the G^+ and G^- Raman modes in semiconducting carbon nanotubes.*
H. Telg, J.G. Duque, M. Staiger, X. Tu, F. Hennrich, M.M. Kappes, M. Zheng, J. Maultzsch, C. Thomsen, and S.K. Doorn
ACS Nano **6**, 904-911 (2012)
DOI: https://doi.org/10.1021/nn2044356

7. *Synthesis of copious amounts of SnS_2 and SnS_2/SnS nanotubes with ordered superstructures.*
G. Radovsky, R. Popovitz-Biro, M. Staiger, K. Gartsman, C. Thomsen, T. Lorenz, G. Seifert, and R. Tenne
Angewandte Chemie International Edition **50**, 21316-12320 (2011)
DOI: https://doi.org/10.1002/anie.201104520

8. *The influence of a single thiol group on the electronic and optical properties of the smallest diamondoid adamantane.*
L. Landt, M. Staiger, D. Wolter, K. Klünder, P. Zimmermann, T.M. Willey, T. van Buuren, D. Brehmer, P.R. Schreiner, B.A. Tkachenko, A.A. Fokin, T. Möller, and C. Bostedt
The Journal of Chemical Physics **132**, 024710 (2010)
DOI: http://dx.doi.org/10.1063/1.3280388

9. *Intrinsic photoluminescence of adamantane in the ultraviolet spectral region.*
L. Landt, W. Kielich, D. Wolter, M. Staiger, A. Ehresmann, T. Möller, and C. Bostedt
Physical Review B **80**, 205323 (2009)
DOI: https://doi.org/10.1103/PhysRevB.80.205323

Contents

1 Introduction

This thesis focuses on a family of layered materials that can be described by the chemical formula $T\mathrm{S}_2$. Here, T is either a transition metal (Ti, Nb, Cr, Mo, W...) or the main group metal Sn, and S denotes sulfur atoms. They form sandwich-like layered structures with metal cations surrounded by sulfur anions. These trilayers extend in two dimensions and are stacked upon each other in the third dimension, forming three-dimensional layered compounds. There are two main structure polytypes within a trilayer (trigonal prismatic H type and octahedral T type) and different stacking types of adjacent layers are possible. Because the covalent or ionic bonding arrangement within each trilayer is much stronger than the weak interlayer forces that are mostly of van der Waals character, many of the physical properties of the $T\mathrm{S}_2$ materials are extremely anisotropic.

Despite their chemical structure being all but complicated, the $T\mathrm{S}_2$ materials cover the whole world of electronic properties ranging from insulators (HfS_2), semiconductors (MoS_2, SnS_2) and semimetals (TiS_2) to metals (NbS_2). All the transition metal dichalcogenides (TMDs) possess nonbonding d orbitals that play a decisive role in determining the basic physical properties. In particular, it is is the d_{z^2} orbital that is successively filled in the group IVB to VIB transition metal dichalcogenides. While the group VB TMDs are metals, the group VI TMDs are of semiconducting nature and many of their electronic properties are governed by excitons.

Structurally, the interplay between strong intralayer bonding and weak interlayer interaction in layered $T\mathrm{S}_2$ has three main consequences. It is possible to peel off individual layers by mechanical exfoliation and study the physical properties depending on the number of layers. Secondly, under certain conditions, the layers will bend and form multiwalled nanotubes or inorganic fullerenes with a hollow core. Thirdly, the van der Waals gap is able to accommodate guest atoms or molecules. They can formally be described as intercalants of the host $T\mathrm{S}_2$ layer and form ordered structures in between layers. A particular case are the so-called misfit layer compounds (MLCs) that are built of alternately stacked layers of $T\mathrm{S}_2$ and cubic monochalcogenide layers $M\mathrm{S}$ (with M a metal). The name MLC stems from the fact that the ratio of at least one of the in-plane lattice constants of the two materials is irrational. Therefore, the layers exhibit a certain mismatch and the translational symmetry of the pure $T\mathrm{S}_2$ compound is broken. Electronically, these compounds can be described, to a first approximation, by the rigid band model that constructs the band structure by a simple superposition of the band structures of

the subsystems. Apart from the system SnS-SnS_2, in the transition metal dichalcogenides, an empty or partly filled metal d_{z^2} orbital appears to be a necessary condition for the formation of a MLC, as group VI TMDs are not known to form any. But whether it is a charge transfer mechanism from the MS to the TS$_2$ layers or any other type of interlayer interaction that can account for the remarkable stability of MLCs is still under debate.

Raman spectroscopy and Resonance Raman spectroscopy have been the experimental methods of choice to study the vibrational and electronic properties of the nanostructures described above. Thereby, monochromatic laser light is focused onto the sample and inelastically scattered by electrons while in the process a quantized portion of energy, a phonon, is created or annihilated. These phonons correspond to atomic vibrational modes and are highly characteristic of the material, its composition and symmetry. Any structural change, be it different dimensionality, stacking type, defects or the combination with other materials will have direct repercussions in the Raman spectra as well as any outside influence such as strain or changes in temperature and pressure. Moreover, whereas normally the electrons excited by the incoming light reach only virtual intermediate states, as soon as the exciting radiation has approximately the same energy as a real transition in the investigated material, the Raman scattering cross section is greatly enhanced. This Resonance Raman process allows one to follow the band structure of a material by scanning a large excitation energy region, and it represents the most obvious connection between vibrational and electronic properties. On the other hand, knowing the optical transition energies of the investigated materials, allows for a careful selection of laser excitation energies to extract maximum signal and to access the specific information Resonance Raman spectra have to offer. The laser systems used in this thesis include a laser diode emitting at 457 nm, a frequency doubled Nd:YAG laser emitting at 532 nm, a HeNe laser at 632 nm, the laser lines of the ArKr laser system, a dye laser system with variable excitation wavelength in the red, and a TiSa laser emitting in the red and near infrared. Thus, basically the entire visible light region of the electromagnetic spectrum is covered.

The analysis of the Raman spectra was greatly supported by the characterization methods employed prior to Raman measurements providing high-accuracy knowledge about the nanotubes' structural properties. Inorganic nanotubes and misfit layer nanotubes were synthesized in the group of Prof. Reshef Tenne of the Weizmann Institute of Science in Israel. They were individually placed on substrates and characterized by scanning electron microscopy (SEM), transmission electron microscopy (TEM), high-resolution TEM (HRTEM), electron diffraction (ED) and energy-dispersive X-ray spectroscopy (EDS), depending on the specific experimental requirements. Few-layer WS_2 samples were supplied by the group of Prof. Schleberger in Duisburg, Germany, via the mechanical exfoliation method. Individual layer numbers were identified under the optical microscope and confirmed by atomic force microscopy. Additionally, density functional theory (DFT) calculations performed in my group and in the group of Prof. Heine of the Jacobs University, Bremen, were of great help in getting insight into the layer-dependent Raman mode splitting in few-layer WS_2 and the possible interlayer interaction mechanisms in misfit layer compounds.

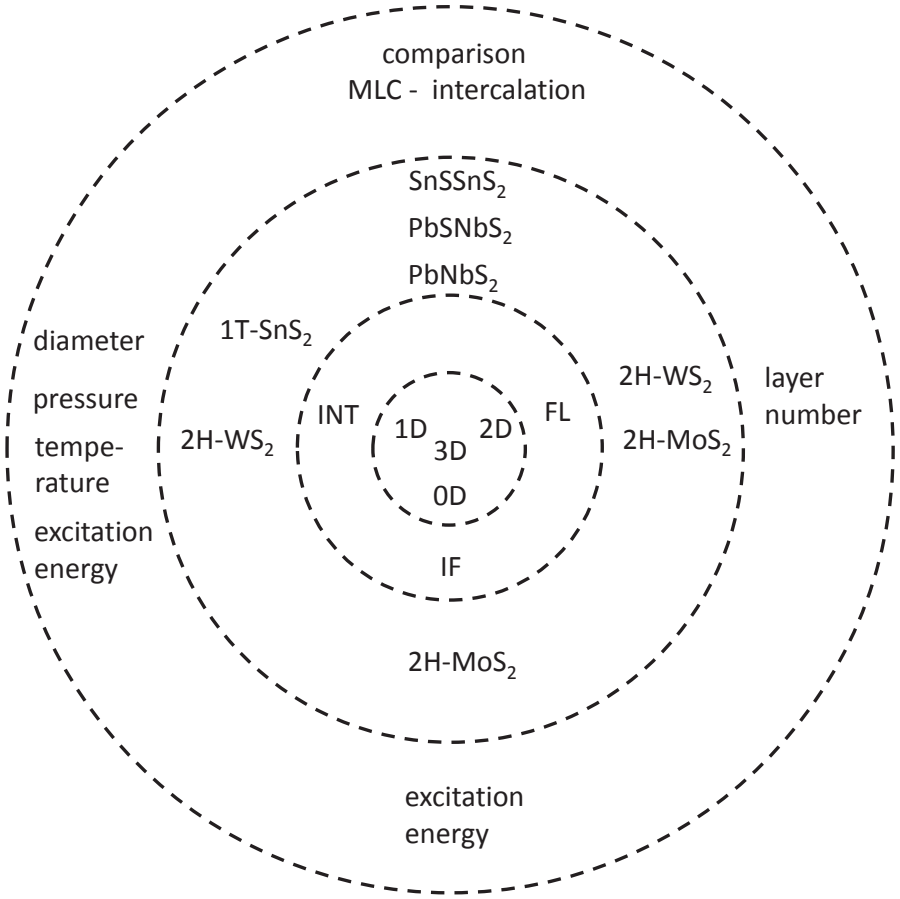

Figure 1.1.: Overview of the materials investigated in this thesis, their structural connection and the focus of the experimental studies.

Shown in Fig. 1.1. is an overview of the materials investigated in this thesis and their structural connection. Principally, nanomaterials can have any dimensionality and at least one member of every dimensionality has been focus of research in this thesis. The innermost circles of Fig. 1.1. denote the general terms for the different dimensionalities - quasi zero-dimensional inorganic fullerene-like nanoparticles (IFs), quasi one-dimensional inorganic nanotubes (INTs) and quasi two-dimensional few-layer transition metal dichalcogenides (FLs), with studies always using the three-dimensional (quasi) bulk structures for comparison. The next segment names the particular materials investigated, with WS_2 nanotubes certainly taking center stage. In the outermost circle segment the respective focus of research is listed.
For WS_2 nanotubes, it was shown that the impact a change of a variety of experimental parameters has on the vibrational properties can all be discussed on the basis of the same underlying mechanism. Namely, an alteration of optical transition energies under any outside influence and slightly different resonance conditions for the two main out-of-plane Raman modes as the Raman fingerprint region chosen in all of the studies. As an extension to the work on WS_2 nanotubes, it was shown that just like nanotube curvature reduces the first optical transition energy with respect to the bulk material, so does the curvature of layers in IF-MoS_2. Expanding research

into the field of planar layered structures, where dimensionality has been found to determine whether WS_2 and MoS_2 are indirect or direct band gap semiconductors, and being aware of the specific information Resonance Raman spectra have to offer, the out-of-plane modes were once again in the focus of attention during work on FL-WS_2. Here, and in FL-MoS_2 as well, Raman spectra were found to contain information about the characteristics of the excitons the phonons couple to in the resonant case.

There are two main polytypes in layered (transition) metal dichalcogenides (TMDs), commonly denoted by the prefix $2H$ and $1T$, and pristine INTs, $2H$-WS_2 and $1T$-SnS_2 NTs, respectively, of both types have been investigated in this thesis. For the later work on misfit layer compounds (MLCs) this was of advantage, as their Raman spectra can be discussed on the basis of the Raman spectra of their constituents. Raman spectroscopy on both $2H$-derived NbS_2 and $1T$-derived SnS_2 MLC nanotubes, was carried out in the course of the present thesis with the scientific focus on the comparison with the respective parent bulk structures on the one hand and NbS_2 nanotubes intercalated with lead atoms on the other hand. Misfit layer nanotubes represent an interesting mix of different dimensionalities with their alternate stacking of quasi two-dimensional TS_2 and MS layers and their rolling-up to large diameter nanotubes that closely resemble the three-dimensional bulk misfit structures. Interlayer interaction as a basic factor stabilizing all of the layered inorganic materials has influence on the vibrational characteristics in the pristine compounds, for instance in different layer number FL-WS_2, despite being of weak van der Waals character. In misfit layer compounds interlayer interaction determines the vibrational frequencies in an unprecedented way and models explaining the remarkable changes in Raman frequencies have to go well beyond the simple van der Waals bonding.

The outline of this thesis is as follows. I will first introduce the basic structural properties of the inorganic layered materials, their combination in misfit layer compounds and the specifics of their appearance as nanotubes in Chapter 2. Then, I will concentrate on the electronic properties of above named compounds in Chapter 3. Knowledge of both, structural and electronic characteristics and their interplay were of vital importance for the papers forming this thesis that are listed in Chapter 4. Their connection and scientific output is discussed in Chapter 5 with the focus on the vibrational properties as the main topic of my work on low-dimensional inorganic layered materials. An outlook summarizing the results and presenting perspectives of future work on these kind of nanostructures concludes this thesis in Chapter 6.

2 Structural properties

2.1. Structure of layered materials

The TS_2 layers

The structure of a layered compound is defined by the coordination of atoms within a layer and by how these layers as a whole are arranged with respect to each other. The formula TX_2 comprises compounds where in each trilayer the (transition) metal atom T is coordinated by three chalcogen X atoms above and below that form the base of two tetrahedrons with the T atom in the middle layer as the tip. Because almost all research is performed on compounds containing sulfur, in this thesis I will mostly speak of TS_2 compounds. In the trigonal prismatic coordination the tetrahedrons have the sulfur atoms within one layer on top of each other, while in the octahedral coordination they are rotated by 60° with respect to each other. The corresponding structural abbreviations are *AbA* and *AbC* (where A and C denote sulfur layers and b the metal atoms) [1], respectively, and both types are shown in Fig. 2.1. Typical examples of trigonal prismatic arrangement (H type) within a metal dichalcogenide layer are MoS_2, WS_2 and NbS_2, whereas e.g. TiS_2 and SnS_2 layers crystallize in the octahedral coordination (T type). The octahedrally coordinated layers commonly obey the simplest possible stacking order: the unit cell of $1T$-TS_2 is only one layer thick and individual layers are placed exactly on top of each other (*AbC AbC*) [Fig 2.1.(a)]. In contrast, the hexagonal $2H$ trigonal prismatic stacking order has its unit cell spanning over two layers [Fig 2.1.(b)]. Consequently, in the rhombohedral $3R$ stacking the sequence of layers is repeated only every three layers. The $2H$ structure has two sub-polytypes that are important to discuss here. In the $2H_a$ structure (e.g. NbS_2) the metal atoms are found on top of each other, but the tetrahedrons from neighboring layers are rotated by 60° (*AcA BcB*). The $2H_b$ structure (e.g. WS_2) has an additional in-plane shift of layers, meaning that metal atoms are found above and below sulfur atoms of adjacent layers. Again, this is illustrated in Fig. 2.1.(b). There is only one $3R$ polytype (*AbA BcB CaC*) for both WS_2 and NbS_2. Without going further into detail concerning the symmetry of the investigated materials, in the Schönfliess notation the space groups of the $1T$ compounds are D_{3d}^3 for the bulk and an unchanged point group symmetry D_{3d} in the individual layers, the $2H$ materials possess D_{6h}^4 symmetry in the bulk and D_{3h} in the monolayer.

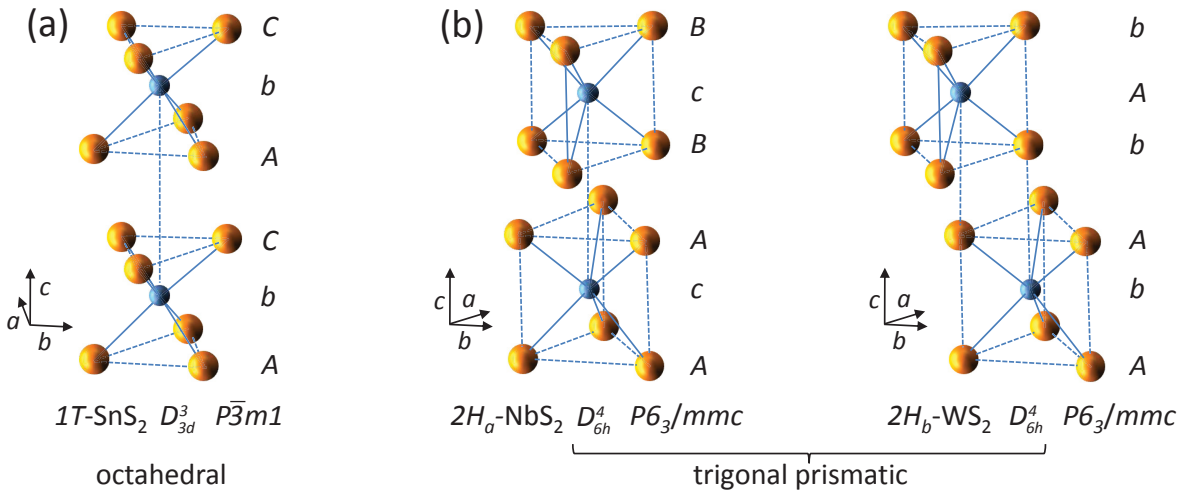

Figure 2.1.: Basic structures of transition metal dichalcogenides. (a) Structure of TMDs in octahedral coordination ($1T$); the unit cell is one triple layer thick. (b) The two types of TMDs in trigonal prismatic coordination ($2H$) with the unit cell spanning over two triple layers. The space groups of the bulk structures are denoted below the compounds, the stacking arrangements are found in italic letters on the right side of the TMDs.

As a consequence of rather weak interlayer interaction, there is the occasional problem of nonstoichiometry particularly for $3R$-NbS_2 [2, 3], with additional Nb atoms found in the van der Waals gap. More importantly, however, intercalation of metal dichalcogenides with atoms, organic molecules or other types of layered materials is widespread.

The MS layers

One class of materials that can be found as guest layers in between host TS_2 layers are cubic monochalcogenides. The general formula MX with M a metal or a rare earth element and X a chalcogenide describes a two atom thick layer cut out from the (001) plane of a (hypothetical) three-dimensional NaCl-type structure. Lead monosulfide is one example of such an intercalant. PbS (Galena) occurs in nature as a three-dimensional crystal with NaCl structure. Its appearance as a MS double layer (half the thickness of a NaCl unit cell) is only reported as an intercalant of TX_2 transition metal dichalcogenides and results in strong distortion compared to the bulk structure. Recent HRTEM (high resolution transmission electron microscopy) investigations [4] are able to show, down to a few picometres, how the lead atoms of PbS in the misfit layer compound are always closer to the neighboring TS_2 layer than its sulfur atoms. Tin sulfide, as another example, has in its pristine form a layered α-phase with GeS structure and an orthorhombic (pseudo-tetragonal highly distorted NaCl) unit cell [5, 6]. In misfit layer compounds (MLCs), however, it is found to adopt a structure similar to the lead sulfide part in PbS-based MLCs [7, 8].

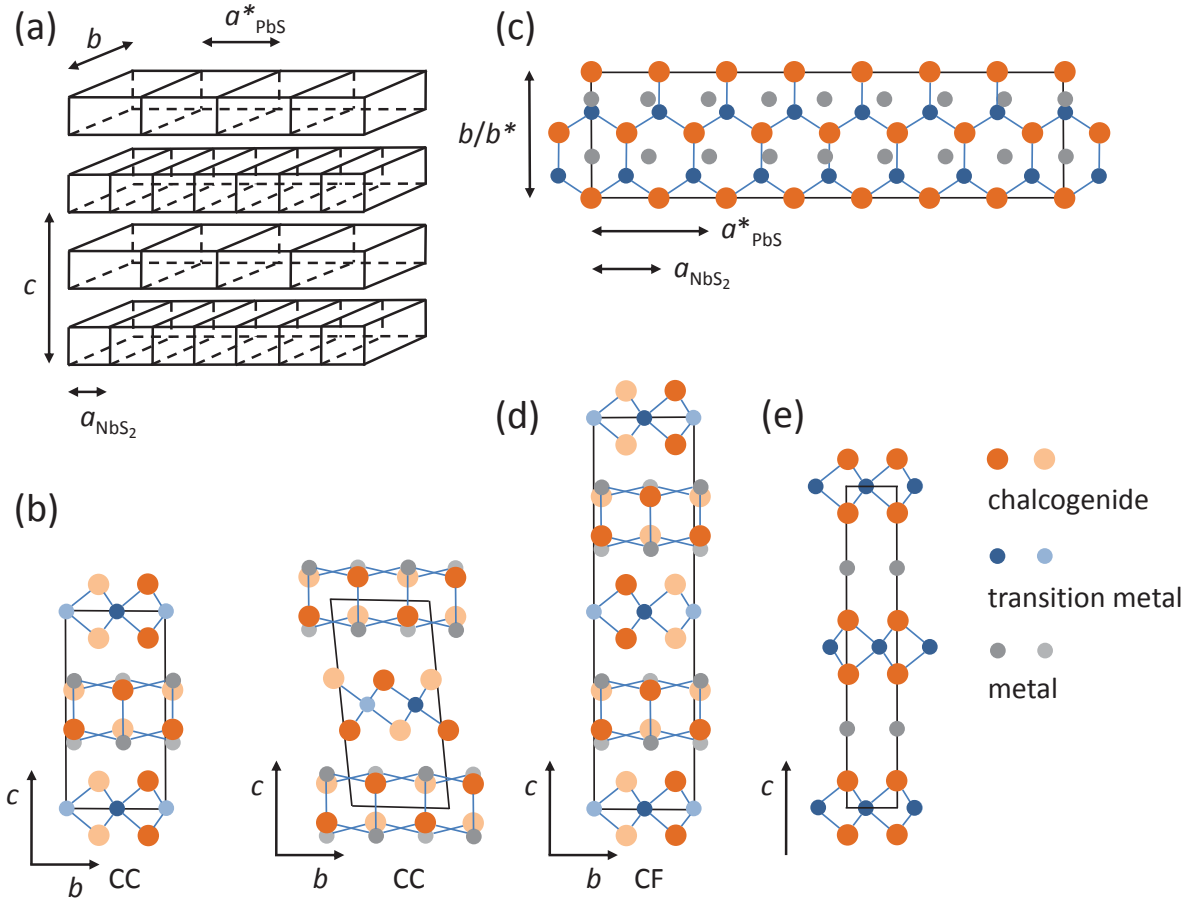

Figure 2.2.: Basic structure of MLC (adapted from Refs. [9, 10]). (a) Sketch of the basic alternate stacking of MX and TX_2 layers in $(PbS)_{1.14}NbS_2$ along a common c direction with a commensurate b and incommensurate a lattice constants. (b) Simple CC stacking sequence for TMDs in trigonal prismatic (left) and octahedral (right) coordination. (c) CF stacking sequence adopted for example by the $(PbS)_{1.14}NbS_2$ compound, seen along the stacking c direction. The sulfur atoms of the PbS part are omitted for clarity. (d) The CF stacking sequence seen along the incommensurate a direction.(e) Basic structure of the intercalation compound $PbNbS_2$. View along the normal to the (11.0) plane according to the pseudohexagonal system of labeling of the NbS2 material intercalated with lead atoms in linear coordination to neighboring S atoms (ICSD col. code. 74698). Panels (b)-(e): different colors of the same element represent atomic positions half a lattice constant apart, the black lines refer to the size of the unit cell.

2.2. The misfit layer compounds

When the two subsystems described above, the TS_2 trilayers and the MS double layers, are combined, the structure that follows is commonly termed a misfit layer compound (MLC). $(PbS)_{1.14}NbS_2$ and the SnS-SnS_2 system are two MLCs that have been studied in the course of this thesis. Exemplary MLC structures are shown in Fig. 2.2. Some of the structural parameters discussed below are presented in Table 1. In these compounds, the TS_2 and MS layers share

compound		a (Å)	b (Å)	c (Å)
2H-NbS		3.324 [12]	5.757 [12]	11.89 [1]
PbS		5.936 [12]	5.936 [12]	5.936
$(PbS)_{1.14}NbS_2$	NbS_2	3.313 [8, 12]	5.801 [8, 12]	23.807 [13] (CF structure)
	PbS	5.834 [8, 12]	5.801 [8, 12]	11.90 [13]
$PbNbS_2$		3.343 [14]	3.343 $\sqrt{3}$	17.73 [14]
$(SnS)_{1.17}SnS_2$	SnS_2	3.6486 [15]	3.6486 $\sqrt{3}$	5.8992 [15]
	SnS	5.673 [8]	5.751 [8]	11.761 [8]
$(PbS)_{1.18}TiS_2$	TiS_2	3.409 [16]	5.881 [16]	11.76 [16] (CC structure)
	PbS	5.800 [16]	5.881 [16]	11.76 [16]

Table 2.1.: Crystal data for misfit layer compounds relevant for this thesis. Cell parameters for the TS_2 part of the structures are given for an orthohexagonal unit cell. For the $(PbS)_{1.14}NbS_2$ misfit compound it is listed in an exemplary way how the cell parameters are altered with respect to the parent materials. As there is no comprehensive structural data for the SnS-SnS_2 misfit system values are given for pure 1T-SnS_2 and SnS in $(SnS)_{1.17}NbS_2$.

a common c axis and are stacked alternately. Naturally, the in-plane lattice constants of the subunits are not necessarily the same and therefore the index in the structural formula differs from one but instead describes the irrational ratio of the crystal units of the subsystems in the MLC. In the pseudohexagonal unit cell of TS_2 compounds the two in-plane lattice parameters are equal to one another and share an angle of 120°. Because the MS layer has lattice parameters orthogonal to each other, in the MLC it is convenient to define an orthohexagonal unit cell for the TS_2 layer to be able to have parallel a/a^* and b/b^* directions for the TS_2 and MS subunits, respectively. The b axis is then orthogonal to the a axis and defined as $b = a\sqrt{3}$. In most misfit layer compounds, the b^* lattice parameter of the MS layer is made to adopt the structure of the host layer so that the b lattice constants are commensurate. In both trigonal and octahedral coordination of the TX_2 layer, the b direction of the unit cell comprises two units of each subsystem and the M atoms are found always in between sulfur atoms of the adjacent layer, principally allowing interlayer bonding [11]. The a lattice constants stay incommensurate and a sketch of an exemplary $(PbS)_{1.14}NbS_2$ system with an a lattice ratio of approximately 7/4 [12] is shown in Fig. 2.2.(a). In Fig. 2.2.(b) the most simple stacking sequence of the two building units are shown with the dichalcogenide layer in the trigonal prismatic (left) and octahedral coordination (right). In the former, layers repeat identically along the c direction, for the latter, rows of chalcogen atoms are displaced in the MLC by $1/6b$ [11], so that the c axis is not orthogonal to the in-plane lattice constants as in the trigonal prismatic compounds, but the angle is bigger than 90°. For CF/FC stacking only the MS/TS_2 units repeat and in the FF stacking both sublayers repeat only every two layers.
The appearance of these different stacking sequences means that the $2H_a$ and $2H_b$ stacking types of the pure TS_2 parent compounds are no longer valid in the MLCs. As a representative of the

CF stacking sequence, the structure of bulk $(PbS)_{1.14}NbS_2$ is depicted in a top-view on the ab-plane in Fig. 2.2.(c) and along the incommensurate a direction in Fig. 2.2.(d). The mismatch of the two materials is expressed in the general structure formula of misfit layer compounds $(MX)_{1+\delta}(TX_2)_n$ as the parameter $1+\delta$ with $\delta = 1 - \frac{a}{a^*/2}$ [17]. This takes into account that the a^* lattice constant of the MX material spans across two formula units. The two extreme cases for the parameter δ are represented by $(YS)_{1.28}CrS_2$ [18] and $(BiS)_{1.08}TaS_2$ [19]. The additional parameter n denotes the number of TX_2 slabs in between MX slabs and takes values between $n = 1$ (*stage 1* MLC [20]) and $n = 3$ (*stage 3* MLC). The influence that the two materials exert on each other when combined to a misfit layer compound has been widely discussed with drastically differing results (see Chapter 3). Structurally, though, it is evident from a number of experiments that the TX_2 layer remains fairly rigid [8], while the MX layer exhibits strong distortion beyond the fact that it is in a very unusual two-dimensional configuration with every atom being a surface atom [4]. Not only has the b^* lattice constant to adopt the b lattice constant of the TX_2 slab, it is also observed that the M atoms always protrude into the van der Waals gap [4], probably owing to the presence of a lone pair of electrons.
Even though it is not a misfit layer compound but a true intercalation compound, the unusual structure of $PbNbS_2$ shall be mentioned here. In most cases, atoms intercalated in transition metal dichalcogenides will fill the interstices of the sulfur atoms resulting in structures like $Pb_{1/3}TX_2$ [14]. In $PbNbS_2$ however, lead atoms are linearly coordinated by neighboring sulfur atoms, see Fig. 2.2.(e) [14].

2.3. Structure of inorganic nanotubes

Pristine inorganic nanotubes

A report on inorganic nanotubes never misses to reference carbon nanotubes (CNTs) as the material whose discovery in 1991 [21] laid the foundation of an entirely new research area. Shortly after, in 1992, Reshef Tenne and coworkers [22] synthesized tubular structures of WS_2 as the first member of the ever since growing family of inorganic nanotubes. The following paragraphs will concentrate on WS_2 and SnS_2 nanotubes in particular, a comprehensive list of inorganic nanotubes that have been synthesized during the last two decades can be found in Ref. [23].
Being an inorganic analogue to carbon nanotubes, WS_2 nanotubes are hollow cylindrical structures with a large length to diameter ratio, made of several rolled-up S-W-S triple layers. In fact, it can be shown that, above a critical diameter threshold, the annihilation of dangling bonds on the rim of multilayer WS_2 stripes by spontaneous bending is energetically preferred to the strain energy associated with the bending of the nanotube walls [24]. Obviously, there is a higher strain energy involved in the bending of a WS_2 layer than in graphene sheets that form the basis for the formation of carbon nanotubes. Consequently, in contrast to CNTs, the diameters of WS_2 nanotubes are never in the subnanometer regime, but cover a wide diameter range starting with a lower limit of the inner diameter of around 4 nm [22]. The always multiwalled form of

WS_2 and other inorganic nanotubes appears to be another stabilization criterion. Individual WS_2 nanotubes with less than 4 walls have not been observed so far [24], typically the number of walls amounts to 10-50, outer diameters range from 7 to 290 nm and lengths are hundreds of nanometer to several micrometers [22, 24–27]. Structurally, a lot depends on the synthesis method and growth conditions and, using techniques such as transmission electron microscopy (TEM), high resolution TEM (HRTEM), X-ray diffractometry (XRD), electron diffraction (ED) and theoretical modeling, a plethora of different subtypes has been revealed on the atomic level. For example, Remškar *et al.* [28–31] report on nanotubes that are formed by the continuous spiral winding of one single molecular WS_2 layer around the tube axis and can be more accurately described as nanoscrolls. Others find nanotubes where the shells grow separately, possibly using one original shell as a growth template [32, 33], in a coaxial, russian doll-like fashion. Whereas nanotubes with diameters up to 30 nm have been shown to possess a near perfect cylindrical cross section [25, 34], thicker nanotubes adopt a polygonal cross section [31, 34] that is predicted to be energetically more favorable [35]. The nanotubes are either open-ended [31] or have closed caps that exhibit a large number of possible angles with most of them identical with angles occurring in regular polygons [36]. Almost round caps are seen predominantly in small diameter nanotubes [22] while 90° angles have been observed in thicker WS_2 nanotubes [34]. The tube diameter also plays a role in determining the stacking order of subsequent WS_2 walls. The stacking can be investigated by either ED patterns [36] or HRTEM on the atomic level [37]. There are reports that conclude that the hexagonal $2H_b$ stacking type predominates for nanotube diameters up to 200 nm while for larger microtubes the rhombohedral $3R$ stacking type has been identified [29]. However, as Ref. [37] rightly points out, statements on a specific bulk derived stacking order have to be taken with caution and a more or less random stacking order seems to be more likely. To begin with, with each shell the tube circumference is enlarged by $2\pi c_0$, where $c_0 = c/2$ is half the c lattice constant perpendicular to the tube axis (the factor two is included because, in the bulk structure, the unit cell stretches out over two triple layers). In order to satisfy a strict bulk pattern, this parameter would need to be an integer multiple of the in-plane lattice parameter in winding direction [30]. In comparison with the $c/2$ lattice parameter of the pristine WS_2 crystal (0.6181 nm [1]) the wall thickness is seen to be slightly expanded in the WS_2 nanotubes [36, 38, 39] and is not a multiple of the in-plane lattice constant a of 0.3154 nm [1]. Secondly, contradicting evidence is also presented concerning a central question that also influences the lattice matching of adjacent layers: the chirality of the tube walls. Similar to carbon nanotubes the direction of the rolling-up of molecular layers can be characterized by a chirality vector $\vec{c} = n_1\vec{a}_1 + n_2\vec{a}_2$, with the two in-plane basis vectors $\vec{a}_1$ and $\vec{a}_2$ sharing an angle of 60° and the two chiral indices (n_1,n_2) having to be integer numbers. Due to their respective appearance on the rim (n_1,0) nanotube walls are called zigzag with a chiral angle of 0° and (n_1,$n_2 = n_1$) nanotubes are called armchair, while every other pair of chiral indices characterizes chiral nanotube walls. Considering the spiral winding growth mode one can assume that there is either only one chiral angle present in these nanotubes or, under the influence of internal strain, several with very similar chiral angles [30]. In the coaxial-cylindrical

growth mode, apart from one report that observed achiral armchair walls [32], the majority of authors find nanotubes with small chiral angles towards the zigzag character and a deviation of only a few degrees from one wall to another or pure zigzag walls [27, 32, 33, 36, 38, 40]. It can generally be stated that, despite the fact that there is considerable strain involved in the bending of the nanotube walls, with the inner sulfur layer experiencing compressive and the outer sulfur layer tensile stress with respect to the tungsten layer in the middle, WS_2 nanotubes possess a remarkable degree of structural uniformity with most of the walls appearing almost defect free.

While the layers in WS_2 nanotubes are in trigonal prismatic coordination, the SnS_2 nanotubes investigated in this thesis are an example of inorganic nanotubes with layers in the octahedral coordination. Although short, tubular-like SnS_2 structures [41] and small amounts of SnS_2 nanotubes [42, 43] have been synthesized before, a detailed analysis of $1T$-SnS_2 nanotubes was first presented by Radovsky *et al.* [5]. The nanotubes are straight and TEM images show evenly spaced fringes with an interlayer distance of 0.59 nm, corresponding to the c lattice parameter of bulk $1T$-SnS_2 (Berndtite) [44]. From the splitting of reflection spots in the measured diffraction patterns the almost monohelical nature of the walls of an exemplary SnS_2 nanotube and a small chiral angle of around 4° was derived [5]. Even the nanotubes characterized as pure SnS_2 include some layers of SnS mostly close to the hollow core of the nanotube that form an ordered SnS-SnS_2 superstructure. The vast majority of nanotubes containing tin can be characterized as misfit layer nanotubes with a variety of ordered stacking sequences of SnS and SnS_2 slabs. This SnS-SnS_2 system as well as the PbS-NbS_2 system also investigated in this thesis shall be examined in more detail in the next section.

Misfit layer inorganic nanotubes

Misfit structures have been known to form fullerene-like and tubular morphologies on the nanometer scale for quite some time and in recent years a number of compounds have been added to a now extensive list of inorganic misfit layer nanotubes [45]. It was mentioned before that for pure inorganic nanotubes the main driving force for bending is the energetic advantages of a healing of dangling bonds on the periphery of the planar layers. Here, in misfit layer compound nanotubes, the intrinsic stress associated with the mismatch of neighboring layers has been established as an additional mechanism that promotes the rolling-up of layers [5, 12]. It is assumed that the relaxation of misfit stress by folding of layers occurs predominantly for asymmetric lamellae, that is, if top and bottom layer are of different material [12]. Naturally, the favored rolling vector will be in the direction the lattice constants of the subsystems differ the most, the incommensurate a direction. Thus, the tube axis is expected to coincide with the commensurate b direction (for a definition of the lattice axes, see previous section) [7]. However, as we will see, the individual layers do not always obey these rules and they can merely be seen as a general trend. Compared to pristine inorganic nanotubes the diameters of misfit layer NTs are larger in average, most probably due to the higher rigidity of their chemical bonds resulting

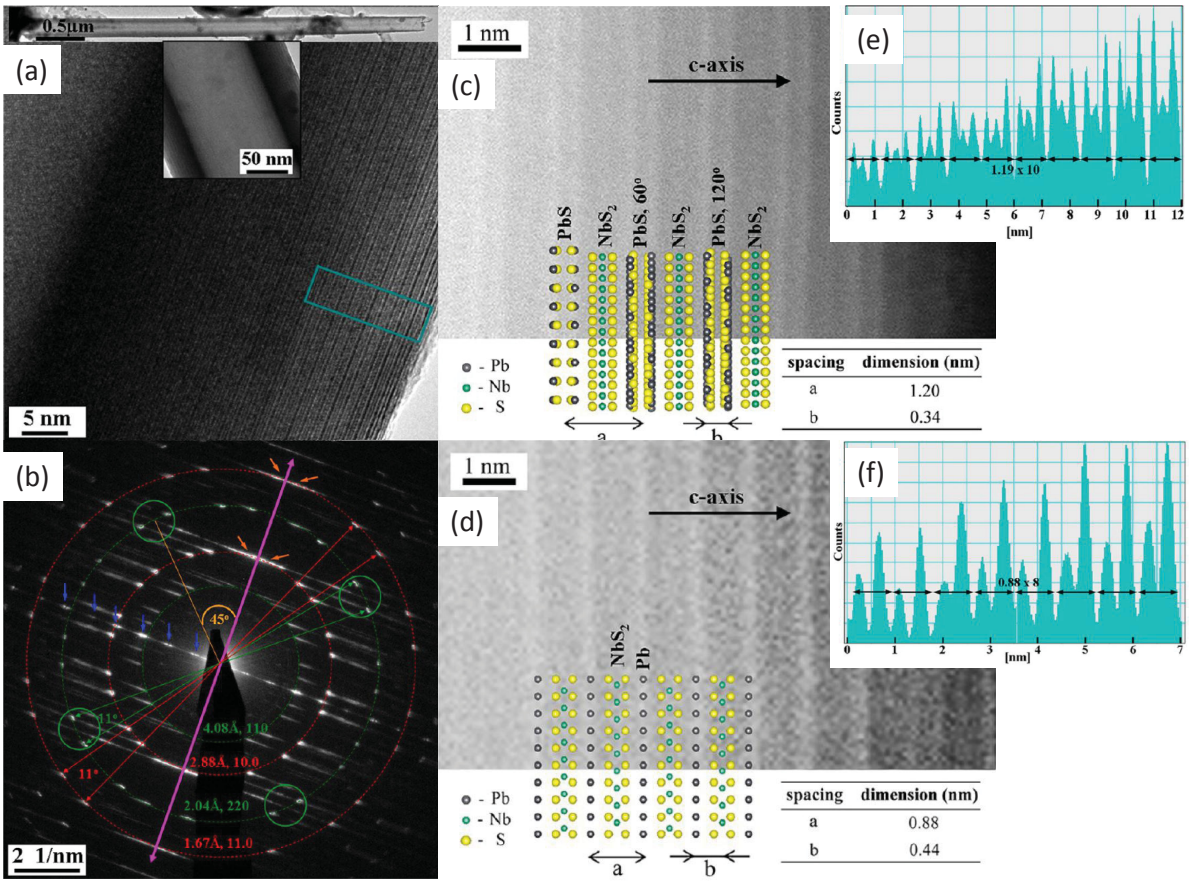

Figure 2.3.: Structural characterization methods of $(PbS)_{1.14}NbS_2$ and $PbNbS_2$ nanotubes. Descriptions in the text. Adapted from Fig. 5 and Fig. 7 of Ref. [6].

in higher folding energies. Both, nanoscrolls and nanotubes with concentric individual walls are encountered with the ratio nanoscrolls *vs.* nanotubes depending on the growth conditions and, more importantly, on the symmetry of the crystals. High symmetry favors the formation of nanotubes as the facets are more easily seamed [45]. A variety of growth steps leading to a telescope-like shape of the nanotube as a whole, particularly in larger diameter misfit layer nanoscrolls [7], conical tubules as well as nanoscrolls with partly unfolded sheets have been observed quite frequently [6, 7, 45, 46]. Contributing to the wealth of appearances are dislocation-like defects that could possibly lead to a transition from nanoscrolls to nanotubes by an "unzippering" mechanism [6] and thin nanotubes with constant outer diameters of 20-40 nm that could serve as template for further scrolling of additional misfit sheets [7].

Shown in Fig. 2.3. are different steps of the structural analysis of an exemplary $(PbS)_{1.14}NbS_2$ nanotube. The misfit layer nanotube pictured in Fig. 2.3.(a) exhibits alternating layers of PbS and trigonal prismatically coordinated NbS_2, stacked along a common c axis. A line profile of the region enclosed in the rectangle in panel (a) [Fig. 2.3.(e)] as well as a scanning transmission electron microscope high-angle annular dark-field (STEM-HAADF) image (of another similar nanotube) [Fig. 2.3.(c)] reveals equidistant fringes of 1.20 nm that correspond to half the c lat-

tice parameter of 2H-NbS_2 plus the c lattice parameter of a PbS layer. A lot about the inner structure of the nanotube can be learned from the selected area electron diffraction (SAED) patterns of panel (b). Without going too much into detail, the periodicity along the c axis can be confirmed, interplanar spacings and Miller indices can be derived from the sets of reflection points equi-azimuthally distributed on circles (red for NbS_2, green for PbS) and the splitting of these sets of reflection points allows for the deduction of a small chiral angle of 5.5° (half of the 11° splitting). In the ortho-hexagonal unit cell of NbS_2 (with orthogonal lattice axes, see previous section) there are three possible and equivalent orientations rotated by 60° for the adjacent PbS layer, the presence all of which can be identified in the diffraction pattern of panel (b). Schematically, the different orientations of the PbS layer with respect to the NbS_2 layer are shown in the inset of panel (c) - only one of them has its b axis in the direction of the nanotube axis - but in the nanotube all of them share the same chiral angle, that is, 5.5° in this case. Actually, most $(PbS)_{1.14}NbS_2$ nanotubes were found to possess a (small) chiral angle [6, 45]. Even though in the b direction the PbS layer adopts to the NbS_2 b-parameter, a small mismatch may be accommodated by a small deviation from this "commensurate" direction [6, 12]. As in the bulk misfit structure, both, *stage 1* [6] and *stage 2* [12] nanotubes seem to exist.

NbS_2 nanotubes intercalated with lead atoms and a c-periodicity of 0.88 nm were also observed [6] and a STEM-HAADF picture as well as a line profile of a $PbNbS_2$ nanotube are depicted in Fig. 2.3.(d) and (f), respectively. The lead atoms are linearly coordinated to adjacent sulfur atoms (Fig. 2.3.(d) inset), Pb and NbS_2 layers alternate, and the ratio between the niobium and lead atoms is close to 1:1. These $PbNbS_2$ nanotubes have uniform inner and outer diameter, are sometimes more than 10 μm long and are believed to grow unidirectionally [6]. The outer diameters of $(PbS)_{1.14}NbS_2$ and $PbNbS_2$ nanotubes range typically between 50 and 250 nm but can reach diameters up to 500 nm.

Nanotubes comprising SnS and SnS_2 investigated in this thesis are the prototype for misfit layer NTs with octahedral coordination of TS_2 layers. Reference [7] presents the synthesis and characterization of $(SnS)_{1.32}SnS_2$, $(SnS)_{1.32}(SnS_2)_2$ and $[(SnS)_{1.32}]_2[SnS_2]_3$ nanotubes. While characterization methods and basic structural concepts such as predominant small chiral angles resemble the above description of Pb-Nb-S nanotubes, the coexistence of different polytypes reflects the stronger autonomy of individual layers and weaker interlayer interaction. SnS and SnS_2 layers do not always alternate along their common c axis, but form ordered superstructures of the sequence O-T-T, O-T and O-T-O-T-T (in order of abundance, O stands for the orthorhombic SnS, T for the SnS_2 lattice) with evenly spaced fringes seen in the line profiles of 1.74 nm (0.56+0.59+0.59 nm), 1.15 nm (0.56+0.59 nm) and 2.89 nm (0.56+0.59+0.56+0.59+0.59 nm), respectively [6]. Random stacking is rarely encountered [7]. The interplanar spacings of both subsystems remain practically unaltered relative to their respective parent compounds, hence both in-plane lattice parameters are principally incommensurate in the SnS-SnS_2 system, in contrast to the Pb-Nb-S system [6, 7]. Not only is this further evidence of weak interlayer interaction but also of a higher degree of freedom regarding interlayer orientation which leads to multiple helicities and in-plane orientation of neighboring layers. However, there is still a

preferred orientation with specific planes of SnS and SnS_2 roughly coinciding with the tube axis. Typical diameters of SnS-SnS_2 nanotubes are 20-60 nm for straight tubules and up to 160 nm for nanotubes with growing steps. The diameters are thus smaller than those observed in the Pb-Nb-S system, probably due to higher rigidity of bonds in Pb-Nb-S materials [6].

3 Electronic properties

3.1. Transition metal dichalcogenides

The structure of the (transition) metal dichalcogenides discussed in detail in the last chapter determines the electronic properties of this family of materials. Metal cations of group IVA (Sn), IVB (Ti, Zr, Hf), VB (V, Nb, Ta) and VIB (Cr, Mo, W) are surrounded by six chalcogen anions (S, Se, Te) in sandwich-like trilayers that are stacked upon each other. Bonding within the layers is of covalent or ionic nature and contrasts the weak interlayer forces of van der Waals character. Owing to the layered structure, many of the electrical and optical properties are extremely anisotropic. Consequently, the term quasi two-dimensional materials is frequently used. Recent years have seen a tremendous increase in interest in layered TMDs that - in analogy to a famous article about graphene [47], the mother of two-dimensional materials - could be called "the rise of transition metal dichalcogenides". One of the advantages over graphene is the diversity of electronic properties and, most importantly, a sizable band gap in materials like MoS_2. While the renewed interest in TMDs is due to the exploration of their properties as low-dimensional materials (few-layer, see section 3.3, and nanotubes, see section 3.4) the bulk materials are well known and their properties have been investigated for decades. A comprehensive review was published already in 1969 by Wilson and Yoffe [1] and includes transmission spectra as well as a simple electronic structure model derived from the ligand-field theory. It is best explained with the help of Fig. 3.1. In the TX_2 materials, the chalcogen s and p orbitals form the occupied bonding and unoccupied antibonding σ and σ^* bands below and above the Fermi energy. To be fully occupied and adopt the energetically attractive noble gas configuration, each of the two chalcogen valence band ns^2np^4 orbitals needs two electrons. These are supplied by metal s and d electrons, leaving them in the oxidation T^{4+} status while the chalcogen atoms reach the X^{2-} oxidation status. Thus, there are now a total of 16 electrons (4 s and 12 p electrons) in the valence band. In the energy gap between the chalcogen valence orbitals and the unoccupied chalcogen conduction band states, the d orbitals of the metal atoms are situated. For the octahedral compounds, they are energetically split into a twofold degenerate e_g level, composed of d_{z^2} and $d_{x^2-y^2}$ orbitals and a threefold degenerate t_{2g} level with d_{yz}, d_{xz}, d_{xy} orbitals. For trigonal prismatic compounds, the d states split into three groups, d_{z^2} (a_1), $d_{x^2-y^2}$, d_{xy} (e),

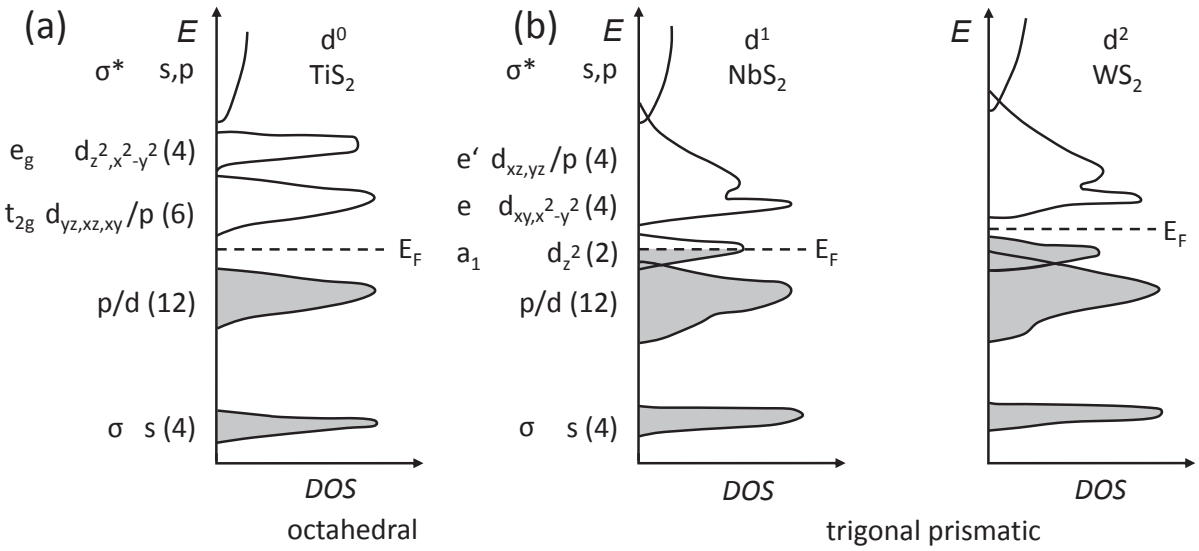

Figure 3.1.: Adapted from Ref. [48] (octahedral compounds) and Ref. [49] (trigonal prismatic compounds). This simple electronic band scheme was first introduced by Wilson and Yoffe [1] and depicts the successive filling of the d_{z^2} band determining the electronic properties of octahedrally coordinated group IVB transition metal dichalcogenides to trigonal prismatically coordinated group VB and VIB TMDs.

and d_{xz}, d_{yz} (e'), and between the first two there is an energy gap of around 1 eV [48]. Their electron population - and for the group IVB, VB and VIB TMDs more specifically the degree of filling of the narrow d_{z^2} band - determines the electronic properties of the transition metal dichalcogenides. The type of chalcogen atom, sulfur, selenium or tellurium has little influence on the electronic structure of the TMDs.

Starting with TiS_2 as a representative of the group IVB TMDs, as a consequence of the titanium $3d^2 4s^2$ valence electrons being transferred to the sulfur orbitals, above the Fermi energy, the TiS_2 d_{z^2} orbital is empty, as shown in Fig. 3.1.(a). Most of the group IVB TMDs are consequently semiconductors or in some cases semimetals due to d-p orbital overlap [1, 49, 50]. Similarly to the IVB materials, the SnS_2 group IVA metal dichalcogenide is a semiconductor with the tin $5s^2 5p^2$ valence orbitals emptied by electron transfer to the sulfur atoms. A reported indirect band gap energy of SnS_2 is 2.06 eV [51]. SnS_2 as well as all of the IVB TMDs crystallize in the octahedral $1T$ bulk structure (see Chapter 2).

NbS_2 is the representative of the group VB transition metal dichalcogenides investigated in this thesis. The depopulation of the niobium $4d^4 5s^1$ valence orbitals leaves all but one d^1 electron in the NbS_2 d_{z^2} orbital. The Fermi energy crosses this half-filled orbital in the middle and all of the VB TMDs are therefore of metallic character [see Fig. 3.1.(b)]. In Fig. 3.2. a calculated band structure of bulk NbS_2 [52] along the high symmetry lines of the Brillouin zone basically confirms the simple picture developed by Wilson and Yoffe. It also shows that for the case of NbS_2 there is no so-called p-d gap between the d_{z^2} band and lower lying p orbitals, as the latter

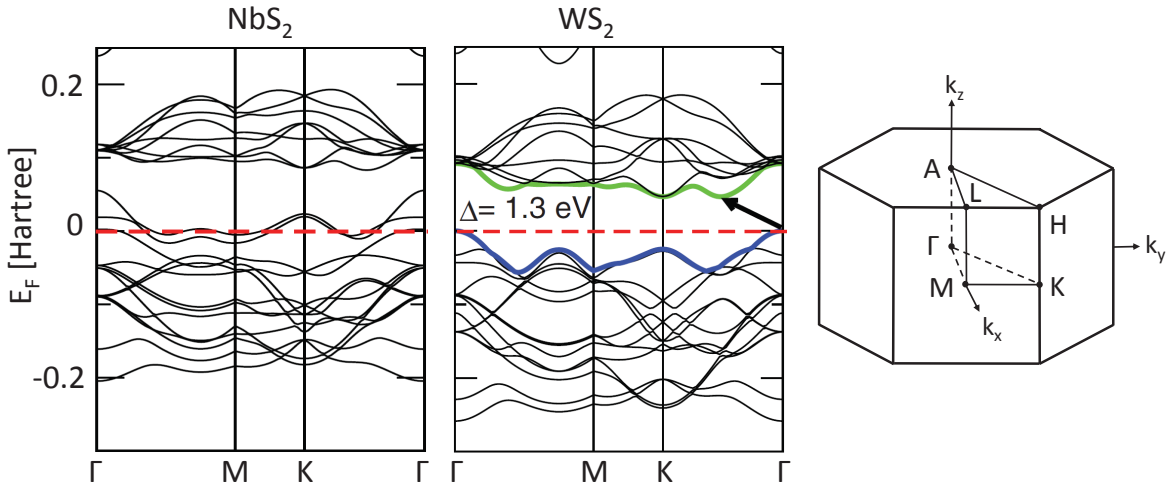

Figure 3.2.: Shown are the electronic band structure (calculated in and adapted from Ref. [52]) for the metal group VB TMD NbS_2 with bands crossing the Fermi energy at several points within the Brillouin zone and for the semiconducting group VIB TMD WS_2, where excitons at the K-point (not shown here) play an important role in determining the electronic properties. Shown on the right side is the Brillouin zone of the hexagonal lattices.

are seen crossing the Fermi level around the Γ-point.

In contrast to the group IV compounds, there are $2H$ (NbS_2) as well as $1T$ polytypes present with TaS_2 found in both configurations. An important feature of group VB TMDs is, with few exceptions including $2H$-NbS_2 [53], the development of a PLD-CDW (Peierls lattice distortion - charge density wave) below a critical temperature T_0 [49]. This phenomenon is only present in quasi one- and two-dimensional materials and describes the occurrence of a periodic modulation of the electron density together with a distortion of the ions forming the periodic lattice. The latter creates a new super unit cell accompanied by an energy gain that compensates, below T_0, for the energy spent for the electron and ion distortion. In quasi one-dimensional materials, the electron energy reduction at the Fermi energy leads to a metal-insulator transition, however, this is not necessarily the case for the layered TMDs which stay metallic [49]. Typical onset temperatures are around 600 K for compounds in the octahedral and below 100 K for compounds in the trigonal prismatic arrangement [49]. At even lower temperatures the group VB TMDs exhibit superconductivity in the single digit range, a recent value for T_c in NbS_2 for example is 6.05 K [54].

The group VIB transition metal dichalcogenides containing molybdenum and tungsten are semiconductors due to their d_{z^2} orbital being fully occupied with two electrons [see Fig. 3.1.(b)]. There is pronounced hybridization between sulfur p orbitals and metal d orbitals [55]. Chromium-based materials as a third member of the group VIB TMDs are unstable in layered form and only exist as part of misfit layer compounds. Structurally, for the VIB TMDs, MoS_2 and WS_2 crystallize in the trigonal prismatic coordination, whereas the chromium atom is octahedrally coordinated to six sulfur atoms in chromium-based MLCs [56]. The indirect band gap of molyb-

denum and tungsten compounds is in the near infrared [57]. Concentrating on WS_2 as the material investigated in this thesis, experimental values for the indirect band gap range between 1.35 and 1.4 eV [58–60], with the top of the valence band situated at the Γ-point while the lowest conduction band state is halfway between Γ- and K-point [52, 61, 62], see Fig. 3.2.

The lowest direct band gap on the other hand is found at the K-point and the optical transitions of the group VIB TMDs are governed by excitons, which in contrast to the group VB TMDs are not screened out by free carriers. Absorption measurements reveal the presence of a number of peaks, typically labeled A and B for the most pronounced exciton features at the absorption edge and a broader band C at higher energies. Exemplary, this is shown for WS_2 in Fig. 3.3. [63] and values for the A and B exciton reported are 1.95 and 2.36 eV, respectively [58]. They arise as a result of vertical optical transitions from a spin-orbit split valence band at the K-point to the conduction band [62]. The presence of excitons complicates the determination of the size of the direct band gap. Assuming an exciton binding energy of 0.06 eV, Ballif *et al.* [58] estimate a value of 2.01 eV at room temperature. A calculated band structure of WS_2 along the Γ-K-M-direction is depicted in Fig. 3.2. for the middle plane of the hexagonal Brillouin zone shown on the right. In the upper plane along the A-H-L-A high symmetry points, the band structure looks similar, but the bands that are split in the Γ-K-M-plane are double degenerate in the upper plane [55, 61].

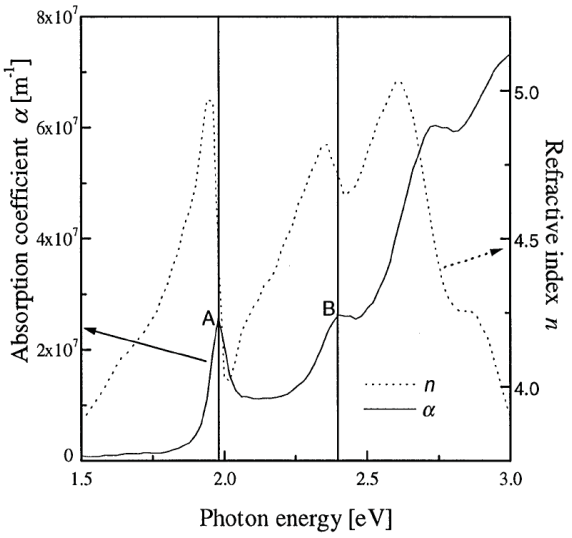

Figure 3.3.: WS_2 single crystal absorption spectrum in the vicinity of the band gap with prominent A and B exciton peaks [63].

3.2. Misfit layer compounds

Research on the electronic structure of misfit layer compounds $MX/RX{-}TS_2$ (M = Pb, Sn; R = rare earth metal, T = Ti, Nb, Ta, Cr...; X = S, Se, Te) is basically driven by a single question: how and to what extent do the two subsystems influence each other and how is the remarkable stability of misfit compounds to be explained? The alternately stacked constituents in the MLC are neither electronically nor geometrically similar, yet, they form ordered superstructures that can be chemically synthesized [41, 64, 65]. Layered chromium disulfide even only exists by virtue of the interaction with the monochalcogenide layers in the misfit compound LaS-

CrS_2 [11, 45, 66]. It can be generally stated that the formation of misfit layered compounds is restricted to divalent metals M, like Sn^{2+} and Pb^{2+} with a lone pair of electrons or trivalent rare earth metals R like La^{3+} or Ce^{3+} [67]. Historically, before research on misfit layer compounds gained momentum, the intercalation of TMDs with alkali metals and other electron donors was thoroughly investigated [49]. It was generally found that an electron transfer from the intercalated atoms to the TX_2 layers takes place and, to continue with the above mentioned example, is the *raison d'être* for layered CrS_2 [68]. The electron donation results in an increased ionicity and therefore a stronger bonding between the layers. The main concepts of the electronic structure of TS_2 intercalation compounds were then later adopted for misfit layered compounds in that a charge transfer was assumed to play a stabilizing role. Because interlayer interaction is weaker than the covalent intralayer bonds, the MS layers are often regarded as intercalation derivatives of layered transition metal dichalcogenides. From an electronic structure point of view, considering the MS and the TS_2 layer as two separate constituents has the consequence that the band structure of the misfit layered compound may be constructed by a superposition of the band structures of the subsystems.

This rigid band model has found widespread application in trying to explain the band structures of MLCs. Many authors state that it is a good first approximation with the only change being a charge transfer from the MS layer to the TS_2 layer and a subsequent adjustment of the Fermi level. The concept is shown schematically in Fig. 3.4. for the misfit compounds $(PbS)_{1.18}TiS_2$ (a) and $(PbS)_{1.14}NbS_2$ (b). In the octahedrally coordinated group IVB TiS_2 compound the broad $3d$ conduction band is either completely empty or only slightly filled, depending on whether it is considered a semiconductor or a semimetal in the pristine compound (see previous section), and

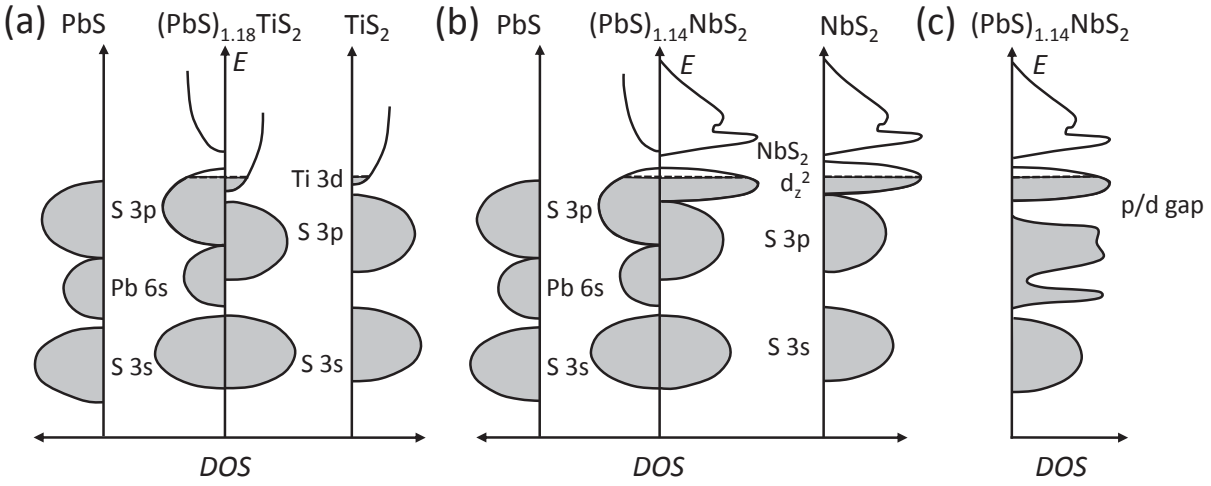

Figure 3.4.: Concept of the rigid band model illustrated for an octahedrally coordinated group IVB (a) and a trigonal prismatically coordinated group VB misfit layer compound (b): the electronic band structure can be seen, to a first approximation, as a superposition of the electronic structure of the subsystems. (c) Phenomena like the opening of a *p-d* gap in the misfit layer system are deviations from the rigid band model. Figure adapted from Refs. [17, 69, 70].

as electrons from the PbS subsystem, a narrow band semiconductor, are donated, the electron population is increased. In the trigonal prismatically coordinated group VB metal NbS_2 the half filled d_{z^2} band can accommodate up to one more electron in the misfit structure leaving an equal amount of holes in the PbS part. Both constituents can principally take part in electrical (hole/electron) conduction. Confirmation for the validity of the rigid band model in a first approximation was found by the Ohno and the Ettema group by a variety of experimental techniques [valence band (UPS) and core level photoelectron spectroscopy (XPS), X-ray absorption spectroscopy (XAS), low energy electron diffraction (LEED) and reflection electron energy loss spectroscopy measurements (REELS)] for the electronic structure of $MS{-}TS_2$ compounds (M = Pb, Sn; T = Ti, Nb, Ta) [71–75]. For example, the valence band structures of SnS-NbS_2 and PbS-TiS_2 measured by photoelectron spectroscopy look very similar to the added spectra of the constituents except for a slight shift in binding energy and an increased shoulder related to the Nb d_{z^2}/Ti 3d t_{2g} orbital in the misfit compound as well as a downshift of the Fermi energy, indicating the filling of these states due to charge transfer [71]. However, no agreement was reached concerning the magnitude of charge transfer and the nature and strength of interlayer interaction in compounds containing PbS and SnS. One of the higher values of charge transfer per monochalcogenide atom, namely $\Delta_{CT} = -0.4$ electrons per Nb from the SnS to the NbS_2 subsystem in $(SnS)_{1.20}NbS_2$, was derived from band structure calculations by Fang *et al.* [76]. A charge transfer was also confirmed by angle-resolved ultraviolet photoelectron spectroscopy (ARUPS) and theoretical band structure calculations by Brandt *et al.* in $(PbS)_{1.18}TiS_2$ and $(PbS)_{1.14}NbS_2$ [77, 78]. As for the SnS-SnS_2 compound that is also investigated in this thesis in nanotubular form, rather surprisingly, recent theoretical results suggest that there is a very small amount of charge transfer (about 0.1 electron per SnS_2 unit) from the SnS_2 to the SnS layer, in opposition to what is common in misfit compounds [79]. To summarize, the existence and the amount of charge transfer in MLCs with divalent metal cations in the MS layer is to date still under debate. A number of alternative and complimentary mechanisms possibly taking part in the interlayer interaction have been suggested in the past years and shall be discussed later in this section.

Contrary to the above discussed materials, for the misfit compounds with RS, where R is a rare earth metal, on the other hand, it is general consensus that each rare earth metal donates almost one electron to the d orbitals of the transition metal dichalcogenide. From band structure calculations and UPS as well as XPS measurements it is shown that there is a transfer of about 0.7-0.9 electrons per rare earth metal atom to the TS_2 layer in $(LnS)_{1.14}TS_2$ (Ln = La, Ho, Tb, Dy) leaving the d_{z^2} band at the Fermi level filled up to 0.3-0.1 remaining holes per transition metal atom [80, 81]. Another method to estimate the magnitude of the d band filling is the measurement of the optical reflectivity spectra where the plasma frequency can be used to deduce an estimation of the carrier density in the misfit compound. Suzuki *et al.* [82] and Rüscher *et al.* [83] found a significant reduction in the Drude edge frequency of rare earth TS_2 materials compared to the pristine TS_2 layers, and carrier densities were estimated to be smaller than in the corresponding PbS, SnS compounds per TMD in accordance with a higher

magnitude of charge transfer in the former compounds. A main result of all these investigations is that most of the rare earth metal can reach a preferred 3+ oxidation state with possible mixing with 2+ cations. There are even indications that the *Ln* cations are exclusively in the 3+ oxidation state which is achieved by either having *Ln* vacancy sites [84, 85] or by having excess electrons strongly localized in the 5*d* conduction band states which would also explain that electrical conduction seems to come entirely from the $T\mathrm{S}_2$ layer [13]. Whereas in rare earth compounds the adopted oxidation state is in agreement with a significant charge transfer, for Pb compounds the same argument is found to disfavor a considerable donation of electrons to the TMD subsystem. Charge transfer would imply a formal 4+ oxidation state of Pb atoms (that have an additional valence electron compared to the rare earth metals) in the monosulfides which in fact has never been observed [66]. So, instead of the pure charge transfer mechanism a couple of additional models have emerged since the mid-1990's and shown to be of value when trying to elucidate the stability and interlayer interaction in misfit layer compounds. They shall be briefly discussed in the following.

1) A *cationic coupling mechanism* was first observed by Moëlo and coworkers when investigating the precise atomic composition of a variety of incommensurate sandwich layered compounds $[(\mathrm{Pb,Sn})\mathrm{S}]_{1+x}[(\mathrm{Nb,Ti})\mathrm{S}_2]_m$ $(0.08 \leq x \leq 0.28, m = 1-3)$ [86]. By electron microprobe analysis the authors were able to show that there is a systematic Pb/Sn depletion in the $M\mathrm{S}$ part of the structure that can be related to a substitution by excess transition metal atoms of the $T\mathrm{S}_2$ layer. The Nb/Ti atoms take up a valency of 3+ in the $M\mathrm{S}$ layer, charge balance is restored by the reduction of an equivalent amount of $\mathrm{Nb}^{4+}/\mathrm{Ti}^{4+}$ cations in the $T\mathrm{S}_2$ layer to the same 3+ oxidation state. As a result, there is an electron excess in the trilayers compared to the single oxidation state subsystem, which is a simple way to account for the observed *d* band filling normally attributed to charge transfer without an actual donation of electrons from one layer to the other. In the monolayer ($m = 1$) case a composition $(\mathrm{Pb}_{0.991}\mathrm{Nb}_{0.126}\mathrm{S}_{1.136})\mathrm{NbS}_2$ is detected with a Pb/Nb substitution of 12% and the authors conclude in stating that when considering the whole MLC the observed nonstoichiometry is a decisive stability criterium. The described mechanism that results in an electrostatic attraction between the constituents is called cationic coupling or hidden charge transfer [87] and enhances the interlayer ionic bonding.

2) The *metal cross-substitution mechanism* can be understood as an extension of the cationic coupling model. In $(\mathrm{PbS})_{1.13}\mathrm{TaS}_2$ not only do the Ta atoms substitute for lead atoms but the reverse effect is also seen [88]. The core level XPS at separate PbS and TaS_2 domains both exhibit spin-orbit split Ta 4*f* and Pb 5*d* levels confirming the presence of the two elements in each of the two subsystems. The parameters x and y in the resulting misfit compound $(\mathrm{Pb}_{1-x}\mathrm{Ta}_x\mathrm{S})_{1.13}(\mathrm{Ta}_{1-y}\mathrm{Pb}_y\mathrm{S}_2)$ are of the order 0.1-0.2, the overall charge transfer is small (around 0.1 electrons per TaS_2 unit) but in accordance with other experimental observations. According to the authors, even formally stoichiometric compounds can thus be stabilized due to electrostatic interaction between adjacent layers. This is contradicted by *ab initio* calculations [89] where the nonstoichiometry (only Ta atom substitution for Pb atoms) as put forward by Ref. [86] is found to stabilize the material. Although the authors do not exclude the existence

of metal cross-substitution, they find that only the nonstoichiometric compounds have negative formation energy. Interestingly, according to the calculations, the ideal misfit compound has about zero formation energy compared to the parent compounds, making the cationic model even more likely.

3) The *covalent bonding* between layers was suggested by the Ettema group when looking for an alternative way of explaining the MLC stability in view of their studies excluding charge transfer as the underlying reason [74, 75]. A hint was given by the broadening of the metal core level states compared to the parent MS compound which is explained by the changing coordination number to sulfur atoms of the TS$_2$ layer along the incommensurate direction. By employing the bond valence mode [90] it was shown by Fang *et al.* [76] (who found evidence of small electron donation to the NbS$_2$ layer in $(SnS)_{1.12}NbS_2$) that the interlayer binding energy induced by weak covalent bonds may have a larger impact on overall stability than the electrostatic interaction due to charge transfer.

In summary, there are a number of partly contradicting models to explain the stability of and give insight into the nature of interlayer interaction in misfit layer compounds. The charge transfer from the MS to the TS$_2$ layer seems to be rather small in MLC with divalent M cations and in many experimental studies an observed filling of transition metal d states is possibly mistaken for real charge transfer when in fact it follows from the hidden charge transfer induced by the cationic coupling mechanism or metal cross-substitution. Nonetheless, band structure calculations that do not take into account the mentioned mechanisms but deal with the ideal stoichiometric materials seem to indicate at least some small magnitude of charge transfer [78, 88]. Covalent interlayer bonding is suggested by some authors but so far there is a lack of direct observation of this type of interlayer interaction. It is well possible that a mixture of the described mechanisms makes for the stability of misfit layer compounds.

The situation is a little different for transition metal dichalcogenides intercalated with mainly alkali metals and post-transition metals like Pb and Sn. There is a wealth of experimental studies on these compounds and an interesting example are the MTS$_2$ compounds where M atoms are linearly coordinated to the sulfur atoms of the neighboring group VB transition metal dichalcogenide trilayer [see Fig 2.2.(e)]. The compound PbNbS$_2$ was studied in nanotubular form as part of this thesis (see section 5.4.). A charge transfer of one electron per metal atom to the Nb, Ta atoms in MTS$_2$ is proposed by several authors [91–93] and the d_{z^2} is then completely filled. Double peak core level Sn $3d_{5/2}$ / Pb $4f_{5/2}$ peaks are explained in terms of a rapid M/M^{2+} valency fluctuation and the formal average valency of M^{1+} is manifestation of a donation of one electron to the TMD layer. Electrical conduction is then possible in the Pb layer in overlapping $p_{x,y}$ orbitals [92]. Covalent bonds that can be deduced from the observed hybridization between intercalant p states and sulfur p_z states contribute to the overall stability [93].

As for the validity of the rigid band model in misfit layer compounds, despite being a helpful first approximation, deviations from a pure superposition of the electronic band structures of the constituents go beyond the filling of the transition metal $d_{z^2}/d\ t_{2g}$ band. These include a loss of dispersion of S $3p$ states along the Γ-A-direction that is present in the two layer thick

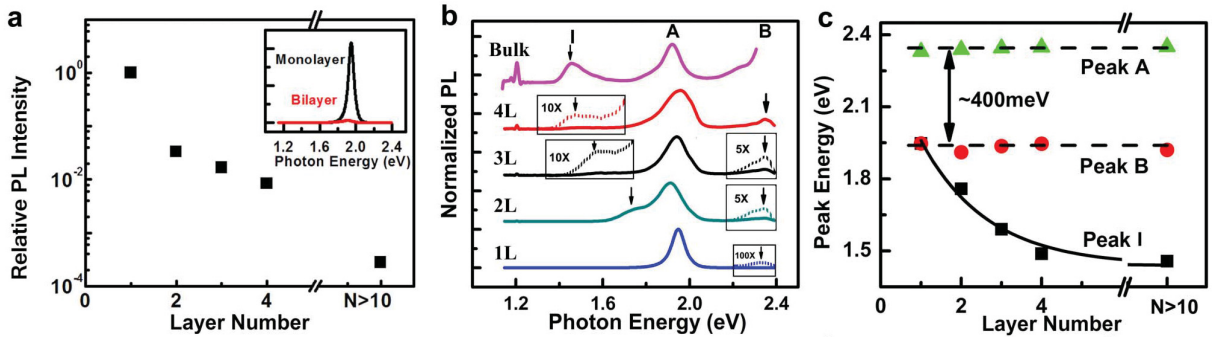

Figure 3.5.: (a) Relative photoluminescence intensities in mono- and few-layer WS_2. (b) Normalized PL signal (with respect to the PL intensity of the A exciton), where A and B denote the excitons and I the indirect band gap photoluminescence. (c) Energetic position of excitons A and B and the indirect band gap as a function of layer thickness. Taken from Ref. [95].

unit cell of the $2H$-TS_2 parent compounds due to interlayer interaction [75, 77, 78, 94] as well as the subsequent opening of an energy gap between transition metal derived d and sulfur derived p states (p-d gap) [see Fig. 3.4.(c)].

3.3. Few-layer transition metal dichalcogenides

The idea of thinning layered materials down to mono- and few-layer is not new and there were a few more or less successful attempts, but it was long believed that a (quasi) two-dimensional arrangement of atoms would be thermodynamically unstable [96, 97]. Once the breakthrough was achieved with the preparation of graphene and monolayers of transition metal dichalcogenides in 2005 [98] an entirely new research area was born. But it was not until five years later that Mak *et al.* [99] and Splendiani *et al.* [100] observed experimentally the key characteristic that distinguishes materials such as MoS_2 and WS_2 from graphene and interest in low-dimensional TMDs rose to new heights. While group VIB bulk and few-layer transition metal dichalcogenides are indirect semiconductors there is a crossover to a direct band gap material in the monolayer limit. The discovery of other unique properties such as huge spin-orbit splitting and spin-valley coupling, many of which are highly interesting for applications in nanoelectronics, valleytronics and spintronics, followed, and today work on this new class of materials is still thriving.
In the following I will, where possible, concentrate on the material WS_2 as the material of choice of this thesis. As for the group VB TMD NbS_2 also investigated in this thesis, it has been shown that, apart from the opening of a p-d gap, the band structures of mono- and few-layers maintain the metallic properties of the bulk [52, 101, 102] (see also Fig. 3.2.). In monolayer WS_2 strong photoluminescence (PL) emerges in the A excitonic regime [103, 104] that is successively quenched when layers are added and completely absent in the bulk. Additionally, much weaker signal comes from the B excitonic transition and the indirect band gap is a competing light emission channel for layer numbers of more than one. In Fig. 3.5. normalized PL spectra are

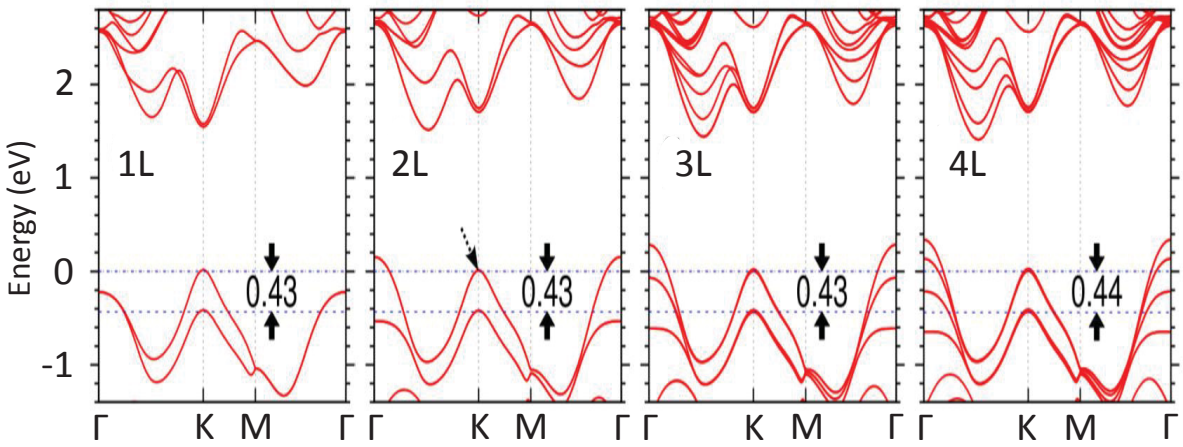

Figure 3.6.: *Ab initio* band structure calculations for FL-WS_2 from mono- (1L) to quadlayer (4L). The spin-orbit splitting is included in the calculations and nearly constant valence band splittings are observed at the K-point. Adapted from Ref. [95].

shown for WS_2 from one to five layers [95] and whereas the energetic position of A and B exciton barely change with N, the indirect band gap is seen to blueshift considerably with decreasing layer number.

The evolution of the photoluminescence signal with the layer number N is experimental proof of a cross over from an indirect band gap to a direct band gap when approaching the WS_2 monolayer. It had been theoretically predicted before for the isostructural MoS_2 monolayer [100, 105, 106] and shall be described with the help of Fig. 3.6. where the calculated band structure of mono- to quadlayer WS_2 is depicted [95]. For $N > 1$ the valence band maximum (VBM) is situated at the Γ-point while the conduction band minimum (CBM) is found about halfway between the Γ- and the K-point. This indirect band gap is reported to be of about 1.35 eV size for bulk WS_2 [63]. The states at both the VBM and the CBM are mainly composed of hybridized tungsten d_{z^2} and sulfur p_z orbitals that have significant expansion into the interlayer van der Waals gap and are thus very sensitive to the interlayer coupling and consequently to the number of layers [100]. On reducing the layer thickness, as a result of quantum confinement, the Γ-point energy is reduced and the CBM goes up in energy [52] resulting in the observed blueshift of the indirect band gap. The K-point states, on the other hand, are localized more or less in one trilayer [107] and stay approximately of the same energy irrespective of N. In the monolayer case this lets conduction band minimum and valence band maximum coincide at the K-point and makes monolayer WS_2 a direct band gap semiconductor. The calculations shown in Fig. 3.6. take into account spin-orbit coupling and reveal the existence of a huge splitting of more than 400 meV [95, 107, 108] at the valence band K-point, significantly higher than in MoS_2, where it is reported to be about 150 meV [107]. This gives rise to another key characteristic of WS_2 and other group VIB TMDs, namely the excitonic optical transitions A and B from the nearly degenerate conduction band at the K-point to the split valence band.

As seen in Fig. 3.5. and 3.6. the *A*-*B* splitting gets only slightly bigger from monolayer to bulk but is nearly constant, despite possibly having different origins in the case of odd (without inversion center) and even (with inversion center) layer number [109–111]. Exciton binding energies are unusually high in monolayer and few layers due to reduced dielectric screening with values reported reaching about 1 eV for monolayer WS_2 [112, 113] while only a few tenths of meV are normally encountered for the bulk materials [1]. The huge excitonic binding energies in the monolayers also enable the stability of charged excitons - trions - where an additional electron is bound (with around 20 meV binding energy for monolayer MoS_2 [114]) to an existing electron-hole pair [115–117]. Very notably, the orientation of the *A* and *B* exciton in few-layer MoS_2 has been found to be almost entirely in-plane without significant expansion in the stacking direction of the layers [111, 118]. In contrast, the higher-energy *C* exciton stretches out in all directions and its energetic position is observed to be dependent on layer number [118].

3.4. Inorganic nanotubes

Due to their always multiwalled form, inorganic nanotubes do not differ much from their bulk counterparts regarding the electronic properties. While FL-TMDs show interesting two-dimensional properties, in contrast to the much thinner single walled carbon nanotubes, only a limited number of properties of inorganic nanotubes can be associated with being characteristic for one-dimensional materials. One of them is the manifestation of the so-called antenna effect - the strong depolarization of light traveling perpendicular and the selective occurrence of optical transitions parallel to the direction of the nanotube axis [119, 120]. There are a number of theoretical investigations on hypothetical single-walled MoS_2 and WS_2 nanotubes that show that the chiral vector dictates the nature of the band gap [121–124]. Armchair nanotubes therefore possess indirect band gaps and zigzag nanotubes are direct band gap materials with band gap sizes always smaller than the direct band gaps of the armchair nanotubes. These calculations are only of theoretical value, however they reveal also a size dependence of the indirect band gap on the diameter of the nanotube that finds its equivalent in experimental observations. For inorganic fullerene-like IF-MoS_2 and IF-WS_2 Frey *et al.* [125] found competing mechanisms for the energetic positions of the *A* and *B* excitons. For layer numbers below six, quantum confinement effects prevail and the excitonic absorption peaks are shifted up relative to the bulk exciton energies. For larger layer numbers a redshift is seen that is attributed to strain brought about by the curvature of the layers and a discommensuration of adjacent IF walls. As part of this thesis, different diameter WS_2 nanotubes (38 nm to 121 nm) and a powder 2*H*-WS_2 bulk material as a reference were investigated by means of Resonance Raman spectroscopy [126]. From the Resonance Raman Profiles (RRP) *A* excitonic transition energies were derived and it was shown that there is a decrease in the first optical transition energy with decreasing diameter of the inorganic nanotube. These findings are in good agreement with results, theoretical and experimental, for a shrinkage of the indirect band gap in WS_2 nanotubes with decreasing diameter

[27, 127] and calculations that show that the curvature and the resulting strain of the nanotube walls are to be held accountable for the diameter dependence of the excitonic transition energies in particular [128]. In the nanotube walls the outer sulfur layers are exposed to tensile strain due to curvature, the inner sulfur layer to compressive strain relative to the transition metal atoms in the middle. The tensile strain brings about a reduction of the conduction band energy around the K-point, which is not balanced out by the effect of the compressive strain [128]. As also the excitonic optical transitions take place at the K-point, with decreasing diameter, increasing curvature and increasing tensile strain, the A excitonic transition energy redshifts.
The electronic properties of other inorganic nanotubes have up to now only been investigated theoretically. TiS_2 [129] and SnS_2 nanotubes [130] are semiconductors also in the single walled limit and have similar diameter and chirality dependencies of the band gap than WS_2 and MoS_2 NTs while NbS_2 nanotubes stay metallic like their parent material [131].
Misfit layer nanotubes have become a new member of the inorganic nanotube family only very recently and research so far has concentrated on their unique structural properties (see Chapter 2). Work on their electronic properties is scarce but it is safe to assume that coming years will see an increase of research in this field. As the diameters and wall numbers in misfit layer nanotubes are comparably large, most of the properties will resemble the respective bulk structures. As in the bulk MLCs, most importantly, the nature and strength of interlayer interaction needs to be addressed. In the SnS-SnS_2 system, the coexistence of a diversity of stacking sequences of SnS and SnS_2 layers [7] points to rather weak interlayer interaction and, if at all, to only weak charge transfer as was indeed shown by Lorenz *et al.* [79]. On the other hand CrS_2 MLC nanotubes [45] are only stable because there is a considerable amount of charge transfer from the MS layer and also for rare earth metal based MLCs charge transfer is well established [66, 80, 81, 83, 132]. In the course of this thesis SnS-SnS_2 as well as PbS-NbS_2 nanotubes were investigated thoroughly via Raman spectroscopy. While for the former system the Raman spectra indicate only weak interlayer interaction [5], huge frequency shifts of Raman modes in the latter compounds point to a larger influence neighboring layers exert on each other. Based on the Raman spectroscopic findings different possible mechanisms of interlayer interaction are subjected to a critical discussion [133].

4 Papers forming this thesis

1. *Excitonic resonances in WS_2 nanotubes.*
M. Staiger, P. Rafailov, K. Gartsman, H. Telg, M. Krause, G. Radovsky, A. Zak, and C. Thomsen
Physical Review B **86**, 165423 (2012)

I performed the Raman measurements, took Resonance Raman Profiles, interpreted all of the data and wrote the manuscript. Raman measurements of WS_2 nanotubes under hydrostatic pressure were performed by P. Rafailov. All authors commented on the manuscript. Individual nanotubes received from *NanoMaterials, Ltd.* were placed on substrate and characterized by SEM and TEM by G. Radovsky. The project was conceived by C. Thomsen and me.

2. *Splitting of monolayer out-of-plane A_1' Raman mode in few-layer WS_2.*
M. Staiger, R. Gillen, N. Scheuschner, O. Ochedowski, F. Kampmann, M. Schleberger, C. Thomsen, and J. Maultzsch
Physical Review B **91**, 195419 (2015)

I performed the Raman measurements, interpreted the data and wrote the manuscript. DFT calculations were done by R. Gillen and visualized by me. All authors, especially N. Scheuchner, discussed the data and commented on the manuscript. Samples were fabricated by O. Ochedowski from a WS_2 single crystal obtained from *hq graphene*. AFM and optical characterization was done by F. Kampmann and me. The project was conceived by J. Maultzsch, C. Thomsen and me.

3. *Raman spectroscopy of intercalated and misfit layer nanotubes.*
M. Staiger, V. Bačić, R. Gillen, G. Radovsky, K. Gartsman, R. Tenne, T. Heine, J. Maultzsch and C. Thomsen
Physical Review B **94**, 035430 (2016)

I performed the Raman measurements, interpreted the data and wrote the manuscript. DFT calculations were done by R. Gillen and V. Bačić. All authors discussed the data and com-

mented on the manuscript. Samples were synthesized, characterized and prepared for Raman measurements by G. Radovsky. The project was conceived by C. Thomsen and me.

Other

1. *Interlayer resonant Raman modes in few-layer MoS_2.*
N. Scheuschner and R. Gillen and M. Staiger, and J. Maultzsch
Physical Review B **91**, 235409 (2015)

2. *Electronic structure tuning of diamondoids through functionalization.*
T. Rander, M. Staiger, R. Richter, T. Zimmermann, L. Landt, D. Wolter, J.E. Dahl, R.M.K. Carlson, B.A. Tkachenko, N.A. Fokina, P.R. Schreiner, T. Möller, and C, Bostedt
The Journal of Chemical Physics **138**, 024310 (2013)

3. *Chiral index dependence of the G^+ and G^- Raman modes in semiconducting carbon nanotubes.*
H. Telg, J.G. Duque, M. Staiger, X. Tu, F. Hennrich, M.M. Kappes, M. Zheng, J. Maultzsch, C. Thomsen, and S.K. Doorn
ACS Nano **6**, 904-911 (2012)

4. *Synthesis of copious amounts of SnS_2 and SnS_2/SnS nanotubes with ordered superstructures.*
G. Radovsky, R. Popovitz-Biro, M. Staiger, K. Gartsman, C. Thomsen, T. Lorenz, G. Seifert, and R. Tenne
Angewandte Chemie International Edition **50**, 21316-12320 (2011)

5. *The influence of a single thiol group on the electronic and optical properties of the smallest diamondoid adamantane.*
L. Landt, M. Staiger, D. Wolter, K. Klünder, P. Zimmermann, T.M. Willey, T. van Buuren, D. Brehmer, P.R. Schreiner, B.A. Tkachenko, A.A. Fokin, T. Möller, and C. Bostedt
The Journal of Chemical Physics **132**, 024710 (2010)

6. *Intrinsic photoluminescence of adamantane in the ultraviolet spectral region.*
L. Landt, W. Kielich, D. Wolter, M. Staiger, A. Ehresmann, T. Möller, and C. Bostedt
Physical Review B **80**, 205323 (2009)

5 Context of the publications submitted

5.1. Introduction

In this thesis the goal was to gain insight into the vibrational and electronic properties of the family of transition metal dichalcogenide nanostructures. These layered materials are the inorganic analogues to carbon nanomaterials and have seen a stellar ascent in interest since their synthesis as nanotubes [22] and their preparation as mono- and few-layers [98]. They thus cover the spectrum from quasi one-dimensional nanotubes to the evolvement from the quasi two-dimensional monolayers in the direction of the three-dimensional bulk material in thicker few-layers. They have the ability to host intercalant atoms and to form misfit layer compounds where transition metal dichalcogenides and cubic monochalcogenides are stacked alternately.
Structurally and electronically there is a variety of parameters that have to be taken into account when discussing their properties. Yet, as we have seen in the last chapters, despite the plethora of different phenomena there are unifying concepts that form a common ground on the basis of which also the results of the papers forming this thesis can be seen. The results of the case studies performed in the course of this thesis reveal intimate relations between the different materials and, in the context of the layered transition metal dichalcogenides, have universal validity.
Working in a group that had years of experience in the field of carbon nanostructures, I started research with studying high energy vibrational modes in semiconducting and metallic carbon nanotubes [134]. In comparison to this early work, what really stands out in the main work of this thesis is that investigations were always carried out not on ensembles but on individual nanostructures where I had precise structural knowledge from e.g. electron microscopy characterization even prior to measurements.
The experimental method of choice and a means to find similarities in the manifold of layered inorganic nanostructures was Raman and Resonance Raman spectroscopy. These methods proved to be versatile tools not only to study the phonon modes of the investigated materials but they also allowed to draw conclusions about the respective electronic structure. The high symmetry of the bulk transition metal dichalcogenides implies that only a small number of phonon modes are first-order Raman-active. Irrespective of the number of layers, of how the layers are stacked

and whether they are in planar or tubular form, because the basic symmetry of individual layers is retained, the same vibrational patterns are found in all the investigated nanomaterials, with the exception of rigid layer modes that do naturally not occur in monolayers. Thus, for example, the Raman spectra of WS_2 nanotubes and NbS_2-based misfit layer compounds can be discussed on the basis of the same simple atomic intralayer vibrations. At the same time, phonon modes in general are very sensitive indicators of even the slightest change in structural or electronic properties. For the studied nanomaterials in particular, the frequencies and Raman intensities can change drastically depending on one hand on inherent factors such as the number of layers, the nanotube diameter, the defect density and the type of intercalant and on the other hand on outside influence like temperature or pressure change and the variation in Raman excitation energy.

For all the materials studied, there were two first-order Raman modes, namely an out-of-plane A and an in-plane E mode, that served as fingerprint modes to identify and analyze changes in the vibrational and electronic structure brought about by these two factors. For the former, in one trilayer, sulfur atoms are displaced along the stacking c direction while the metal atom in the middle does not take part in the vibration. In WS_2, this mode is well separated from all other modes and was the primary study focus of two of the papers forming this thesis [126, 135]. For the case of WS_2 nanotubes, it was shown that this mode shifts up with increasing external hydrostatic pressure. The changes in Raman cross section when scanning a larger excitation energy region were employed to derive a nanotube diameter dependence of the first optical A excitonic transition energy. A sister mode to the A_{1g} mode, the silent B_{1u} mode, where neighboring layer vibrate not in- but out-of-phase was observed to appear with considerable intensity in the resonance Raman spectra and to follow the same trends. Because of slightly different strength of interlayer interaction, this mode is split from the A_{1g} mode by a few wavenumbers and was identified to be a sensitive indicator of nanotube curvature and accompanying strain. The knowledge gained from the work on WS_2 nanotubes, especially the awareness of the possible appearance of non-Raman-active modes when exciting in the vicinity of the excitonic transition energy, was later transferred to the study of few-layer WS_2. With high-resolution Raman spectroscopy and a newly employed sub-pixel mode, a "N modes for N layer rule" was established with all the sidebands to the main out-of-plane mode following the already known effect of increasing Raman frequency of the A mode with increasing number of layers. Symmetry considerations and supporting density functional calculations showed that - coming from the respective few-layer symmetry - every other of these sidebands is not Raman but infrared-active. These modes appear in the resonance Raman spectra as a consequence of the in-plane orientation of the A exciton which has the effect of partly decoupling the layers and thus activating the modes in the monolayer picture. Unpublished work on the behavior of the A_{1g} mode in WS_2 materials includes the frequency downshift with increasing temperature that was followed for different diameter nanotube in the range of 100 to 300 K as well as the investigation of the B_{1u}/A_{1g} Raman intensity ratio at nanotube caps - highly ordered and closed ones as well as open ones with different degrees of disorder - that had been characterized by

high-resolution TEM before. Additionally, a peculiar effect that shows WS_2 nanotubes to be quasi-one-dimensional materials despite their multiwalled form and large diameter compared to carbon nanotubes, is the orientation dependence of the Raman scattering cross section with respect to the polarization of the incident laser light [119]. We studied this so-called antenna effect and found that in average the depolarization ratio α_{xx}/α_{zz} is small for smaller nanotube diameters (around 0.1) but is increased in larger nanotubes with diameters above 100 nm where the nanotube diameter to length ratio is larger and the nanotube looses its quasi-one-dimensional character.

In the studied misfit layer materials the out-of-plane A mode is not the Raman feature that deserves the most attention. Instead, the in-plane E mode is subjected to huge changes when going from the pristine parent materials to the MLCs and becomes a rewarding focus of study. In the investigated trigonal prismatic compound $2H$-NbS_2 it has the sulfur atoms move in one of the in-plane directions while the metal atom is displaced in the opposite in-plane direction. Because the Raman spectra of the misfit layer materials can be seen as a superposition of the Raman spectra of the constituents, this mode also exists in $(PbS)_{1.14}NbS_2$ but is seen drastically upshifted by more than 40 wavenumbers. This effect was investigated in comparison with a similar effect in NbS_2 nanotubes intercalated with lead as part of this thesis in Ref. [133]. It can be ascribed to changes in interlayer interaction compared to the pristine materials and there are different models (see Chapter 3.2.) that could account for the observed stiffening of this Raman mode. In another work on the octahedrally coordinated $1T$-SnS_2 nanotubes and the related SnS-SnS_2 misfit layer material [5] the SnS_2 in-plane E_g mode is observed to be overshadowed by Raman modes belonging to the SnS part of the structure.

In the following, I will introduce the papers forming this thesis from a Raman spectroscopic point of view, emphasizing the numerous connections between them. In a first part, I will concentrate on low-dimensional $2H$-WS_2, investigated in this thesis in tubular and planar form. Then, I will present the Raman measurements of the $1T$-SnS_2 and SnS-SnS_2 nanotubes as a transition to the investigation of misfit layer nanotubes. This last section will be devoted to discussing the Raman spectra of $2H$-NbS_2-based misfit layer and intercalated nanotubes, where interlayer interaction, though always playing an important role, is seen to take center stage.

5.2. Low-dimensional WS_2

A Raman spectrum is first and foremost an expression of the basic structural symmetry of the investigated material. The symmetry determines the number of possible vibrational modes, whether they are Raman-, infrared-active or silent and how they behave under differently polarized exciting light. Distortion of this symmetry will broaden the modes, change the Raman frequency and can bring about the relaxation of Raman selection rules. Therefore, the structural properties of WS_2 nanomaterials in particular were discussed in detail in Chapter 1 as a ground work to an understanding of their vibrational characteristics.

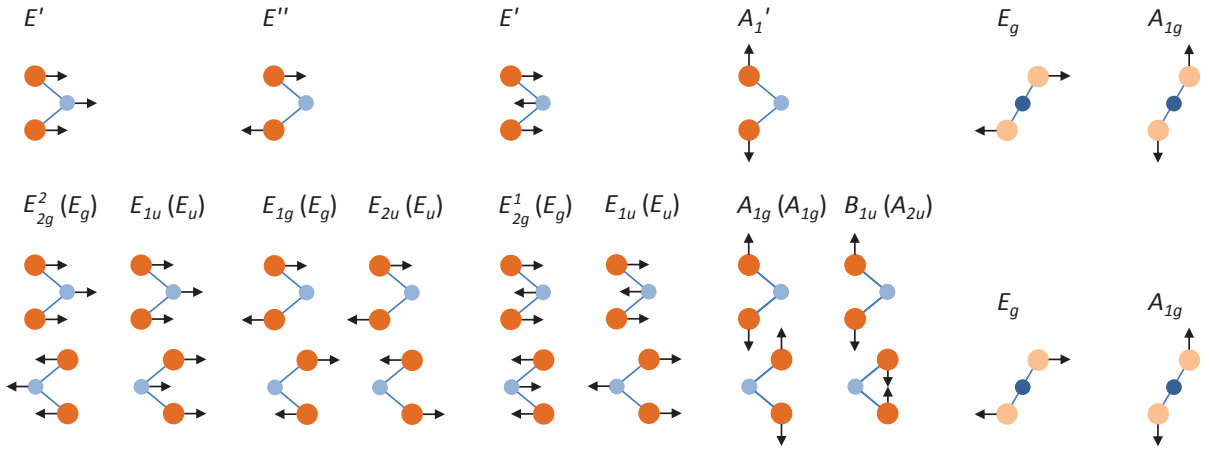

Figure 5.1.: Atomic displacements of the vibrational modes derived from the four Raman-active bulk modes in trigonal prismatically (left) and the two Raman-active modes in octahedrally coordinated layered compounds (right). For the latter, the Raman modes stay the same, irrespective of the layer number. For the former, the monolayer Raman modes (top row) split up for higher layer numbers. In the lower row, bulk and bilayer (in brackets) Raman modes with their respective Davydov pair are depicted. For higher layer numbers there are more and more possibilities for adjacent layer to vibrate with respect to each other. Adapted from Ref. [136].

Bulk 2H-WS_2 crystallizes in the D_{6h}^4 space group (Schönfliess notation: $P63/mmc$) and there are 18 different phonon modes accessible at the Γ-point of the hexagonal Brillouin zone [137]:

$$D_{6h} : \Gamma = A_{1g} + 2A_{2u} + B_{1u} + 2B_{2g} + E_{1g} + 2E_{1u} + E_{2u} + 2E_{2g}$$

Of these, only four are first-order Raman-active, an A_{1g} mode ($421\,\mathrm{cm}^{-1}$) that has sulfur atoms vibrating out-of-plane with a fixed metal atom in the middle, two in-plane modes with E_{2g} symmetry (E_{2g}^1 at $356\,\mathrm{cm}^{-1}$, E_{2g}^2 at $27\,\mathrm{cm}^{-1}$) and an E_{1g} mode ($306\,\mathrm{cm}^{-1}$) which is inactive under the normally employed backscattering configuration. The atomic displacements of these modes are depicted in Fig. 5.1. In the monolayer and an odd number of layers (odd N), where no center of inversion is present, the symmetry is reduced to the D_{3h} point group. Nonetheless, in the following irreducible representation one can identify the same vibrational patterns as in the bulk, see Fig. 5.1.

$$D_{3h} : \Gamma = \tfrac{3N-1}{2}(A_1' + A_2'' + E' + E'') + A_2'' + E',\ N = 1, 3, 5, ...$$

The same holds true for an even number of layers that possess a center of inversion and have point group D_{3d}:

$$D_{3d} : \Gamma = \tfrac{3N}{2}(A_{1g} + E_g + A_{2u} + E_u),\ N = 2, 4, 6, ...$$

The Raman frequencies of the two most accessible first-order Raman modes in layered 2H transition metal dichalcogenide materials, the out-of-plane A and the in-plane E mode around $420\,\mathrm{cm}^{-1}$ and $355\,\mathrm{cm}^{-1}$, respectively, have been shown to change slightly from the monolayer to

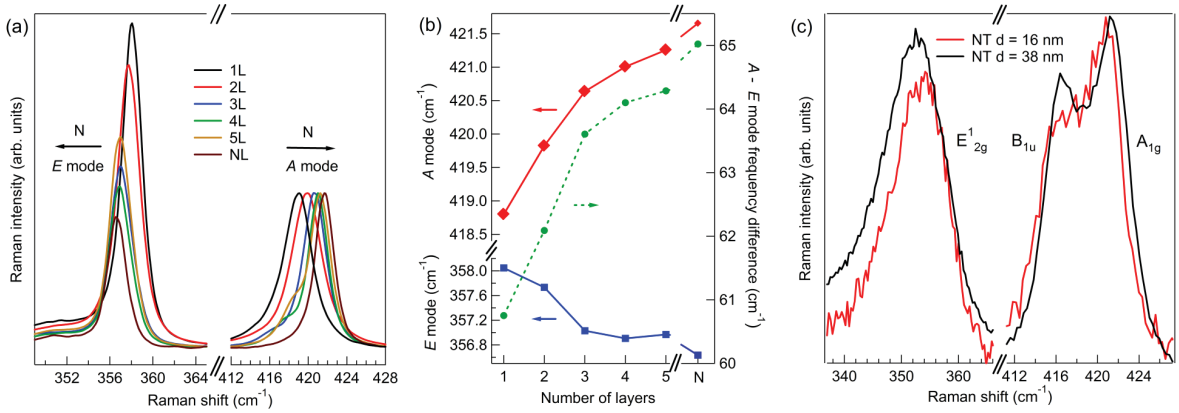

Figure 5.2.: (a) The two main Raman modes of FL-WS_2 are seen to shift apart for increasing layer numbers (off resonance spectra with 457 nm excitation wavelength). (b) Raman frequencies and their difference deduced from (a). (c) The same behavior is observed in a very thin nanotube (d = 16 nm, wall number = 4) compared to a thicker one. Spectra are recorded with 633 nm excitation wavelength, a shoulder to the main A_{1g} mode is identified as the B_{1u} mode.

the bulk depending on the number of layers [138–143]. This was the starting point for my work on few-layer WS_2 and results are shown in Fig. 5.2.(a) and (b). As a consequence of increasing interlayer interaction with additional layers adding a successively increasing restoring force, the out-of-plane A mode Raman frequency is observed to stiffen with increasing N by about 3 cm^{-1} from monolayer to the bulk WS_2 material. Rather unexpectedly, the in-plane E mode displays the opposite trend which is explained in terms of increasing dielectric screening of the long range Coulomb interaction with the number of layers [144]. I observed the same behavior of the above named Raman modes in unusually thin WS_2 nanotubes (wall number of four for the thinner nanotube), see Fig. 5.2.(c) and Ref. [145], but there, another phenomenon is more focus pulling. As a very pronounced low-energy shoulder of the A_{1g} mode, a second mode with almost the same intensity is detected. It had been observed in the Raman spectra of other WS_2 nanomaterials as well and had been attributed mostly to a LA+TA combination mode activated by defects as this sideband was seen to increase in intensity with increasing pressure and decreasing nanotube diameter in WS_2 fullerenes and nanotubes, respectively [26, 146]. In the first paper forming the body of this thesis, Staiger *et al.*, Physical Review B, **86**, 165423 (2012), I was able to show that in fact it is the silent B_{1u} mode that is activated by nanotube curvature and a slight mismatch of adjacent layers. Using a variety of laser excitation energies in the region of both the optical transition energies of the A and the B exciton, where thus a resonant enhancement of the Raman intensities was to be expected, I recorded Resonance Raman Profiles (RRP) of four different diameter nanotubes and a reference powder WS_2 sample. I established a diameter dependence of the first optical transition energy. Coming from the bulk 1.96 eV A excitonic transition energy, with decreasing the nanotube diameter, the transition energy was seen to decrease down to 1.92 eV for a 38 nm diameter nanotube. Also here, nanotube curvature

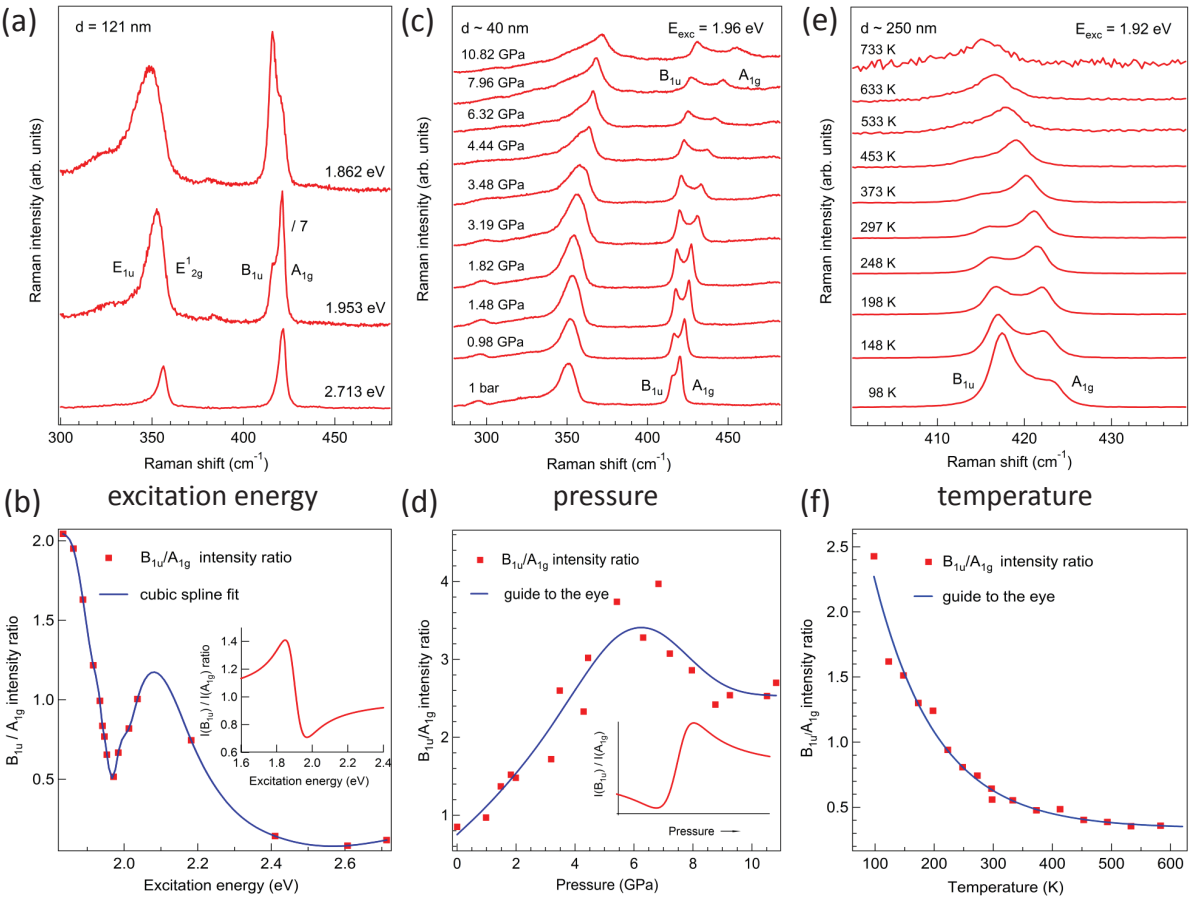

Figure 5.3.: Raman spectra of WS_2 nanotubes with varying excitation energy (a), increasing hydrostatic pressure (c) and temperature (e). For every of these experimental parameters, the B_{1u}/A_{1g} Raman intensity ratio depicted in (b), (d) and (f), respectively, changes drastically due to slightly different resonance conditions of the two modes.

is the decisive factor, in that tensile and compressive strain on the outer and inner side of one triple-layer nanotube wall, respectively, have the net effect of reducing the energy gap between occupied and unoccupied states around the K-point where the excitonic optical transitions take place. In an unpublished work, I recorded Resonance Raman profiles on MoS_2 fullerenes and, for the same reason, also observed a decrease in the first optical transition energy relative to the bulk crystal.

For increasing nanotube diameters, when the structure gradually resembles the unstrained planar crystal and curvature becomes less important, the maximal resonant enhancement of the B_{1u} mode decreases relatively to the maximal resonant enhancement of the A_{1g} mode. For a certain nanotube diameter on the other hand, the Raman intensity ratio B_{1u}/A_{1g} is by no means fixed but is strongly dependent on Raman excitation energy and other external influences like pressure and temperature changes. Figure 5.3.(a) shows some exemplary Raman spectra in different excitation energy ranges of a 121 nm diameter WS_2 nanotube and a plot of the B_{1u}/A_{1g} intensity ratio as a function of excitation energy [Figure 5.3.(b)]. The varying intensity ratio is proven to

be due to slightly differing resonance conditions of the two modes (in the here described case about 20 meV) in the A excitonic transition region around 1.96 eV and an exclusive enhancement of the A_{1g} mode in the higher energy B excitonic transition energy region. As the B_{1u} Raman mode signal finds its origin particularly in the inner nanotube walls, where the curvature is higher than in the walls closer to the nanotube surface, the resonant enhancement will resemble that of a smaller diameter nanotube, with slightly lower excitonic transition energy than the resonant enhancement of the neighboring A_{1g} mode. The information gained from the recording of WS_2 nanotubes Resonance Raman profiles were then applied to the Raman spectra of WS_2 nanotubes under hydrostatic pressure and varying temperature [Fig. 5.3.(c), (d) and (e), (f)]. Apart from an upshift of the Raman modes with increasing pressure and decreasing temperature, strong variation in the intensity ratio of the two out-of-plane modes were detected that had been explained in the case of WS_2 inorganic fullerenes as being due to shape distortions with increasing pressure [146]. I showed that - because both decreasing temperature and increasing pressure will push the excitonic transition of the WS_2 materials towards higher energies - the net effect is the same as for varying excitation energies. In the latter case the relative intensities of two Resonance Raman profiles are scanned through while the sample stays under the same ambient conditions. External influences like pressure and temperature variations change the energetic position of the Resonance Raman profiles and with a fixed excitation energy similar changes in the intensity ratio are observed.

Research on few-layer WS_2 was a logical continuation of the above described work on one hand in light of the increased scientific interest in the field of quasi two-dimensional layered materials and on the other hand because I could benefit from previously obtained knowledge. Again, Raman spectra acquired in resonance with the A exciton were far more interesting to study than those recorded off-resonance and yet again it were the sidebands to the main out-of-plane A mode the deciphering of which comprised the most scientifically interesting phenomena. Results are published in Staiger *et al.*, Physical Review B, **91**, 195419 (2015). In Fig. 5.4.(a) off-resonance (dashed lines) and resonance Raman spectra (full lines) of monolayer to five-layer and bulk-like WS_2 are superimposed and large differences are evident. While the main component at the higher-frequency side stays the same, lower lying sidebands are barely made out in the off-resonance Raman spectra but become prominent in the resonant case. In a delicate fitting procedure, I showed that for a layer number of N there are also N components to the out-of-plane A mode in the few-layer regime until for the pristine and undistorted bulk material only the A_{1g} mode remains. Work then concentrated on tracing back each of the components to a specific vibrational pattern with the help of CASTEP phonon calculations (detailed in Ref. [135] and the visualization of phonon modes in the GaussView software. The findings are depicted in Fig. 5.4.(b) and (c). We showed experimentally as well as theoretically that all the sidebands that are added successively with increasing layer number are following the trend of shifting up in frequency with N due to an increase in interlayer interaction. The lowest lying phonon mode for layer numbers of more than three was seen to saturate in frequency most quickly because the strict out-of-phase pattern of this component brings with it the in-phase displacement of

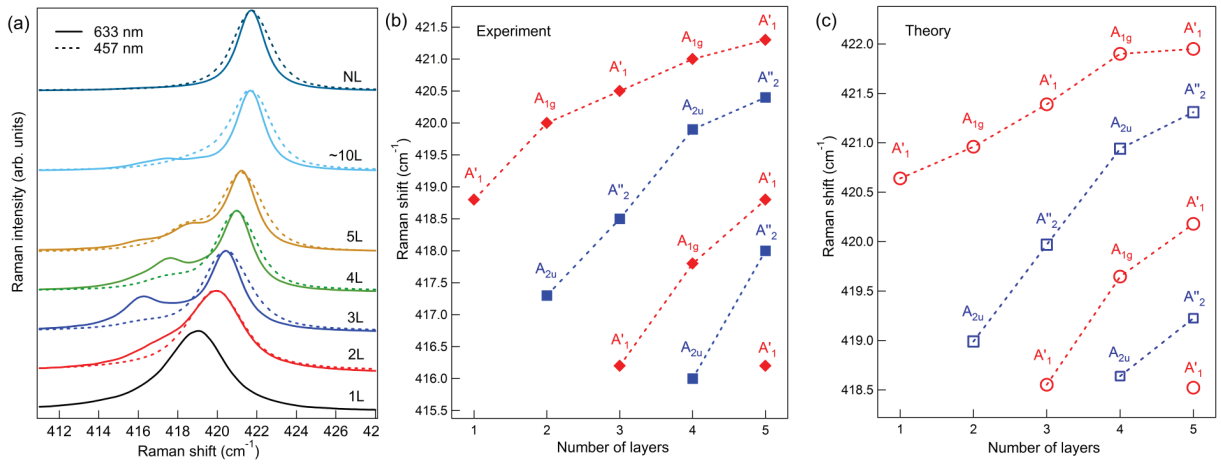

Figure 5.4.: (a) Resonance (full lines) and off-resonance (dashed lines) Raman spectra for few-layer WS_2. (b) Raman frequencies and symmetry assignments for each of the modes identified from (a) via a lorentzian fitting procedure. (c) Calculated Raman frequencies confirming the experimental results. Adapted from Ref. [135].

neighboring sulfur atoms and hence little changes in the interlayer force constants for varying layer numbers.

Furthermore, every second phonon mode was shown to be only infrared-active (A_{2u} symmetry for even, A_1' for odd number of layers, respectively) in the strict picture of few-layer symmetry, but, much to our initial surprise, all of them were identified in the resonance Raman spectra, albeit with weaker intensity than the Raman-active phonon modes. Apparently a resonant effect, the nature of the exciton the phonons couple to was pulled to the focus of attention and a possible explanation was found in the spatial expansion of the A exciton wavefunction. It had been recently shown by photoluminescence measurements for FL-MoS_2 to be oriented entirely in-plane [118], which is theoretically supported by a work by the Wirtz group [111] indeed showing the wavefunction of the A exciton constricted to one layer only. This has drastic consequences for the resonance Raman process. If in resonance with the in-plane A exciton, the Raman cross section is dominated by scattering processes confined to one of the N layers. Thus, the few-layered system has partly to be seen as N decoupled layers. With this, the selection rules of the N-layered system are at least weakened because they are overlaid with the selection rules for N monolayers. In this picture, N monolayer Raman modes become allowed and this is exactly what we see in the resonance Raman spectra of FL-WS_2. The fact that the infrared-active components, from the point of view of the symmetry of the N-layered system, are always weaker in intensity than the regularly allowed Raman components, illustrates that the selection rules in the resonance Raman process are weakened but not completely broken. An article on newly observed first-order resonant Raman modes in FL-MoS_2 [136], which I am a coauthor of, can be seen as a complimentary work. There, it is illustrated how the different expansions of exciton wavefunctions - in-plane for the A and B exciton, not confined to a specific layer for the

C exciton - affect the resonance Raman spectra of few-layer inorganic materials.
In the end, what connects the different investigations carried out on low-dimensional WS_2 materials in the course of this thesis is that the findings have validity for the whole family of inorganic layered materials. Secondly, the close entanglement of electronic structure and vibrational characteristics is made evident in the Raman spectroscopic investigations. For each of the measurement series, the key to the understanding of the observed phenomena - whether it is the nanotube diameter dependence of the resonant enhancement of Raman modes or the appearance of infrared-active modes in FL-WS_2 - was found in the specific electronic features of the respective materials. The exemplary investigated fingerprint A_{1g} frequency region was shown to shed light on the properties of layered inorganic nanostructures far beyond the narrow focus of vibrational characteristics.

5.3. The SnS-SnS_2 system

As a member of the TS_2 family crystallizing in the octahedral configuration of triple layers, SnS_2 nanotubes were investigated and results are presented as part of a joint work in Radovsky *et al.*, Angewandte Chemie, **50**, 12316-12320 (2011) [5]. At the same time, with the simultaneous presence of SnS-SnS_2 ordered superstructures in the available samples, a first encounter with misfit layer structures was made, which laid the basics for the follow-up work on the PbS-NbS_2 system, which I focused on during the last part of my thesis. Raman measurements were performed on nanotubes characterized by TEM, which allowed me to have precise structural information but lower signal-to-noise ratio and on nanotubes characterized by SEM, where only basic structural knowledge was at hand but higher-intensity Raman spectra were obtained. By acquiring Raman spectra of TEM characterized nanotubes as prototypes, later the same types were identified in the higher resolution spectra of SEM characterized nanotubes (see Fig. 5.5.). SnS_2, like TiS_2, adopts the CdI_2 structure type with D_{3d} ($\bar{3}m1$) point group symmetry, thus there are nine normal modes of vibration, the first two of which are Raman-active [147]:

$$\Gamma = A_{1g} + E_g + 2A_{2u} + 2E_u$$

A main difference to the $2H$ family is that, because there is only one layer in the unit cell, there are no so-called Davydov pairs, where neighboring layers have the possibility of moving in- or out-of-phase (like A_{1g} and B_{1u} in WS_2). There is only the A_{1g} mode with atomic displacement vectors just like in the trigonal prismatic coordinated compounds and an E_g mode that has the metal atom fixed and sulfur atoms moving in opposite directions (similar to the E_{2g} mode in the $2H$ family).
Figure 5.5.(a) shows a Raman spectrum taken with 532 nm excitation wavelength of a SnS_2 nanotube in comparison to a $1T$-SnS_2 bulk powder sample. For the latter, both A_{1g} and E_g mode are easily identifiable at 314 cm^{-1} and 205 cm^{-1}, respectively, in accordance with literature values [147–150]. The E_g mode is often at least a magnitude smaller in intensity than the A_{1g} mode. Another peculiarity is the appearance of the infrared-active $A_{2u}(LO)$ mode as a high-

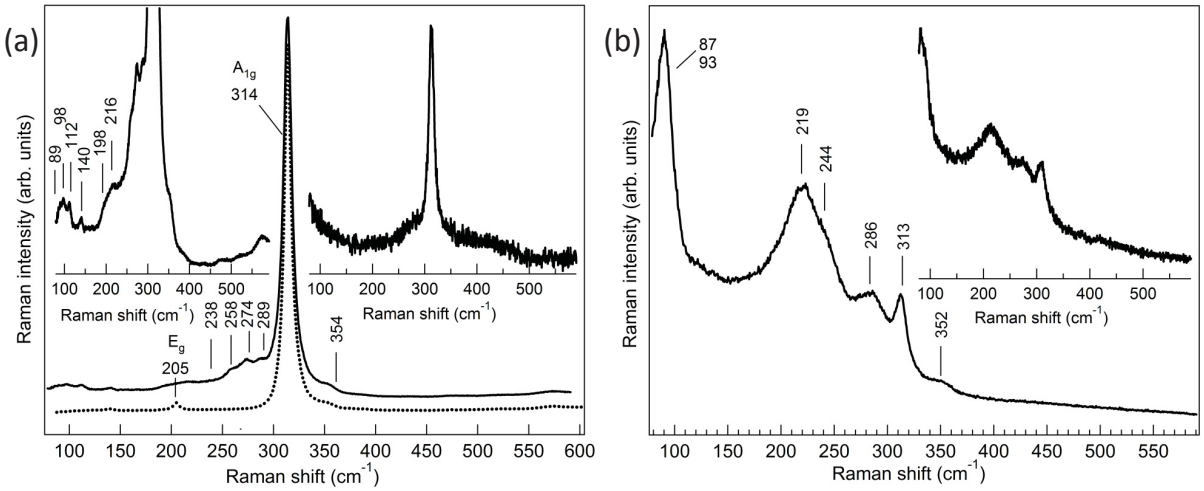

Figure 5.5.: (a) Raman spectrum of a SnS_2 nanotube (diameter $d = 152\,\text{nm}$; analyzed by SEM) in comparison with a Raman spectrum of SnS_2 bulk powder. The two first-order Raman-active modes are denoted with A_{1g} and E_g. Left inset: a zoom-in on the region comprising SnS and SnS_2 difference modes of the nanotube Raman spectrum. Right inset: Raman spectrum of a SnS_2 nanotube ($d = 91\,\text{nm}$; TEM). (b) Raman spectrum of a SnS-SnS_2 ordered superstructure nanotube ($d = 57\,\text{nm}$; SEM). Inset: SnS-SnS_2 ordered superstructure nanotube ($d = 75\,\text{nm}$; TEM). All spectra are taken with 532 nm excitation wavelength at room temperature. Adapted from Ref. [5].

energy shoulder of the A_{1g} mode around $354\,\text{cm}^{-1}$ [149–151]. It is said to be characteristic of the CdI_2 structure type [149] and has been attributed as being due to a Fröhlich interaction induced Raman activation in polar semiconductors in the resonance Raman case [150]. A second tiny Raman feature is the second order difference band at $140\,\text{cm}^{-1}$ [150], that is detected in almost all Raman spectroscopic investigations of SnS_2 and can be found in the left hand inset in Fig. 5.5.(a). The overall appearance of the SnS_2 nanotube Raman spectrum is similar, but whereas in total there is an increased number of small Raman bands on the low-energy side of the A_{1g} mode compared to the bulk spectrum that vary in intensity from nanotube to nanotube, the E_g mode is not easily detected. Instead, in the frequency region between 90 and $300\,\text{cm}^{-1}$, the Raman spectrum comprises low intensity bands of tin monosulfide [152, 153]. As a matter of fact, in the TEM investigation of SnS_2 nanotubes it was revealed that especially closer to the hollow core some SnS layers are always present [154]. This finding can be confirmed by Raman spectroscopy, it was even possible to detect traces of Bi_2S_3 [155] (bismuth was used in the synthesis process as a catalyst [5]). Either the E_g SnS_2 mode is overshadowed by these additional modes, or - because the nanotube curvature possibly revokes the strict $1T$ ordering - there are locally different polytypes with different in-plane mode frequencies. In the $4H$ and $18R$ polytype, for example, the $1T$ E_g phonon branch is folded back onto the Γ-point and more than one mode becomes Raman-allowed [156]. This could account for the smeared out features around the suspected E_g mode frequency in almost pristine SnS_2 nanotubes.

During the work on the SnS-SnS_2 system, most often spectra of the type shown in Fig. 5.5.(b) were encountered. The respective nanotubes or nanoscrolls comprise SnS as well as SnS_2 layers in different orderings with *O-T-T*, *O-T* and *O-T-O-T-T* as the most common ones (*O* for the orthorhombic SnS, *T* for the SnS_2 lattice, respectively, see Chapter 2.3.). Here, the question arose, to what extent the SnS_2 mode frequencies are influenced by the presence of SnS layers, or vice versa, and whether this influence scales with the ratio SnS/SnS_2. Clearly seen in the exemplary SnS-SnS_2 nanotube spectra in Fig. 5.5.(b) is the mode at 313 cm^{-1} with the shoulder at 352 cm^{-1} which can be attributed to the A_{1g} and the A_{2u} mode, respectively, of the SnS_2 part of the structure, with negligible shift compared to the pristine nanotube. Other than that, the spectrum is dominated by features identifiable as belonging to the SnS layers, again, only small shifts are observed. The measured spectra of the SnS-SnS_2 system are hence a confirmation of what is called the rigid band model in describing the electronic structure of such superstructures: the Raman spectra are to a first approximation a superposition of the Raman features of the constituents. However, as will be shown later for the PbS-NbS_2 system, in misfit layer structures, the in-plane mode of the *S-T-S* triple layer is a very sensitive indicator of interlayer interaction, and it is just this mode that, just as in the SnS_2 case, can not be made out in the SnS-SnS_2 nanotube spectra. One has to resort to other pieces of evidence with the small shifts of the out-of-plane modes serving as a first indication of very weak interlayer interaction. Even more so as no frequency differences were detected neither for different orderings of SnS and SnS_2 layers nor for nanotubes and nanoscrolls. To the best of my knowledge there are no Raman spectroscopic reports on SnS-SnS_2, but there is at least one article on lithium-intercalated SnS_2. Alkali metals are prone to donate an electron to neighboring layers and since charge transfer is one of the main routes to explain frequency shifts in intercalation compounds like $LiTiS_2$ [157] the existence of only small (up)shifts in $LiSnS_2$ [158] points in the same direction. A recent paper actually calculates a very small charge transfer of less than 0.1 electrons in the SnS-SnS_2 double layer from the SnS_2 to the SnS layer [79], contrary to the charge transfer direction that is common in other misfit layer systems (see Chapter 3.2.). Finally, the simultaneous and random occurrence of different stacking sequences in the SnS-SnS_2 nanotube synthesis speaks in favor of weak interlayer interaction and consequently for at most small frequency shifts in the combined materials.

5.4. The PbS-NbS_2 system

Work on misfit nanotubes of the type $(PbS)_{1.14}NbS_2$ and of NbS_2 nanotubes intercalated with lead formed the last part of my thesis and results are published in Staiger *et al.*, Physical Review B, **94**, 035430 (2016). I was already familiar with the specifics of 2*H* transition metal dichalcogenides and with the basic questions arising when these materials are hosting intercalants and form misfit layer compounds, respectively. But, as it turned out, the situation is entirely different from the prior work on the SnS-SnS_2 system. 2*H*-NbS_2, like WS_2, has the D_{6h} point

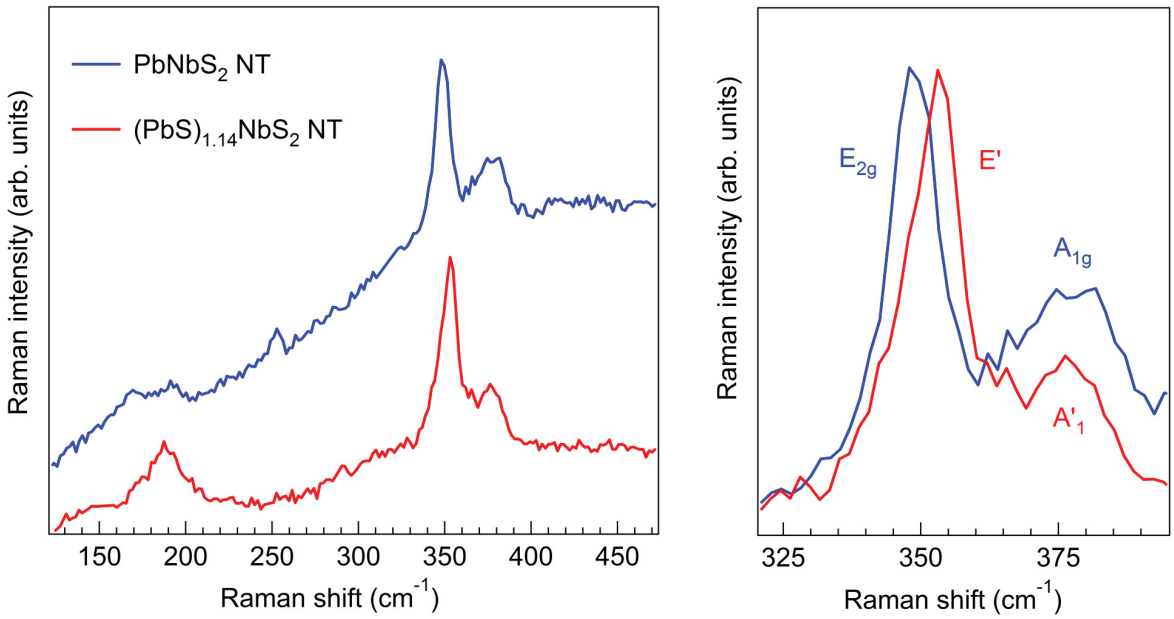

Figure 5.6.: (a) Raman spectra of an exemplary $(PbS)_{1.14}NbS_2$ and a $PbNbS_2$ nanotube. The main in-plane and out-of-plane modes are located around 350 and 380 cm^{-1}, respectively. (b) A closer look reveals subtle differences in the frequency of the Raman modes and their respective symmetry. Both spectra are taken taken with 532 nm excitation wavelength at room temperature.

group and the frequencies of the main A_{1g} and E_{2g} Raman modes are around 379 and 309 cm^{-1}, respectively [159]. In the misfit layer nanotubes, because the NbS_2 layers are separated by a PbS layer in between, is is more accurate to make use of the monolayer D_{3h} symmetry, not accounting for additional structural distortion induced by the intercalant layer and the nanotube curvature. For the measured nanotubes the two Raman modes related to the A_{1g} and E_{2g} mode of the parent material were identified at 378 (A_1') and 353 cm^{-1} (E'). In the $PbNbS_2$ nanotubes, where the parent material symmetry is approximately retained, the same modes were observed at 377 (A_{1g}) and 348 cm^{-1} (E_{2g}). Raman spectra of the two cases are shown in Fig. 5.6. Thus, two main characteristics are seen to distinguish the experimental observations from the results obtained for the SnS-SnS_2 nanotubes. The in-plane E mode is clearly detected in the spectra and is seen to shift up drastically with respect to the parent material, whereas the frequency of the out-of-plane A mode stays almost the same. Clearly, the key to the understanding of this quite unusual strength of frequency shifts has to be found in the characteristics of the interlayer interaction when combining the two materials. Some basic concepts of interlayer interaction have been presented in Chapter 3.2. of this thesis. Niobium disulfide intercalated with lead has not been investigated by Raman spectroscopy before, but while the same holds true for $(PbS)_{1.14}NbS_2$ nanotubes, the bulk misfit system as well as a variety of other misfit layer systems and intercalated layered systems have been subject of research [20, 157, 159–169]. For compounds containing NbS_2 and intercalants other than rare earth metal monochalcogenides

the results are similar to the ones presented here, a strong upshift for the in-plane and little to no change for the out-of-plane mode of the TMD part of the structure is measured [159–162, 166]. Yet, despite intensive discussion and authors presenting several, partly contradicting models, no definite conclusion has been reached as to why this mode-stiffening only occurs for the in-plane Raman mode. Moreover, for NbS_2 misfit layer compounds with rare earth metal monochalcogenides even the out-of-plane A_1' mode shifts up and extra modes start appearing that can not be explained in the context of the simple superposition of Raman modes of the constituents [20, 164]. In contrast, in MLCs containing 1T-TMDs and in intercalated 1T-TMDs, several authors claim to observe a small downshift of the E_g mode with respect to the parent material [157, 160].

Assuming the reasons for the frequency changes are based on the same underlying mechanism for all these compounds, in finding an explanation for the frequency shifts in $PbNbS_2$ and $(PbS)_{1.14}NbS_2$ nanotubes, one has to aspire to bring under the same umbrella also the phenomena observed in other misfit and intercalated layered compounds. The mechanism put forward by a majority of authors for the NbS_2 compounds is that a filling of the NbS_2 d_{z^2} orbital by charge transfer from the intercalant is to be held responsible for the raise in frequency. However, it is not clear why this charge transfer should have a larger impact on the E mode frequency and only little impact on the A mode frequency in $MXNbS_2$. One idea was to consider the orientation of the main lobe of the d_{z^2} orbital: it is oriented perpendicular to the layers, thus the atomic displacements for an in-plane vibrational mode will lead to changes in the chalcogen valence / transition metal d_{z^2} orbital overlap and lead to a subsequent frequency upshift, whereas the same change will not occur for out-of-plane modes [168]. This model can not be applied simultaneously to 1T misfit layer compounds, where small E mode downshifts occur. One has to take into account though that the 1T-TMD orbital the charge is transferred to from the intercalant does not have the same orientation than the trigonal prismatic d_{z^2} orbital. A different approach is presented by Shirai *et al.* [169] and focuses on the changes of intralayer central and noncentral forces upon charge transfer. Again, this model only deals with trigonal prismatic TX_2 compounds and is not applicable to the 1T family.

If the charge transfer mechanism was to be held accountable to the frequency upshift in trigonal prismatic MLC, as a second assumption, the magnitude of the former should be related to the strength of the latter, e.g. large charge transfer should make for large frequency upshifts. Looking at the literature, comparing $MSNbS_2$ [160] and $RSNbS_2$ [161] this seems to be indeed the case, also *stage 2* compounds, where a RS layer is inserted only every second NbS_2 layer and hence a smaller charge transfer is likely, exhibit smaller frequency upshifts than *stage 1* compounds [20]. Having two model systems, $PbNbS_2$ nanotubes (upshift: $39\,cm^{-1}$) and $(PbS)_{1.14}NbS_2$ (upshift: $44\,cm^{-1}$) the magnitude of the charge transfer should thus be similar. As a matter of fact though, as was carried out in detail in Chapter 3.2., the charge transfer expected for $(PbS)_{1.14}NbS_2$ - if there at all - is only a small fraction of the larger charge transfer confirmed for the intercalation compound $PbNbS_2$. The measured frequency upshifts are hence not likely to be caused by charge transfer.

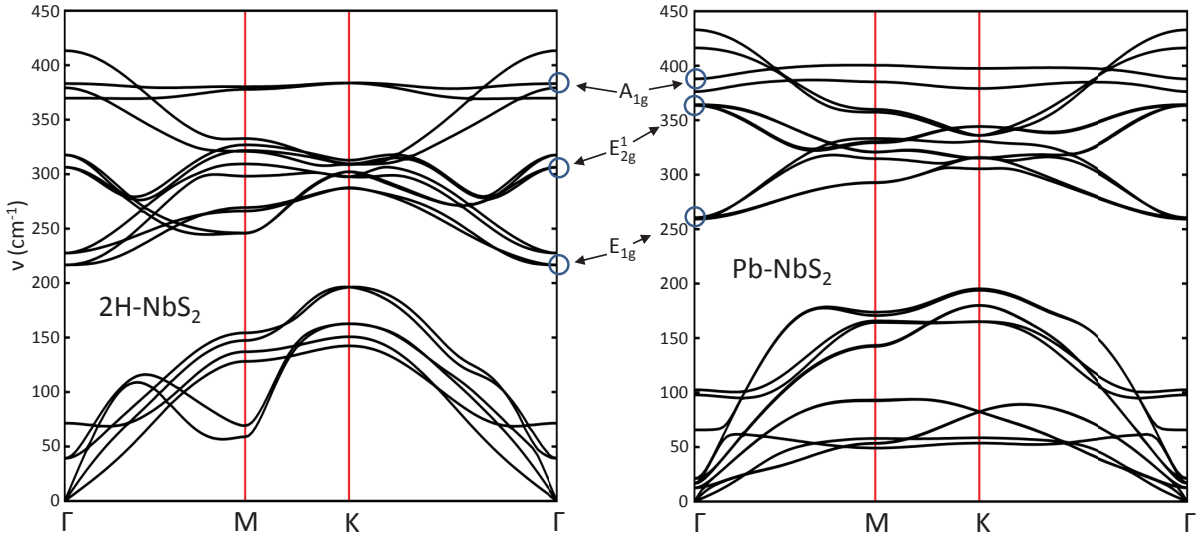

Figure 5.7.: Calculated phonon dispersion of 2H-NbS_2 (a) and $PbNbS_2$ (b).

As a means to elucidate the nature of the vibrational modes in misfit layer compounds, DFT calculations were done in my group. Because it has a much smaller unit cell than the MLC, $PbNbS_2$ was chosen instead of $(PbS)_{1.14}NbS_2$. Calculated Γ-point frequencies in 2*H*-NbS_2 and $PbNbS_2$ are 306 and 356 cm^{-1} for the *E* and 381 and 382 cm^{-1} for the *A* mode, respectively, in very good agreement with the experimental results. The calculated frequencies also imply that interlayer interaction through cationic coupling or metal cross substitution does not play a role in the frequency upshift, as the calculations are performed on the pure, stoichiometric compounds. The calculations also allowed me to visualize the atomic displacement patterns for the phonon modes using the GaussView software. They show that the 2*H*-NbS_2 Raman modes of the parent compound are found again in the intercalated compound without the lead atoms taking part, thus backing up the idea that the Raman spectra can be seen as a superposition of the constituents Raman modes. Extra vibrational modes with the participation of the intercalant layer are not Raman-active. Between 100 and 200 cm^{-1}, experimentally observed Raman features can be attributed to second order and combination modes, and in the case of $(PbS)_{1.14}NbS_2$ also to vibrations of the PbS part of the MLC, see Ref. [133]. Looking at the calculated phonon dispersions of bulk 2*H*-NbS_2 and $PbNbS_2$ in Fig. 5.7. it becomes clear that, e.g., zone-folding effects do not play a role in the frequency upshift of the in-plane mode. Neither does the NbS_2 monolayer nature in $PbNbS_2$, with the NbS_2 layers being separated by intercalant layers, since the NbS_2 monolayer phonon dispersion (not shown) closely resembles the one of the bulk.

We also investigated if the stacking order affects the frequency of the vibrational modes. In the polytype 3*R*-NbS_2, the in-plane mode is also stiffened with respect to 2*H*-NbS_2 [170–172] but our calculations were unable to reproduce this shift. It is thus not likely to be an effect of stacking order but can rather be traced back to the existence of extra niobium atoms intercalated between NbS_2 layers [2, 3]. Also, MLCs with the transition metal in trigonal prismatic

coordination in *CC* [e.g. $(SnS)_{1.17}NbS_2$] or *CF* [e.g. $(PbS)_{1.14}NbS_2$] stacking order [13] (see Fig. 2.2.) seem to exhibit the same frequency trends. This is further supported by calculations done at the Jacobs university in Bremen, where a single slab of NbS_2 sandwiched between two lead atom layers, without the influence of any neighboring NbS_2 layers, was shown to exhibit a similar strength of frequency upshift [173].

The existence of covalent bonds between intercalant and TMD layers is under debate (see Chapter 3.2.) but one would expect them to act more strongly on the frequency of in-plane than out-of-plane modes.

A model not discussed yet in the literature on misfit layer compounds takes into account the charge redistribution in the intercalant layers during the atomic vibrations. In the NbS_2 in-plane *E* mode the movement of negatively charged sulfur atoms along the layer direction will lead to a rearrangement of charges also in the adjacent intercalant layer. In order to restore equilibrium, this charge redistribution will, in turn, act as a restoring force on the sulfur atoms and consequently raise the frequency of the respective vibration. In the case of the out-of-plane *A* mode, because significant charge redistribution will not occur perpendicular to the layer direction or is not possible at all in one-atom thick intercalant layers, the frequency remains unaffected. This hypothesis was tested for $(PbS)_{1.14}NbS_2$ with the finite displacement frozen phonon technique. There, the atomic displacement pattern is divided into small steps and each time the forces acting on the atoms taking part in the vibration is calculated, thus taking into consideration the effect of a possible charge redistribution on the Raman frequencies. Carried out in detail in Ref. [133] the calculations indeed favor this new model, as the in-plane *E* mode frequencies are raised strongly and the out-of-plane *A* mode frequency exhibits only a small downshift with respect to the parent material. Calculations have yet to be performed for semiconducting group IVB compounds in octahedral coordination, where a small downshift for the in-plane mode is seen in the MLCs, thus the question whether the above described concept has validity for all MLCs remains an open question.

In conclusion, the misfit layer systems represent a family of materials, where Raman spectroscopic investigations can yield a lot of information also about the electronic properties. As misfit layer nanotubes have only been synthesized for the first time in recent years [5, 6, 45, 46, 56, 174, 175] further research on the vibrational properties will be of great value.

6 Summary and outlook

In this thesis, I studied nanostructures of inorganic layered materials by Raman and Resonance Raman spectroscopy. Research was done almost always on individual nanostructures with prior characterization by electron microscopy techniques (see Appendix A.1.). Investigated compounds cover all dimensionalities, a variety of materials are combined in misfit layer structures and different stacking types occur in the pristine and misfit compounds. Yet, I was able to show that the discussion of the vibrational properties relies on a few principles that are common to all the studied materials. Furthermore, research revealed just how closely vibrational and electronic properties are intertwined.

By virtue of their triple-layered nature all of the vibrational modes in transition metal dichalcogenides have the atoms either moving out of plane in the stacking c direction or doubly degenerated in the ab-plane. Within the triple layers there are two basic coordinations possible for the transition metal atom in the middle layer, for the group IVA and IVB TMDs this is the octahedral coordination, for the majority of group VB and VIB TMDs it is the trigonal prismatic one. In the octahedrally coordinated compounds there are only two Raman active modes, an out-of-plane A_{1g} mode and an in-plane E_g mode (see Fig. 5.1.). In the bulk structure of the latter, of the four Raman active vibrations, the rigid layer E^2_{2g} mode is of very low frequency and the E_{1g} principally not allowed in the employed backscattering configuration. This leaves the in-plane E^1_{2g} and again an out-of-plane A_{1g} mode as the main fingerprint modes in trigonal prismatically coordinated compounds. These two Raman modes are at the core of every study conducted in the course of this thesis and their characteristics are followed with different dimensionality and stacking order changes, with changes in excitation energy and experimental parameters.

I performed Raman spectroscopy on low-dimensional WS_2, MoS_2 and SnS_2 materials and misfit layer/intercalation compounds SnS-SnS_2, $PbNbS_2$ and $(PbS)_{1.14}NbS_2$. It was the investigation of the A_{1g} mode that in the case of the former revealed the most information, not only about the vibrational characteristics of inorganic layered structures but about their electronic structure as well, especially the nature of the excitons. In the case of the misfit/intercalation compounds, in contrast, the E^1_{2g}/E_g Raman mode was the primary study object and interlayer interaction proved to be the pivotal point of discussion. Thus, obtained results can be divided in two parts as follows:

1) *Pristine systems: A_{1g} mode and excitons.*
Coming from the monolayer A_1' mode, in trigonal prismatically coordinated TMDs, there is a splitting of the out-of-plane Raman mode into a set of alternating A_{1g}/A_{2u} modes in an even and A_1'/A_2'' modes in an odd number of layers. In the bulk, these modes collapse into a Davydov pair of an in-phase Raman active A_{1g} and an out-of-phase silent B_{1u} mode. I established experimentally, for the first time in FL-TMDs, that there are N components to the out-of-plane A mode for N layers in FL-WS_2 [135]. This simple rule is shown to be in principle applicable to all other vibrational modes in few-layer systems [135, 136]. In WS_2 nanotubes, where wall numbers are large enough that it is convenient to use the bulk symmetry in describing the vibrational properties, both the A_{1g} and the neighboring B_{1u} mode are observed and their intensity ratio is shown to be strongly dependent on nanotube diameter [126]. It was assumed previously that a stronger intensity of the B_{1u} relative to the A_{1g} mode in smaller diameter nanotubes was due to an increased density of defects [26]. I showed that one has to delve deep into the electronic properties of the investigated material in order to understand the underlying mechanism that promotes the appearance of the B_{1u} mode in WS_2 nanotubes and explains the varying intensity ratio with nanotube diameter. By using a large set of excitation wavelengths in the region of the first optical transition energies I recorded Resonance Raman profiles of four different diameter WS_2 nanotubes and a bulk reference sample. Not only was the B_{1u}/A_{1g} intensity ratio observed to change with diameter but even more so with excitation wavelength. The excitation energy for which each of the two modes reached their intensity maximum turned out to possess a slight offset with this energy difference again depending on the diameter. Thus, the changes in intensity ratio with excitation energy were proven to be due to slightly different resonance conditions of the two modes. I was able to trace back this difference to a diameter dependence of the A excitonic transition energies. By reducing the nanotube diameter, the curvature of the nanotube walls is increased and as a combined effect of tensile stress on the outer and compressive stress on the inner side of each of the triple-layered nanotube walls the lowest conduction band state is brought down, hence reducing the first optical transition energy. This has also been used to explain the lower excitonic transition energy found by Resonance Raman spectroscopy in fullerene-like MoS_2 with respect to a bulk sample. As the appearance of the formally silent B_{1u} mode in WS_2 Raman spectra is assumed to be a result of strain and mismatch of adjacent layers which plays a role particularly in the inner, smaller diameter nanotube walls, the resonance condition for the B_{1u} mode is met always at the low-energy side of the excitonic transition energy derived from the A_{1g} Raman mode which leads to the observed strong dependence of the B_{1u}/A_{1g} intensity ratio on nanotube diameter and excitation energy. This model was then later confirmed when discussing Raman spectra of WS_2 nanotubes under increasing hydrostatic pressure and temperature. There, instead of changing the excitation energy for a fixed nanotube diameter and corresponding transition energy, the external factors change the transition energy and, using a fixed excitation energy, similar variations of the B_{1u}/A_{1g} intensity ratio are observed [126]. It is likely that the effect of every external influence on the B_{1u}/A_{1g} intensity ratio in WS_2 nanotubes, for instance by external doping or the application of voltage, is to be

explained along similar lines. A recent work [176] is in excellent agreement with the observed pressure dependence of Raman modes, particularly of the A_{1g} mode, in WS_2 nanotubes and confirms the findings presented in this thesis.
In the resonance Raman spectra of FL-WS_2 all of the N components to the out-of-plane mode, Raman-active and formally infrared-active ones, are detected. Again, this can only be explained by the specifics of the electronic structures of the investigated TMDs, particularly the nature of the excitons. The activation of infrared-active phonons in the Raman spectra is an indication of a relaxation of Raman selection rules. The model put forward in my work on FL-WS_2 is evidence of the in-plane orientation of the A exciton in FL-TMDs confirming recent studies [111, 118]. In a simple picture, during the resonance Raman process the phonons couple to one layer only and are thus subjected to the selection rules of N partly decoupled layers. As a result, selection rules in the N layered system are weakened and low-intensity infrared-active phonons are observed in the Raman spectra. As Ref. [136] points out, this will likely not be the case for measurements in resonance with the C exciton which is found to be stretched out in all three dimensions. Recently, we identified first-order Raman modes in FL-MoS_2 that only appear with considerable intensity when the sample is excited in resonance with the C exciton [136]. The insights presented should be transferable to FL-WS_2 as well, where first measurements indicate again a fine structure of these modes that is not seen in FL-MoS_2.

2) *Misfit/intercalation systems: E^1_{2g}/E_g mode and interlayer interaction.*
As an introductory work to Raman spectroscopy on misfit layer nanotubes, Raman spectra of almost pristine SnS_2 and SnS-SnS_2 misfit nanotubes were compared. I was able to prove that the misfit system spectra can be interpreted in terms of a superposition of the Raman modes of the constituents. Almost identical A_{1g} mode frequencies in the two compounds lead me to the conclusion that interlayer interaction was weak in the misfit system, a result that was later confirmed by theoretical studies [79]. However, the in-plane SnS_2 E_g mode was not identified in the SnS-SnS_2 spectra. The related in-plane E^1_{2g} of the trigonal prismatic compounds turned out to be the most sensitive indicator of interlayer interaction in misfit layer systems, so it would be of interest whether under certain experimental conditions the E_g mode in SnS-SnS_2 is discernible. This could be the use of a different excitation energy or low-temperature measurements.
In the main work on misfit layer nanotubes, the system $PbNbS_2$ and $(PbS)_{1.14}NbS_2$ was thoroughly investigated. In comparison with literature data on the parent $2H$-NbS_2 material I observed a drastic upshift of the in-plane modes in the misfit/intercalated nanotubes and a nearly constant out-of-plane A mode frequency. The charge transfer mechanism held accountable for this shifts by a majority of previous studies was put to the test and shown to not satisfactorily explaining the similar in-plane E mode upshifts in both $PbNbS_2$ and $(PbS)_{1.14}NbS_2$ nanotubes. As charge transfer is weaker in $(PbS)_{1.14}NbS_2$ than in $PbNbS_2$ but the upshift is slightly stronger in the former, this apparent contradiction calls for an alternative approach. A number of interlayer interaction mechanisms such as non-stoichiometry, metal cross substitution and covalent bonding as well as Raman spectra of other misfit compounds were discussed. To support the

experimental results, a number of DFT calculations on 2*H*-NbS_2 and $PbNbS_2$ were performed and found to be in very good agreement with experiment. In the end, finite-displacement frozen phonon calculations on the PbS-NbS_2 system provided evidence that during in-plane movement of the NbS_2 part charge in the adjacent PbS layer is being redistributed and the resulting restoring forces raise the in-plane frequency through interlayer interaction.

The PbS-NbS_2 system is only an example of the ever growing number of misfit layer nanostructures. Raman studies on newly synthesized *M*S-TaS_2 [46] nanotubes, judging from their similarity to the structural and electronic properties of *M*S-NbS_2, are likely to yield similar results. In contrast, research on misfit systems should continue in the direction of lanthanide-based misfit nanotubes like *Ln*S-TaS_2 NTs [174] and especially nanotubes where the transition metal dichalcogenide is CrS_2 [45, 56, 175]. For these compounds charge transfer is established and could well lead to additional shifts in the Raman spectra. Moreover research on CrS_2-based misfit compounds should present an interesting experimental and theoretical challenge as the layered bulk CrS_2 compound is not known to exist.

Appendices

A. Experimental methods

A.1. Experimental procedure

Apart from the experiments on few-layer WS_2, the work in this thesis was largely done in collaboration with the group of Prof. Tenne at the Weizmann Institute of Science (WIS) in Israel. This group specializes in the synthesis and characterization of inorganic nanotubes and has done a vast amount of pioneering work in the field. The joint goal of this collaboration was to investigate individual inorganic nanotubes by Raman spectroscopy with simultaneous precise knowledge of their inner structure. This method differs from the way Raman spectroscopic investigations are normally carried out on carbon nanotubes, where one is challenged to extract knowledge about different diameter and chirality nanotubes from ensemble measurements. Having all the structural information prior to Raman measurements allowed me to be sensitive to details like the small differences in Raman frequency of the in-plane mode of $PbNbS_2$ and $(PbS)_{1.14}NbS_2$ nanotubes. As several nanotube types also in the SnS-SnS_2 system are often synthesized in the same batch, in the future, with one simple Raman measurement one will be able to distinguish between the different types. Most of the nanotubes investigated here were synthesized by Gal Radovsky, a PhD student in Prof. Tennes group at the time, whom I worked most closely with. During the time of our collaboration we developed an understanding of each others work and, most importantly, ways to simplify the Raman measurement process. In the end, when I received new samples from Gal they had already been characterized by scanning electron microscopy (SEM), transmission electron microscopy (TEM), electron diffraction, energy-dispersive X-ray spectroscopy (EDS) and had been marked on the underlying substrate by focused ion beam deposition (FIB), so that I was able to begin my work with all the information necessary. In Fig. A.1.(a) an exemplary SnS-SnS_2 nanotube on a carbon coated Cu substrate is shown, surrounded by a platinum circle and a roman cipher to have a common numbering, together with a high resolution TEM picture that identifies the nanotube to be of the *O-T-T* type and a complimentary diffraction image. Starting from an easy-to-identify center of the sample, with the help of a low magnification SEM map with an overlaid Cartesian plane indicating the location of each of the nanotubes, I was able to quickly find the desired position under the optical microscope and start the Raman measurements. As it became evident that the originally used TEM substrate was especially prone to be ruptured due to laser heating, the then used Si_3N_4 nitride TEM grid allowed for slightly higher laser powers without damaging the substrate. To make sure that neither the focused ion beam deposition of platinum circles nor

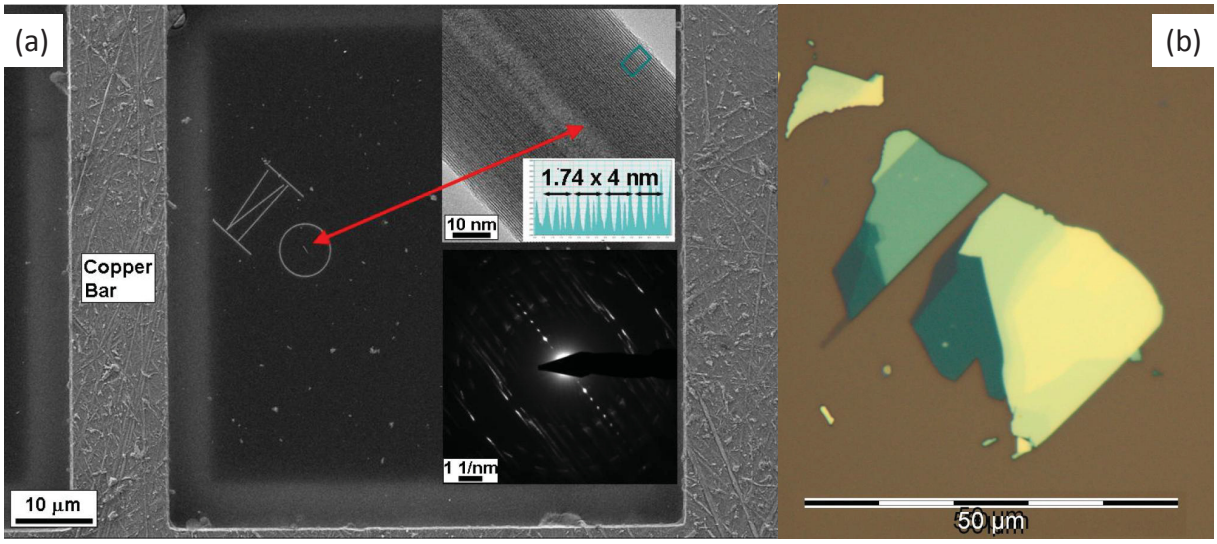

Figure A.1.: (a) Individual nanotubes were placed on a TEM grid, encircled and numbered with FIB deposition. Supplementary information like the high resolution TEM image, the line profile and the diffraction image shown in the insets were available prior to the Raman spectroscopic investigation (picture from Ref. [5] Supporting Information). (b) Before performing Raman spectroscopy, I identified few-layer flakes of WS_2, like the one shown here, under the optical microscope.

the TEM analysis did damage or change the structure of the nanotubes, in the beginning of the joint work, an exemplary WS_2 nanotube that had only been characterized by SEM was sent to Berlin, where we performed Raman measurements before sending it back for TEM characterization in Israel (operation power was 120 keV). As shown in Ref. [126], a Raman spectrum taken after the nanotube was again sent to Berlin did not show any of the Raman features altered in any way. Thus, from then on, nanotubes were routinely analyzed by TEM before performing Raman measurements. In the framework of a soon to begin GIF (German-Israeli Foundation for Scientific Research and Development) project we envision to extend this mode of collaboration by studying the individual nanotubes sequentially by moving them from the WIS to the TU Berlin and then to Jülich for Cs corrected TEM/STEM analysis.
In the case of the work on WS_2 nanotubes the focus did not lie so much on the TEM characterization. For establishing the diameter dependence of the first optical transition energy [126] it was only necessary to prepare individual nanotubes, making sure by SEM characterization that a larger range of diameters was covered. The same applied for the unpublished work on the diameter dependence of the strength of the antenna effect. During the work on SnS_2 and SnS-SnS_2 nanotubes, TEM characterization was established as a complimentary tool to the Raman measurements, as from both methods differences between pure SnS_2 and misfit layer nanotubes as well as mixed cases were unambiguously identified. Finally, for research on the misfit PbS-NbS_2 system, the combination of TEM and Raman investigations was absolutely vital. More or less as a side product, together with $(PbS)_{1.14}NbS_2$ nanotubes, $PbNbS_2$ nanotubes had been

synthesized which were detected in the TEM images because of the different periodicity of the layers. In the Raman spectra, the two types exhibit very similar features and without the prior knowledge could have been easily mistaken for one and the same sort of misfit nanotubes. Being aware of the difference made me sensitive to the small differences in Raman frequencies of related modes. Now, not only does one single Raman measurement suffice to tell whether one has a real misfit layer nanotube at hand or a nanotube intercalated with lead (often both types are synthesized in the same batch). Moreover, the two model systems were an interesting study object to test traditional beliefs in explaining the unusually high frequency shifts with respect to the transition metal dichalcogenide parent material [133].
For my work on few-layer WS_2 I received samples from the University Duisburg-Essen, where a WS_2 crystal acquired from *hq graphene*, Netherlands - Groningen had been mechanically exfoliated onto an SiO_2/Si wafer. I then searched the wafer for appropriate WS_2 flakes and identified approximate layer numbers by optical contrast measurements prior to Raman measurements. One example of such a flake is depicted in Fig. A.1.(b). After the Raman measurements, layer numbers were confirmed by atomic force microscopy scans.

A.2. Raman spectroscopy: experimental details

Raman spectra of low-dimensional transition metal dichalcogenides were acquired, with the exception of pressure and temperature measurements, at ambient conditions and always in backscattering geometry. Apart from the work on MoS_2 inorganic fullerenes where ensemble measurements in solution were done in a macro-optic setup, confocal μ-Raman spectroscopy of individual nanoparticles was the method of choice. The work on WS_2 nanotubes was largely done employing a triple monochromator Dilor XY800 Raman system with a 1800 lines/mm grating in subtractive mode, a 100x objective (numerical aperture of NA= 0.95) and a nitrogen-cooled charge-coupled device. The acquisition of Resonance Raman profiles required a combination of different laser excitation energies - for this undertaking an ArKr ion laser, a variable frequency dye laser (DCM dye) and a TiSa solid-state laser were used to cover the whole WS_2 A and B excitonic energy range. Measurements were always done such that the nanotube orientation was parallel to the linear polarization of the incoming laser light. The limitation of laser excitation power to less than 150 μW to avoid sample heating brought with it accumulation times of 30 to 300 s. In order to be able to compare WS_2 NT Raman cross sections depending on the excitation energy, the non-resonant Raman signal of CaF_2 was recorded after each nanotube Raman measurement.
Raman measurements on FL-WS_2 were performed with a LabRAM HR800 Raman spectrometer equipped with notch filters suppressing the Rayleigh scattered light. A diode laser emitting at 457 nm was used for off-resonance Raman and a HeNe laser with an excitation wavelength of 633 nm for resonance WS_2 Raman measurements. The other experimental conditions were similar to the WS_2 nanotube measurements. In addition to the high spectral resolution of

less than $1\,\mathrm{cm}^{-1}$ I made use of the subpixel mode offered by the LabSpec acquisition software (detailed description, see Ref. [135]) that by providing more data points per wavenumber gave an overall rounder shape to the Raman peaks, which was of high value in the fitting procedure. The SnS-SnS_2 nanotubes were also investigated using a LabRAM HR800 Raman spectrometer and in this case the laser system chosen was a frequency doubled Nd:YAG laser emitting at 532 nm, closer to the optical transition energies of SnS_2 than the red excitation wavelengths used for the WS_2 materials. Here, special care had to be taken for the measurements of nanotubes placed not on the standard SiO_2 substrate but on TEM grids, where the carbon coated copper substrate was prone to rupturing and laser powers had thus to be reduced to $120\,\mu$W and less. The same held true for the TEM characterized NbS_2-based misfit layer nanotubes. Due to them being rather poor Raman scatterers (partly because of the metallic nature of NbS_2) the 1800 lines/mm was exchanged for a 600 lines/mm grating to achieve higher signal-to-noise ratio at the expense of a lower spectral resolution of around $2\,\mathrm{cm}^{-1}$. Accumulation times were still high and exceeded 20 minutes in most cases.
The pressure Raman measurements on agglomerated WS_2 nanotubes were performed by Peter Rafailov using a gasketed diamond-anvil cell. Details can be found in Ref. [126]. For temperature measurements I used a Linkam heating and freezing stage, the coolant was liquid nitrogen. Since the objective-sample distance was bigger than in the other experiments, a far-distance objective (80x magnification, NA= 0.75) came to use.
For all Raman measurements performed in this thesis, the known spectral lines of a neon lamp were used as a calibration standard.

A.3. Basics of Raman spectroscopy

One of the ways light interacts with matter is through scattering processes. Thereby the light is either scattered elastically (e.g. by defects) and retains its energy or inelastically, losing or gaining a quantized portion of energy in the event. This latter process is called Raman effect after its discoverer, C.V. Raman [177, 178], who went on to receive the Nobel prize in physics in 1930. Today, it is one of the primary experimental methods especially in solid state physics. Its contactless and non-destructive nature and the wealth of information the spectra have to offer makes it an ideal analysis tool for research on novel materials and Raman spectroscopy has therefore been the main method of choice in this thesis.
Let us consider an electromagnetic wave traveling through a medium

$$\vec{E}(\vec{r},t) = \vec{E}(\vec{k}_i,\omega_i)\cdot\cos(\vec{k}_i\cdot\vec{r}-\omega_i t) \tag{A.1}$$

$\vec{E}(\vec{r},t)$ will induce a time-dependent polarization $\vec{P}(\vec{r},t)$ in the medium with the same frequency ω_i and wavevector $\vec{k}_i$,

$$\vec{P}(\vec{r},t) = \vec{P}(\vec{k}_i,\omega_i) \cdot \cos(\vec{k}_i \cdot \vec{r} - \omega_i t) \tag{A.2}$$

The strength of the polarization is determined by the material's electric susceptibility χ, which can be altered periodically by atomic vibrations that are excited thermally at temperatures above zero. The amplitude of these vibrations $\vec{u}(\vec{q},\omega_0)$, with wavevector $\vec{q}$ and vibrational frequency ω_0, is normally much smaller than the lattice constants of the material. This allows us to expand χ in a Taylor series with respect to the atomic vibrations $\vec{u}(\vec{r},t)$=$\vec{u}(\vec{q},\omega_0)$·cos($\vec{q}\cdot\vec{r}-\omega_0 t$)

$$\chi(\vec{k}_i,\omega_i,\vec{u}) = \chi_0(\vec{k}_i,\omega_i) + \frac{\delta\chi}{\delta\vec{u}}_0 \vec{u}(\vec{r},t) + ... \tag{A.3}$$

where the first term is an expression of the unperturbed susceptibility χ_0 and the second term represents the perturbation of the susceptibility by the atomic vibrations. The induced polarization of the material through the propagating electromagnetic wave can thus be decomposed into a polarization wave P_0 that is in phase with the incident radiation and two polarization waves $P^{\pm}_{ind}$ where the atomic vibrations increase or decrease the frequency and wavevector of the incident radiation. This is expressed by [179]:

$$\begin{aligned}\vec{P} = P_0 + P^{\pm}_{ind} = \chi_0(\vec{k}_i,\omega_i) \cdot \vec{E}(\vec{k}_i,\omega_i) \cdot \cos(\vec{k}_i \cdot \vec{r} - \omega_i t) + \\ \frac{1}{2}(\frac{\delta\chi}{\delta\vec{u}})_0 \vec{u}(\vec{q},\omega_0) \cdot \vec{E}(\vec{k}_i,\omega_i) \times [\cos((\vec{k}_i+\vec{q})\cdot\vec{r} - (\omega_i+\omega_0)t) + \cos((\vec{k}_i-\vec{q})\cdot\vec{r} - (\omega_i-\omega_0)t)]\end{aligned} \tag{A.4}$$

The first term describes the elastic Rayleigh scattering; the electromagnetic wave travels through the medium basically unperturbed. The second term describes the inelastically Raman scattered light; the electromagnetic wave leaving the medium has its frequency and wavevector altered by virtue of the modulation of the electric susceptibility by the atomic vibrations. Either it has its wavevector and frequency decreased by $\vec{k}_S = (\vec{k}_i - \vec{q})$ and $\omega_S = (\omega_i - \omega_0)$ (Stokes radiation) or increased by $\vec{k}_{AS} = (\vec{k}_i + \vec{q})$ and $\omega_{AS} = (\omega_i + \omega_0)$ (anti-Stokes radiation). As an important condition, Raman scattering will only occur in a material if the polarizability changes during the lattice vibration - $(\delta\chi/\delta\vec{u})_0 \neq 0$ - as can be seen from Equation A.4.
From a microscopic point of view, the atomic vibrations, much like the photons of the electromagnetic wave, have particle like character, are quantized, and are commonly called phonons. The Raman scattering is a three-step process involving photons, electrons and phonons. First, an incident photon with energy $\hbar\omega_i$ excites an electron into an intermediate (either virtual or excited) state, creating an electron-hole pair. Subsequently, this electron-hole pair now can mediate between the incident photon and the atomic vibrations and is scattered in another state thereby generating or annihilating a quantized phonon. Finally, electron and hole recombine and a scattered photon $\hbar\omega_s = \hbar(\omega_i \pm \omega_{ph})$ is sent out that has its energy diminished (Stokes-

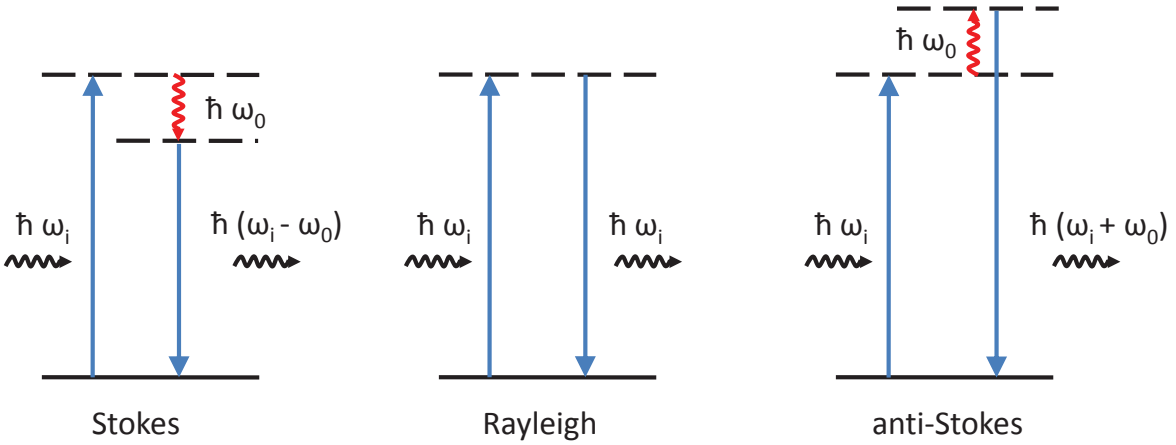

Figure A.2.: Sketch of the Raman process in comparison with the Rayleigh process, where no phonons are involved, in the middle. In the Stokes case a phonon is created and the outgoing light has a smaller energy than the incoming, in the anti-Stokes process a phonon is annihilated and the outgoing light possesses a higher energy. Starting from the ground state (solid line), all other states (dashed lines) can either be real (resonant case, see Fig. A.3.) or virtual.

process) or enlarged (anti-Stokes-process) by the energy of a phonon. This is schematically depicted in Fig. A.2. with the Rayleigh process, where no phonon is involved in the elastic scattering process, shown in the middle for comparison. While the Rayleigh process is by far the dominant one in light scattering by solids, Stokes scattering normally has a higher cross section than anti-Stokes scattering because, as a necessary condition for the anti-Stokes process to occur, a phonon must already be excited in the material in order to be annihilated in the Raman process. In this thesis, Stokes scattering of inorganic nanomaterials is recorded and the Raman shift between the frequency of the incoming and the outgoing photon is measured in reciprocal centimeters (cm^{-1}).
The relationship $\omega(\vec{q}_{ph})$ between the phonon's frequency ω_{ph} and momentum $\vec{q}_{ph}$ is called phonon dispersion and allows one to track the energy of a phonon principally anywhere in the Brillouin zone of a material (see Fig. 5.7.). As Raman scattering requires energy and momentum conservation,

$$\hbar\omega_i - \hbar\omega_s \pm \omega_{ph} = 0, \qquad \hbar\vec{k}_i - \hbar\vec{k}_s \pm \vec{q}_{ph} = 0 \tag{A.5}$$

using visible light where the photons' momentum is much smaller than the dimension of the Brillouin zone, Raman scattering as employed in this thesis only probes zone-center Γ-point phonons with $\vec{q}_{ph} \approx 0$. Still, the Raman spectral features offer a unique fingerprint of a material and one can follow any outside influence, be it temperature, pressure, strain or atomic imperfections by simply looking at the vibrational frequencies.

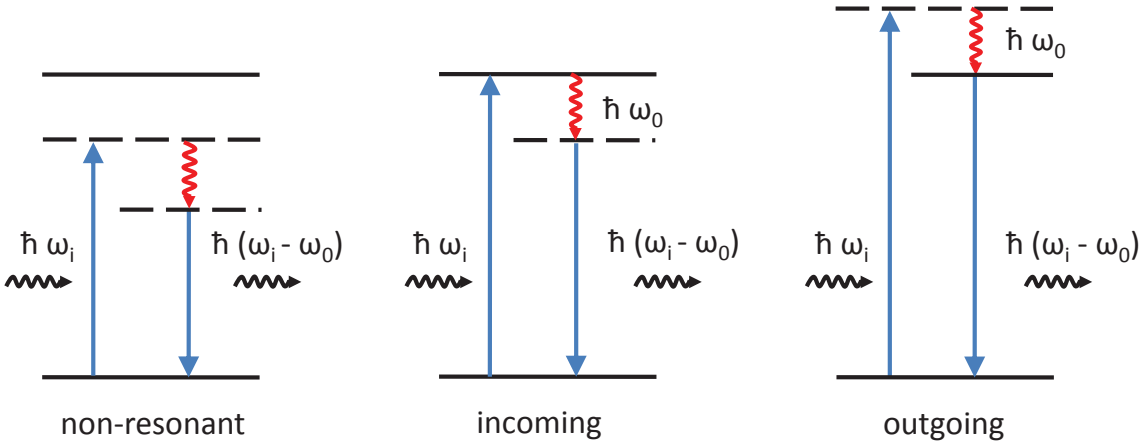

Figure A.3.: Sketch of the Resonance Raman process in comparison with the non-resonant Stokes process on the left. Either the incoming light excites the electron into a real state (solid line, incoming resonance) or a real state is hit after a phonon has been created (outgoing resonance). In both cases, the Raman intensity is resonantly enhanced.

A.4. Basics of Resonance Raman spectroscopy

The information that one can extract from the characteristic phonon frequencies is not everything Raman spectroscopy has to offer. While ω_{ph} is independent of the excitation energy, changing E_{exc} will drastically influence the Raman scattering efficiency, opening up the possibility to deduce the energy of the optical transitions of a material. In most cases the intermediate state in the Raman process will be a virtual state. But by tuning the laser energy such that the intermediate state before or after the interaction with a phonon is an eigenstate of the system, the Raman intensity is enhanced, sometimes by several orders of magnitude. This is called resonance Raman scattering and the different contributions to this process are illustrated in Fig. A.3. Taking into account only the dominant Stokes scattering, if the excitation energy $\hbar\omega_i$ matches the transition to a real state incoming resonance occurs, outgoing resonance describes the case where the excited electron is scattered into an eigenstate of the system before electron-hole recombination.

Formally, the resonance phenomenon can be derived from the time-dependent pertubation theory resulting in "Fermi's Golden Rule". The transition probability from an initial state by a pertubation brought about by an incoming photon $\hbar\omega_i$ into an excited state in the region of an eigenstate of the system is proportional to the Raman scattering probability P_{ph} [179]

$$P_{ph} \approx \left(\frac{2\pi}{\hbar}\right)\left|\frac{\mathcal{M}_{e-r,o}\mathcal{M}_{e-ph}\mathcal{M}_{e-r,i}}{(\hbar\omega_i - E_{ii} - i\Gamma)(\hbar\omega_i - \hbar\omega_{ph} - E_{ii} - i\Gamma)}\right|^2 \tag{A.6}$$

Here, $\mathcal{M}_{e-r,i}$, $\mathcal{M}_{e-r,i}$ and $\mathcal{M}_{e-ph}$ are the matrix element for the interaction of the electrons with the incoming and outgoing radiation and the electron-phonon interaction, respectively.

The first term in the denominator becomes small for incoming, the second term for outgoing resonance. In both cases the Raman intensity is resonantly enhanced. The empirical broadening factor Γ prevents the unphysical situation of the denominator becoming zero and can include the linewidth due to the finite lifetime of the intermediate electronic states as well as the broadening resulting from scattering by crystal imperfections. P_{ph} has thus two contributions with their maxima separated by the phonon energy $\hbar\omega_{ph}$ usually smeared out by Γ.
Resonance Raman spectroscopy has been brought to use in this thesis in two ways. By continuously tuning the exciting laser over a wide range of energies it is possible to record Raman Resonance Profiles (RRP) of a system and derive optical transition energies (incoming resonance) employing Equation A.6. [126]. Secondly, this knowledge can then be used in selecting the best experimental conditions for reducing the signal-to-noise ratio in a Raman spectroscopic investigation. Additionally, it appears that measuring in resonance can have the effect of relaxing the Raman selection rules giving access to modes otherwise not seen in Raman spectra recorded far from resonance [135].

B. Papers as published

B.1. Physical Review B 86, 165423 (2012)

PHYSICAL REVIEW B **86**, 165423 (2012)

Excitonic resonances in WS_2 nanotubes

Matthias Staiger,[1,*] Peter Rafailov,[2] Konstantin Gartsman,[3] Hagen Telg,[4] Matthias Krause,[5] Gal Radovsky,[3] Alla Zak,[6] and Christian Thomsen[1]

[1]*Institut für Festkörperphysik, Technische Universität Berlin, Hardenbergstraße 36, 10623 Berlin, Germany*
[2]*Institute of Solid State Physics, Bulgarian Academy of Sciences, 72 Tzarigradsko Chaussee Boulevard, 1784 Sofia, Bulgaria*
[3]*Department of Materials and Interfaces, Weizmann Institute of Science, Rehovot 76100, Israel*
[4]*Center for Integrated Nanotechnologies, Los Alamos National Laboratory, Los Alamos, New Mexico 87545, USA*
[5]*Helmholtz-Zentrum Dresden-Rossendorf, Institute of Ion-Beam Physics and Materials Research, 01314 Dresden, Germany*
[6]*Holon Institute of Technology, 52 Golomb Street, P.O. Box 305, Holon, Israel*

(Received 16 July 2012; revised manuscript received 14 September 2012; published 12 October 2012)

Resonance Raman profiles of WS_2 nanotubes of different diameter are presented. We show that the A excitonic transition energy lies below the bulk value and is increasingly redshifted with decreasing diameter of the nanotubes. The findings are attributed to strain effects associated with the curvature of the nanotube walls. A silent Raman mode, the B_{1u} mode, is disorder enhanced in the Raman spectra of WS_2 nanomaterials. We discuss the development of the relative intensities of the B_{1u} mode and the nearby A_{1g} mode with nanotube diameter, excitation energy, and hydrostatic pressure in terms of a slight difference in resonance condition.

DOI: 10.1103/PhysRevB.86.165423 PACS number(s): 78.30.−j, 63.22.Gh, 71.35.Gg

I. INTRODUCTION

In the field of nanoscale research, over the last years much attention has been paid to the unusual properties of quasi-one-dimensional materials, the most prominent among them being carbon nanotubes. Following their discovery in the early 1990s inorganic analogs, namely metal dichalcogenide nanotubes, were synthesized successfully[1,2] and are now available in considerable quantities.[3] Recently, the preparation of atomically thin MoS_2 sheets[4,5] has sparked wide interest. Originally an indirect band gap semiconductor, in the single-layer limit MoS_2 becomes a direct band gap material which makes it attractive for applications particularly in the field of nanoelectronic devices such as transistors.[6] Due to their strength, surface chemistry, nanosize, and high aspect ratio WS_2 nanotubes have a very beneficial effect in reinforcing polymer composites improving their tribological,[7] mechanical, and thermal properties.[8] Individual WS_2 nanotubes show promising results when used as photodetectors[9] and as catalysts in the hydrodesulfurization process.[10]

Metal dichalcogenide nanotubes exist only in multiwalled form where one shell corresponds to a triple layer S-*X*-S with metal *X* atoms sandwiched between two layers of sulfur atoms. The metal atoms are covalently bonded to six nearest sulfur atoms resulting in a trigonal prismatic structure. The triple layers are held together by weak van der Waals forces and, most commonly, stacked in 2H order, with the unit cell extending over two S-*X*-S layers. Bulk WS_2 has an indirect band gap of 1.3 eV; the smallest direct band gap is at the *K* point and governed by a pair of excitons A and B (1.98 eV and 2.41 eV, respectively, at room temperature).[11]

Raman spectroscopy is a widely used method to characterize the structure, symmetries, and optical properties of nanostructures. Both bulk 2H-WS_2 and WS_2 nanotubes have been analyzed by means of Raman spectroscopy in the past.[12–16] For bulk 2H-WS_2 the D_{6h}^4 ($P6_3/mmc$) symmetry results in four Raman active lattice vibrations at the Γ point of the hexagonal Brillouin zone: a fully symmetric A_{1g} mode (421 cm^{-1}),[12] two modes with E_{2g} symmetry (E_{2g}^1 at 356 cm^{-1}, E_{2g}^2 at 27 cm^{-1}), and an E_{1g} mode (306 cm^{-1}) that is inactive for light (exciting and scattered) propagation perpendicular to the basal plane.[17] In nanotubes, the A_{1g} mode becomes a breathing-like mode where the sulfur shells of one sandwich layer possess a significant radial component out of phase relative to the almost immobile tungsten shell. The E_{2g}^1 mode on the other hand shows longitudinal and circumferential displacement of sulfur shells in phase but out of phase with respect to the displacement of tungsten atoms.[18,19] Raman signatures of WS_2 nanotubes show distinct differences to the spectra of their bulk counterpart. The most characteristic Raman feature of WS_2 nanomaterials is the strongly increased Raman mode on the low-energy side of the A_{1g} mode at around 416 cm^{-1}. In the literature, following an analysis by Sourisseau *et al.*,[20] it is often attributed to a combination mode of acoustic phonons LA + TA from the *K* point of the Brillouin zone. An additional Raman feature that significantly broadens the shape of the E_{2g}^1 mode is assigned to the 2 × LA combination mode. However, these assignments are not confirmed by state of the art calculations of the phonon dispersion. Recent theoretical results[21] indeed seem to favor a different interpretation. In these density functional calculations, the infrared active conjugate of the E_{2g}^1 mode, the E_{1u} mode, accounts for the feature around 350 cm^{-1} whereas a silent B_{1u} mode is the origin of the feature at 416 cm^{-1}. For the remainder of this paper we will use this latter notation. As the B_{1u} mode is of only weak intensity in the Raman spectrum of the bulk material it is likely to be activated by the curvature and increased structural disorder inherent to the nanotubes.[16] In recent years several articles have been devoted to the evolution of this mode with diameter,[16] pressure,[22] and different layer orientation in thin films.[23]

This work addresses the B_{1u} mode as a unique feature of WS_2 nanomaterials subject to strong variations with curvature, excitation energy, and pressure. We present resonance Raman profiles of WS_2 nanotubes of different diameters using laser energies ranging from 1.85 eV to 2.71 eV. We find that the maximum of the Raman cross section is slightly redshifted

with respect to the excitonic transition energies in bulk WS_2 and that it decreases in energy with decreasing diameter of the nanotubes. The B_{1u}/A_{1g} intensity ratio is strongly dependent on the excitation energy, increasing by more than an order of magnitude from high to low excitation energies. This increase is not monotonic but shows a local minimum close to the excitonic transition energies. We attribute this to slightly different resonance conditions of the two Raman modes. In addition to resonance Raman spectroscopy we employed hydrostatic pressure-dependent measurements (up to 11 GPa) with a fixed excitation energy on agglomerated WS_2 nanotubes and derived the pressure coefficients of the Raman modes. Again, the B_{1u}/A_{1g} intensity ratio is subject to strong changes when varying the applied pressure. It reaches a maximum at around 6.5 GPa but decreases again towards the high-pressure region. These findings are explained in terms of a pressure-induced gradual increase in the excitonic transition energy that acts on the ratio $I(B_{1u})/I(A_{1g})$ in a manner similar to varying the excitation energies for a WS_2 nanotube at fixed ambient pressure.

II. EXPERIMENTAL

A. Synthesis, characterization

Inorganic nanotubes (INTs) of WS_2 were synthesized in a semi-industrial fluidized bed reactor by NanoMaterials, Ltd. A mixture of tungsten suboxides in the form of spherical nanoparticles was used as a precursor for this reaction. The reaction was carried out at temperatures of 800–900 °C in the atmosphere of hydrogen sulfide and hydrogen in the presence of the inert carrier gas nitrogen. First, long tungsten suboxide whiskers are *in situ* grown in the reactor, which is followed by an outside-inside sulfidization reaction. Careful control over the reaction parameters enables pure INT phase production. Nanotubes of 5–50 μm in length and 20–180 nm in diameter were obtained being partially entangled. A special procedure was developed in order to de-agglomerate these nanotubes through gentle and multitudinous sonication and filtration. Several droplets from a suspension of the de-agglomerated nanotubes in ethanol were dripped on scanning electron microscopy (SEM) stubs based on a silicon substrate and on carbon/collodion-coated Cu transmission electron microscopy (TEM) grids. Individual nanotubes were identified and surrounded by platinum circles with a focused ion beam (FIB) so that they were easily detectable under the optical microscope for Raman measurements. A Helios 900 Nanolab DualBeam Microscope (FIB) based on SEM was utilized for the Pt ring deposition. Organometallic $C_9H_{16}Pt$ precursor gas molecules were used. The resulting samples were examined by SEM with a Zeiss Ultra model V55 and LEO model Supra 55VP equipped with an EDS detector (Oxford model INCA). The nanotubes deposited on TEM grids were examined by TEM (Philips CM120) operating at 120 kV, equipped with an energy-dispersive x-ray spectroscopy (EDS) detector (EDAX-Phoenix Microanalyzer) for chemical analysis. A TEM image of an individual tube with outer and inner diameter of 32 and 8 nm, respectively, is presented in the inset of Fig. 1.

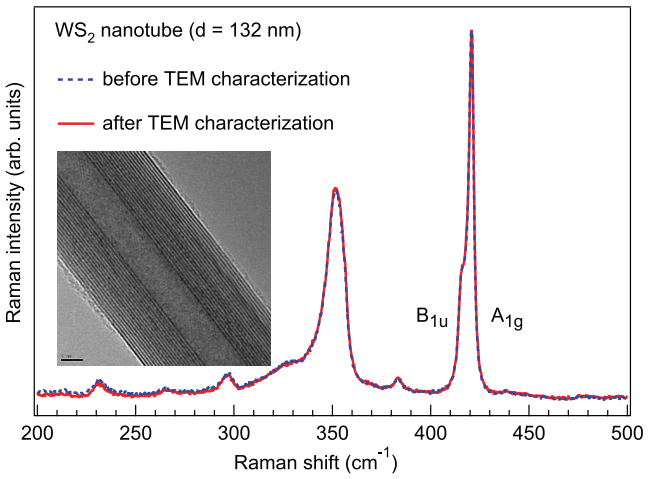

FIG. 1. (Color online) Raman spectra of an individual WS_2 nanotube ($d = 132$ nm) before and after characterization with TEM. None of the Raman features is altered by the characterization technique. The inset shows an exemplary TEM image of a different WS_2 nanotube with an outer diameter of 32 nm.

B. Resonance Raman spectroscopy

Resonance Raman profiles were taken of four individual WS_2 nanotubes on silicon substrate of 38, 46, 85, and 121 nm outer diameter as well as on WS_2 powder (average grain size: 2 μm) dispersed in ethanol. Nanotube diameters were determined by SEM with an accuracy better than 5%. An Ar^+Kr^+ laser (excitation energies: 1.834, 1.916, 2.182, 2.410, 2.607, 2.713 eV) was used as well as a dye laser with excitation energies ranging from 1.862 to 2.036 eV. Measurements were performed at room temperature in backscattering geometry and the scattered light was collected by a nitrogen-cooled charge-coupled device after being spectrally cleaned and dispersed by a triple monochromator (Dilor XY800). The laser power was reduced to values below 150 μW in the case of the nanotubes to avoid changes in the spectra induced by heating while accumulation times varied between 30 and 300 s. The Raman intensities were then normalized to both the laser power and integration time as well as to the system response by subsequently measuring the nonresonant Raman signal of CaF_2 for each excitation energy.

C. Hydrostatic pressure measurements

For the pressure measurements a small 30 × 30 μm^2 mat containing agglomerated WS_2 nanotubes was put into a gasketed diamond-anvil cell[24] and the line at 647 nm of an Ar^+Kr^+ laser was used for excitation. With a 4:1 methanol-ethanol mixture as pressure medium we obtained hydrostatic pressures up to 10.82 GPa as determined by the ruby-luminescence method.[25] The spectral resolution was about 1.5 cm^{-1}.

III. RESULTS

A. Raman measurements on SEM/TEM characterized nanotubes

Most Raman spectra that are discussed in this work were taken on WS_2 nanotubes on silicon substrate and characterized

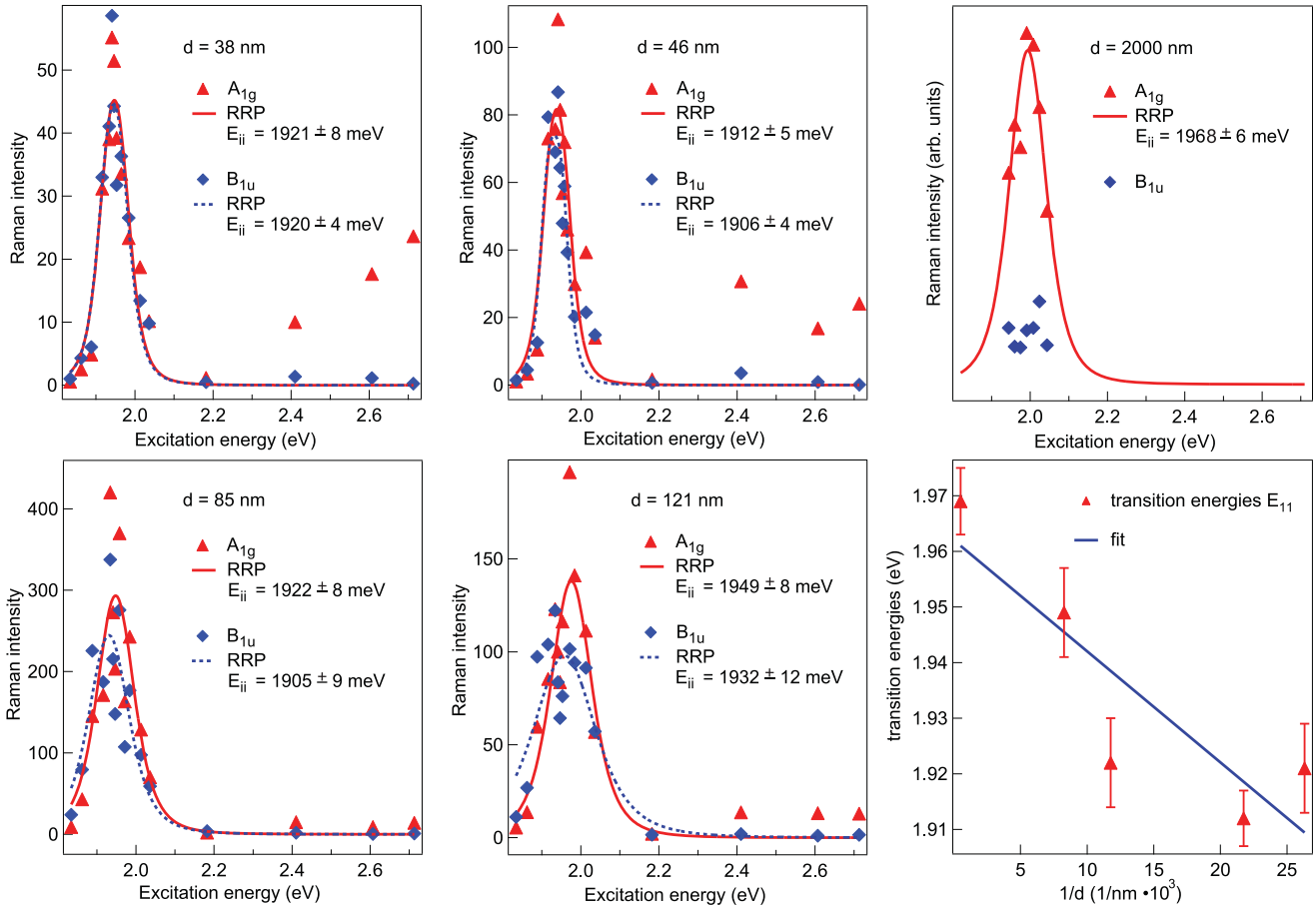

FIG. 2. (Color online) Resonance Raman profiles of different diameter WS_2 nanotubes (d = 38, 46, 85, and 121 nm) and of a WS_2 powder reference sample (upper right) for the A and B exciton region. Shown are the Raman intensities of the A_{1g} and B_{1u} modes (triangles and diamonds, respectively) normalized to the optical F_{2g} CaF_2 phonon as a function of the excitation energy and a fit to the data (solid and dashed lines) following Eq. (1). From the fits optical transition energies were derived; values are given in each plot. In the lower right, transition energies determined from the RRPs of the A_{1g} mode are plotted over the inverse diameter of the WS_2 nanotubes and the powder, demonstrating the redshift of the optical transition energy into the A exciton with decreasing size of the nanomaterials. The solid line is a linear fit.

by SEM. However, some nanotubes synthesized by the same method were also characterized by TEM and allow for a detailed insight in their internal structure. TEM images (inset in Fig. 1) show evenly spaced fringes of the (0002) plane corresponding to the c lattice constant of WS_2 of 6.2 Å. To examine whether the preparation technique affects the structure, Raman measurements were performed on samples before and after TEM characterization. While for SEM the accelaration voltage is very low (around 3 kV), the exposure to the high-voltage electron beam in TEM measurements is known to alter the structure of, e.g., InGaN quantum wells.[26] Figure 1 compares the Raman spectrum of a WS_2 nanotube (outer diameter d = 132 nm) before and after TEM electron beam exposure on the middle part of the nanotube. The spectra were normalized to the Raman intensity of the A_{1g} mode at 421 cm^{-1}. The position, relative intensities, and FWHMs of the Raman features remain the same; in particular no change can be seen in the the B_{1u}/A_{1g} intensity ratio. The structural disorder associated with the appearance of the B_{1u} mode is thus unaffected by sample preparation.

B. Resonance Raman spectroscopy

The resonance Raman profiles (RRPs) of individual WS_2 nanotubes of different diameters as well as of WS_2 powder (average grain size 2 μm) were measured in the range of 1.85 to 2.71 eV covering the region of both the A and B exciton (Fig. 2). The change in Raman signal with excitation energy was examined for the fundamental A_{1g} mode as well as for the B_{1u} mode appearing at 416 cm^{-1} on the low-energy side of the A_{1g} mode (421 cm^{-1}). A set of two Lorentzians was employed to fit the Raman spectra and to determine the intensity of the two Raman modes. The RRPs depicted in Fig. 2 exhibit well-defined maxima between 1.9 and 2.0 eV and a continuous rise in intensity between 2.4 and 2.7 eV. The position of the first maximum coincides with the absorption peak of the A exciton that is known to possess a binding energy of some 50 meV.[27] In all cases the maximum intensity of the B_{1u} mode can be found at slightly lower energies than that of the A_{1g} mode with the difference increasing with diameter. The second maximum in the A_{1g} mode intensity can be identified as originating from the B exciton (2.41 eV in bulk

TABLE I. Optical transition energies E_{11} of WS_2 nanotubes and a powder sample determined from fitting the measured RRPs of the A_{1g} and B_{1u} Raman modes with Eq. (1). For the powder only the RRP of the A_{1g} could be fitted.

Sample	A_{1g} E_{11} (eV)	B_{1u} E_{11} (eV)
WS_2 NT $d = 38$ nm	1.921 ± 0.008	1.920 ± 0.004
WS_2 NT $d = 46$ nm	1.912 ± 0.005	1.906 ± 0.004
WS_2 NT $d = 85$ nm	1.922 ± 0.008	1.905 ± 0.008
WS_2 NT $d = 121$ nm	1.949 ± 0.008	1.932 ± 0.012
WS_2 powder	1.968 ± 0.006	

WS_2[11]) while the B_{1u} intensity remains weak for this energy region.

The first optical transition energies (that is, the transition into the A exciton) were obtained by fitting the RRPs of the A_{1g} and B_{1u} mode with the equation for the excitation energy dependence of the Raman cross section[28]

$$I(E_{\mathrm{exc}}) = \left(\frac{\mathcal{M}c}{\hbar\omega_{\mathrm{ph}}}\right)^2 \left| \frac{1}{(E_{\mathrm{exc}} - E_{ii} - i\Gamma/2)} - \frac{1}{(E_{\mathrm{exc}} - \hbar\omega_{\mathrm{ph}} - E_{ii} - i\Gamma/2)} \right|^2. \quad (1)$$

Here, E_{exc} denotes the laser excitation energy, E_{ii} the optical transition energy, Γ the lifetime broadening of the intermediate electronic state, $\mathcal{M}$ contains the matrix elements, and c the remaining factors. The first and second term account for the incoming and outgoing resonance, respectively. The so derived first optical transition energies E_{11} for the four WS_2 nanotubes and the reference powder material are listed in Table I. They correspond to the incoming resonance and are thus lower lying in energy than the respective maximum in the Raman scattering cross section. For the powder the dependence of the B_{1u} mode intensity on the excitation energy was not sufficient to be fitted with Eq. (1).

As the A_{1g} mode is allowed by first-order Raman selection rules (in contrast to the B_{1u} mode) its RRP is taken to be the reliable source for obtaining the excitonic transition energies. For the nanotubes they all lie below the value found for the 2 μm powder WS_2 sample (bulk reference). Furthermore, the transition energies scale with the diameter of the nanotubes and with exception of the smallest diameter nanotube show increasing redshift with decreasing diameter. In a much smaller diameter region, a band gap reduction with decreasing diameter for inorganic nanotubes (in contrast to what one would expect from quantum confinement effects) has been predicted theoretically for GaS[29] and MoS_2 nanotubes[30] and was also experimentally confirmed by STS (scanning tunneling spectroscopy) measurements.[31] We report here for the first time the closely related dependence of the excitonic transition energies on diameter for diameters up to more than 120 nm. In the lower right panel of Fig. 2 the transition energies E_{11} are plotted as a function of the inverse diameter, and a linear fit is employed. As will be discussed in Sec. IV this dependence has its origin in the diameter-dependent curvature of the S-W-S triple layers.

C. Excitation energy dependence of the B_{1u}/A_{1g} Raman intensity ratio

The observation of the B_{1u} Raman mode at 416 cm^{-1} is one of the most intriguing features in WS_2 nanomaterials. Its intensity is negligible in the Raman spectra of WS_2 single crystals and its appearance thought to be related to disorder as group theory predicts it to be Raman inactive.[21] Up to now the change in the ratio $I(B_{1u})/I(A_{1g})$ with nanotube diameter,[16,32] pressure,[22] and thin-film orientation[23] has been studied and mostly attributed to curvature effects. These studies all use a fixed excitation energy (1.96 eV). From the RRPs measured in this work it is apparent that the relative enhancement of the B_{1u} and A_{1g} mode scale with diameter, and also their resonance maxima increasingly differ for increasing diameters. For the thinnest nanotube examined the relative enhancement of the two modes is near 1; for the nanotube with $d = 121$ nm it is around 0.7. The existence of a diameter dependence of the $I(B_{1u})/I(A_{1g})$ ratio observed in Ref. 16 can thus be confirmed. However, using only one excitation energy does not account for the difference in excitonic transition energies for nanotubes of different diameter and the energetic offset of the two RRPs.

Figure 3(a) shows Raman spectra of a WS_2 nanotube, 121 nm in diameter, measured with different excitation energies. The spectrum obtained at 1.953 eV (middle trace) features a B_{1u} mode as a shoulder of the neighboring A_{1g} mode, very similar to Raman spectra of WS_2 nanotubes found in the literature.[16,22] Far from resonance, in the Raman spectrum taken with a 2.713 eV (lower trace) excitation energy the absolute intensity of the Raman features is greatly reduced but also the B_{1u}/A_{1g} intensity ratio has changed drastically; only a fit to the specified region reveals the B_{1u} mode is still present. The first-order E^1_{2g} (356 cm^{-1}) and A_{1g} modes dominate the Raman spectrum for the high excitation energies. Exciting on the lower energy side of E_{11}, an excitation energy of 1.862 eV (upper trace) results in a Raman spectrum where the B_{1u} and the E_{1u} Raman mode at 352 cm^{-1} are even more pronounced than the first-order allowed Raman features of WS_2.

The drastic influence of the excitation energy on the relative intensities of the two modes in the four nanotubes investigated here is seen in Fig. 3(b) exemplary for the thickest nanotube and with similar results for the other nanotubes (not shown). For each excitation energy the areas of the two Lorentzian fits were compared. For the high excitation energy region, the intensity ratio B_{1u}/A_{1g} is less than 0.2 but it increases by an order of magnitude towards low excitation energies. Around the first optical transition energy region (1.949 eV) a local minimum is observed. There are two main contributions to the measured dependence of the relative intensities of the two Raman modes with excitation energy: (1) For the A excitonic resonance region both Raman modes are resonantly enhanced, but as mentioned above the resonance condition of the B_{1u} mode is met at slightly lower energies than that of the A_{1g} mode. Both the increase in the intensity ratio for the low excitation energies and the local minimum around the A exciton energy are a consequence of this phenomenon. This is illustrated in the inset of Fig. 3(b). The ratio of two simulated, identical resonance Raman profiles similar to the ones obtained from the measured spectra with a full width at half maximum of around 8 meV and an energetic offset of 10 meV is shown that mimics the measured nonmonotonic

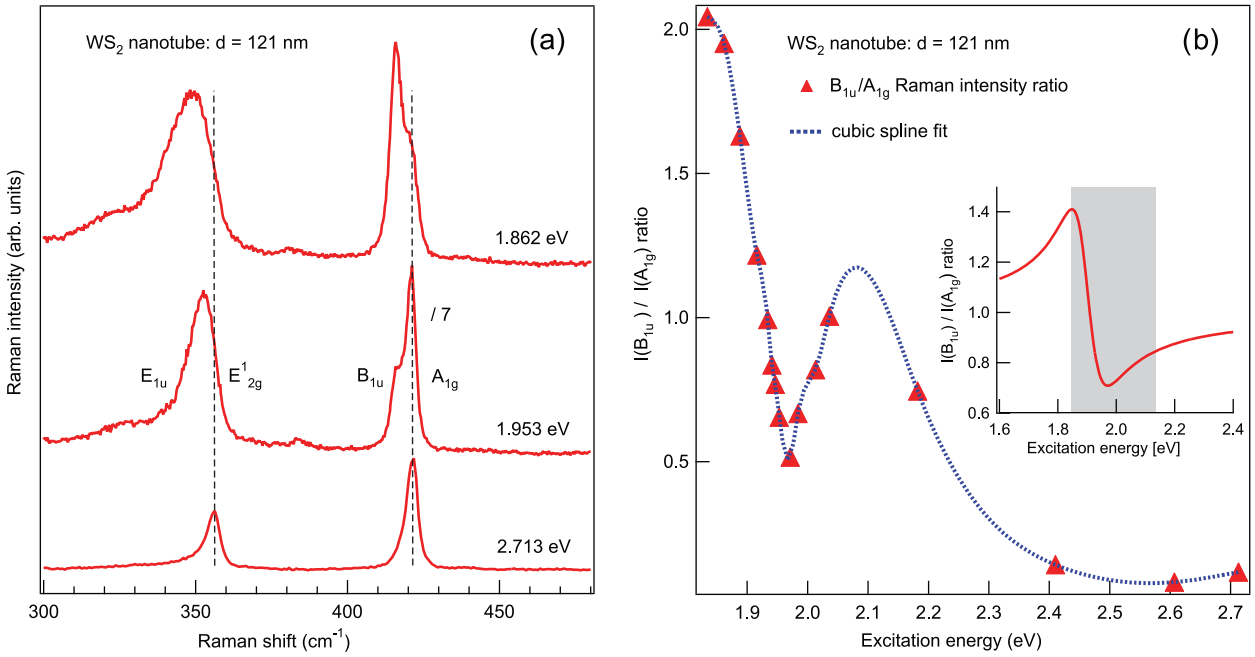

FIG. 3. (Color online) (a) Raman spectra of a WS_2 nanotube ($d = 121$ nm). The spectrum excited with 1.953 eV, close to the resonance condition of the A_{1g} mode, is divided by a factor of 7 to be of similar intensity compared to the two other spectra. The symmetry of the four main Raman modes is given next to the corresponding spectral features. The dashed lines denote the two first-order allowed Raman modes. The B_{1u} and E_{1u} modes that are barely present in the bottom spectrum (2.713 eV) become increasingly prominent when the nanotube is excited with lower energies. (b) The B_{1u}/A_{1g} Raman intensity ratio with excitation energy for the same nanotube. A strong increase can be observed with decreasing excitation energy, with a kink in the A excitonic resonance region. The inset in (b) shows that the observed dependence between 1.85 and 2.1 eV (shaded area) is a result of dividing a simulated resonance profile by another with a small energy offset (10 meV). In the measured spectra, because only the A_{1g} phonon exhibits resonant behavior in the B exciton region, the intensity ratio approaches small values above 2.1 eV.

changes in the intensity ratio (shaded area). (2) Only the A_{1g} mode intensity is enhanced in the region of the B exciton energy, while the B_{1u} phonon does not couple strongly to this second optical transition. Therefore, instead of approaching the value of one as suggested by the simple model in the inset, the intensity ratio approaches zero for the 2.4–2.7 eV range.

D. Pressure dependence of the WS_2 nanotube Raman response

Figure 4(a) shows Raman spectra of agglomerated WS_2 nanotubes measured at hydrostatic pressures up to 10.82 GPa with a fixed excitation energy of 1.916 eV. Additionally, some spectra were obtained upon pressure release and depicted as well. With increasing pressure the position of all Raman modes shifts to higher energies, the line shapes become distorted, and there are also significant changes in the B_{1u}/A_{1g} intensity ratio. The impact of hydrostatic pressure on the Raman spectra of the WS_2 nanotubes is completely reversible.

The pressure dependence of the A_{1g} and B_{1u} mode frequencies starting at 420 and 415.5 cm^{-1} for ambient pressure is shown in Fig. 4(b) and used to derive pressure coefficients $\delta\omega/\delta P$. While for the A_{1g} mode a Lorentzian line shape suffices the B_{1u} region is best fitted with a Fano line shape to account for the increasingly asymmetric line shape with pressure. A linear upshift of 3.19 ± 0.05 cm^{-1}/GPa and 1.41 ± 0.04 cm^{-1}/GPa for the A_{1g} and B_{1u} mode, respectively, is found.

Similar to the excitation-energy-dependent Raman measurements the most striking effect in the spectra is the drastic change of the relative intensity of the B_{1u} and the A_{1g} mode with pressure [see Fig. 4(c)]. Starting off with comparatively low values for the ambient pressure Raman measurement [$I(B_{1u})/I(A_{1g}) = 0.85$] the relative B_{1u} Raman mode intensity quickly rises almost linearly until a maximum is reached for hydrostatic pressures around 6.5 GPa. Above this threshold the intensity ratio decreases again in the 7–11 GPa region and levels out at about 2.5.

IV. DISCUSSION

In this section we first discuss the measured resonance Raman profiles of different-diameter tungsten disulfide nanotubes and the resulting transition energy E_{11} dependence on nanotube diameter. Next, the difference in the resonance condition of the A_{1g} mode and the silent B_{1u} mode and the resulting strong variations in the B_{1u}/A_{1g} ratio with excitation energy are analyzed. Finally, Raman measurements on agglomerated WS_2 nanotubes under hydrostatic pressure are addressed, again with a focus on the change in the $I(B_{1u})/I(A_{1g})$ ratio with pressure.

Resonance Raman profiles reflect the change in normalized Raman intensity of a specific Raman mode with the laser excitation energy. Following Eq. (1) whenever the energy of the incoming or the scattered light coincides with a real

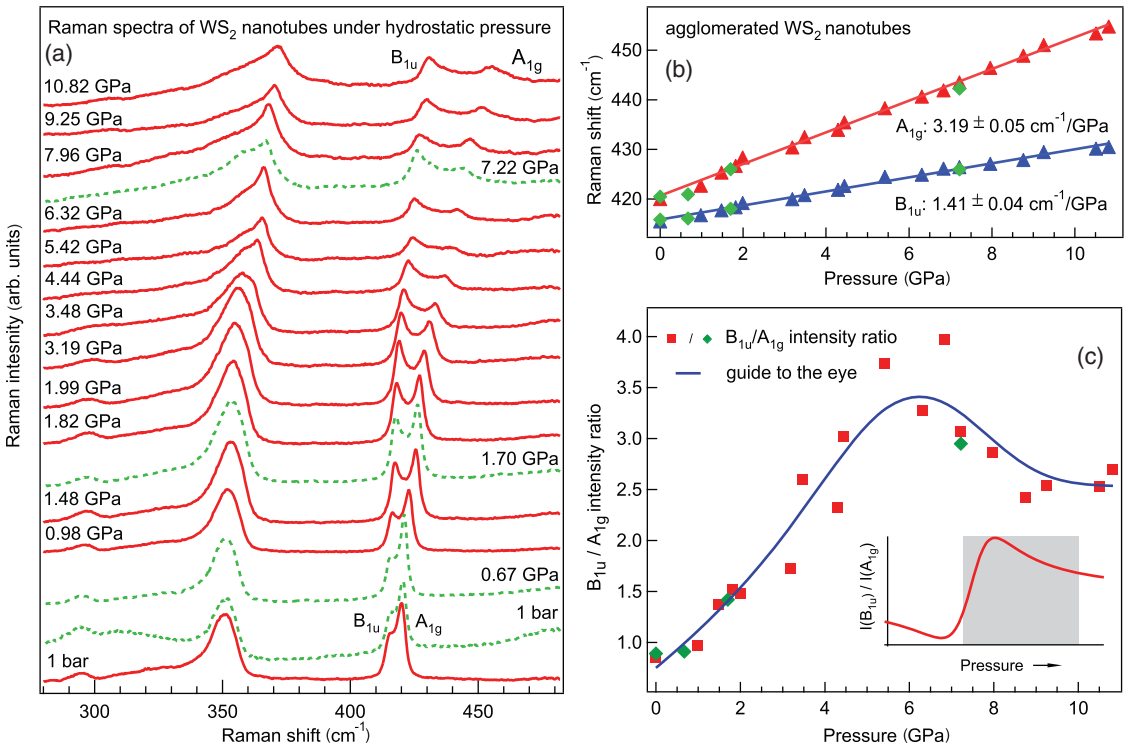

FIG. 4. (Color online) (a) Raman spectra of agglomerated WS_2 nanotubes (excitation energy: 1.916 eV) under hydrostatic pressure up to 10.82 GPa (solid lines). The spectra obtained during subsequent pressure release are also depicted (dashed lines). All Raman modes shift up and broaden with increasing pressure. Additionally, the B_{1u}/A_{1g} intensity ratio changes strongly. (b) The upshift of both the A_{1g} and B_{1u} mode with pressure is linear; the pressure coefficients are given. (c) While for pressures up to 6 GPa the B_{1u}/A_{1g} intensity ratio rises almost linearly, for the high-pressure region a decrease is observed. A smoothing spline fit is employed to guide the eye. In (b) and (c) the diamonds are values obtained during pressure release that illustrate the reversibility of the process. The inset in (c) in analogy to the inset in Fig. 3(b) (the x axis is reversed) demonstrates that with increasing pressure the ratio of two resonance profiles (shaded area) with a small energy offset reproduces well the experimental observation (see Sec. IV).

electronic transition the Raman scattering cross section is greatly enhanced. Taking into account that both processes contribute to the intensity enhancement and it is the incoming resonance that corresponds to the optical transition energy one can follow the band structure of the material under investigation. In WS_2, as can be seen in absorption measurements[11,27] around the direct band gap there is a pair of excitons, termed A and B, that are split by spin orbit and interlayer interaction.[33] Reported values for the A and the B peak position in a WS_2 single crystal are 1.98 eV and 2.41 eV, respectively.[11] The relatively sharp (FWHMs of around 70 to 180 meV) RRPs of the measured WS_2 nanotubes in the 1.8–2.1 eV region thus correspond to the optical transition into the A exciton. There are not enough data to quantitatively determine the transition energy into the B exciton from a resonance profile at higher energies, but an intensity enhancement between 2.4 and 2.7 eV for the A_{1g} mode is observed. To begin with, the RRP of the fundamental first order A_{1g} mode is taken to accurately mirror the excitonic transition energy E_{11} of the nanotubes and the WS_2 powder. With respect to the powder sample the excitonic transition energies in the nanotubes are shifted to lower energies with an increasing redshift for decreasing diameter. Our findings are in qualitative accordance with previously published theoretical work on WS_2 nanotubes.[30] In a smaller diameter region Scheffer and coworkers[31] took dI/dV curves of individual WS_2 nanotubes using STS, and in spite of significantly scattered data they could derive a redshift with decreasing diameter of the nanotube. Frey *et al.*[34] employed absorption spectroscopy to determine the A and B exciton peak positions of films of inorganic fullerene-like (IF) MoS_2 and WS_2. Their results suggest that a redshift in the A exciton peak is only observed if the number of triple layers is larger than around $n = 6$. For lower number of layers quantum confinement can be seen as a competing process that ultimately leads to a blueshift of the excitons. For the nanotubes examined in this work the inner radii and the related number of layers are not exactly known. However, from comparison with similar diameter nanotubes characterized with TEM during the course of this work, n is expected to be much bigger than 6 (in the case of the nanotube depicted in Fig. 1 it is 18, for example). As can be seen in Fig. 2, the normalized Raman intensities, which are related to the sample volume probed by the laser, and hence to the number of walls, increase with diameter.

The underlying mechanism for the excitonic transition energy dependence on the diameter of the nanotubes can be found in different magnitudes of strain incorporated in the tube walls. Obviously, rolling up triple layers in inorganic nanotubes involves much higher strain energies than in carbon nanotubes (CNTs), where there is only one carbon layer. The strain energy per atom scales with the radius of the nanotubes as

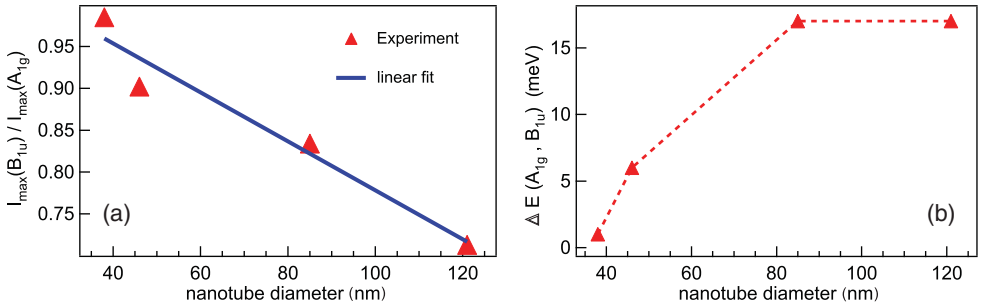

FIG. 5. (Color online) (a) A roughly linear decrease in the intensity ratio $I_{max}(B_{1u})/I_{max}(A_{1g})$ is observed when going from smaller to larger nanotube diameters. (b) The maxima of the resonance Raman profiles of the B_{1u} and A_{1g} mode increasingly differ in energy as the nanotube diameter becomes larger.

$E_{str} = \alpha/R^2$, and values for α, the strain parameter, are 2.2 and 27.2 eVÅ^2 per atom for CNTs and MoS_2-NTs, respectively.[35] Considering one S-W-S triple layer, in a WS_2 nanotube the inner (outer) sulfur layer will have a smaller (bigger) diameter with respect to the metal layer in the middle. This is accompanied by uniaxial compressive and tensile strain in the inner and outer part of one triple layer, respectively, whose magnitude again depends strongly on the curvature of the layers and hence on the diameter of the tube wall as a whole. The influence of strain on the electronic band structure has been investigated theoretically for a variety of closely related compounds such as GaS nanotubes, single-walled $MoTe_2$ nanotubes, and few-layer MoS_2.[29,36,37] In all cases the band gap is found to be lower than the bulk limit and to decrease with decreasing diameter and increasing strain, respectively. For excitons in particular similar results were obtained for strained CdS nanowires.[38] It is argued in Refs. 30 and 37 that the main reason for the band gap shrinking lies in the tensile strain that brings down the conduction band's antibonding Mo-d-S-p states near the K point. For small compressive strain the opposite effect is seen but to a somewhat lesser extent. As the lowest direct band gap also in WS_2 is near the K point (as are the excitons) these results serve as an explanation for the experimentally observed optical transition energy decrease with decreasing diameter of the WS_2 nanotubes investigated in this work.

In this paper the A_{1g} mode at 421 cm^{-1} was used to determine optical transition energies via resonance Raman spectroscopy, because it is the only Raman feature of WS_2 materials in the measured region that is (a) allowed in first-order Raman scattering and (b) shows no substantial overlap with any other Raman feature (as is the case for the E^1_{2g} mode). The B_{1u} mode on the other hand is originally a silent mode, and its appearance is a distinctive feature of WS_2 nanomaterials. Again, what distinguishes the WS_2 nanotubes from the 2D layered bulk material is the local curvature of the nanotube walls. If one considers two adjacent walls within the same nanotube the outer wall will comprise a larger number of unit cells and a slight lattice mismatch is very likely to occur. Additionally, TEM characterization of WS_2 nanotubes in agreement with measurement done in the course of this work often reveal that the center of the hollow inner part does not coincide with the geometrical axis of the nanotubes outer walls[39] pointing to a rearrangement of layers and edge dislocations close to the center of the tubes. It is not clear yet whether WS_2 nanotubes are formed by continuous spiral winding (Ref. 39) of one S-W-S layer or whether they consist of concentric cylindrical shells (Ref. 40). Also, whether or not the different nanotube walls all possess the same chirality (or are achiral) is still under debate. Recent results suggest that the majority of shells are either zigzag or near zigzag, e.g., mostly of zero chiral angle.[40,41] Obeying the stacking order of the bulk flat slab will thus be very difficult in the curved nanostructures and formally silent modes like the B_{1u} mode will be activated as a result of the loss of long-range order. Moreover, from the point of view of symmetry the opposite strain direction in the inner and the outer sulfur layer lifts the inversion symmetry of the triple stacks and hence the strict Raman selection rules valid for WS_2 crystals. Obviously these effects become more pronounced as the diameter of the nanotubes is reduced whereas the walls in comparatively thick nanotubes will little by little adapt the ordered, unstrained structure of the single crystal. This leads to a gradual suppression of the B_{1u} mode intensity with increasing tube diameter.

In Fig. 5(a) the maximum intensities of the resonance Raman profiles (see Fig. 2) are plotted as $I_{max}(B_{1u})/I_{max}(A_{1g})$ as a function of the diameter. The diameter dependence so derived differs from the one obtained in Ref. 16 as it compares the absolute Raman intensities of the two modes at different excitation energies (the energies where the maximum resonant enhancement is reached). For the thinnest, 38 nm diameter nanotube, these energies are almost identical (Fig. 2). As can be seen in Fig. 5(b) they increasingly differ as the diameter becomes larger. In all cases, the maximum Raman intensity of the B_{1u} mode lies on the low-energy side of the maximum Raman intensity of the A_{1g} mode. This is possibly because the Raman signal of the B_{1u} mode mainly stems from the inner triple layers, where the curvature of the nanotube walls is high enough for the Raman selection rules to be relaxed. As a consequence the values for E_{11} obtained from the B_{1u} mode are that of a nanotube of seemingly smaller diameter and hence of smaller excitonic resonance energy. This effect is negligible for small-diameter nanotubes but becomes increasingly important as the diameter and the number of walls increases.

In the Raman spectra of agglomerated WS_2 nanotubes under hydrostatic pressure at a fixed excitation energy (1.916 eV) one can observe the frequencies of the A_{1g} and B_{1u} Raman modes linearly upshifting with pressure. For the closely related compound MoS_2 a simple central force model was able to explain the data as resulting from an increase of the intralayer and interlayer force constants.[42] It was found

that the interlayer distance (van der Waals gap) decreased by almost 8% from atmospheric to 5 GPa pressure and that the associated change of the interlayer force constant is the main reason for the frequency upshift of vibrational modes. The difference in the pressure-induced slope can be explained by the normal coordinates of the both crystal modes. The A_{1g} mode represents an in-phase, the B_{1u} mode an out-of-phase S-S stretching motion.[43] Hence the former one has to overcome a much larger force than the latter, which leads to a distinctly higher pressure coefficient.

The linear pressure-induced frequency upshifts of Raman modes rule out the possibility of a phase transition. Significant alterations in the cross section of the nanotubes or rearrangement of atoms from a crystallographic point of view would be indicated by a sudden change of pressure coefficients. In single-walled carbon nanotube bundles, for instance, a sudden change in the slope of the frequency upshift of the *G* modes with pressure has been attributed to a circular-elliptical phase transition.[44] The observation that the Raman spectra return to their original appearance upon pressure release [Fig. 4(a)] is further evidence of the agglomerated WS_2 nanotubes not collapsing in the applied pressure range. Instead it is indication of the extreme flexibility of the material. Any macroscopic defects as a result of the application of pressure are therefore unlikely.

Thus, the question remains as to why the relative intensity of the B_{1u} mode—being related to disorder—undergoes such strong changes with increasing pressure [Fig. 4(c)]. Yu *et al.*[22] followed the evolution of the B_{1u}/A_{1g} mode intensity ratio under pressure for W/WS_2 fullerene-like nanospheres with core-shell structure. The results are to a large extent comparable to the ones obtained in this work. In the low-pressure region the $I(B_{1u})/I(A_{1g})$ ratio increases but decreases again after going through a maximum around 6 GPa. Their interpretation makes use of the concept of shape transitions and associated changes in curvature of the nanotubes.

In light of the results from the resonance Raman measurements presented in this work a different explanation is given here. We argue that the main effect of the hydrostatic pressure applied lies in a gradual upshift of the A excitonic transition energy.[45,46] With that, the coupling of the incoming photon to the optical transition changes with pressure. As there is a small energy offset in the resonant enhancement of the two Raman modes (see Sec. III B) the relative intensities will also vary. The excitation energy used here (1.916 eV) is situated on the low-energy side of the A exciton peak for ambient pressures and will move further downwards when the pressure is increased. According to Refs. 47 and 48 the value for the energy dependence of the A exciton peak on pressure in WS_2 is 45 meV/GPa which means that already at 6 GPa pressure the A exciton should be found above 2.2 eV and the laser excitation is near off-resonance. Additionally, with pressure, the exciton will gradually become unstable and eventually dissociate in the higher pressure region (above 6 GPa in MoS_2[46]). This accelerates the process of putting the excitation energy off-resonance with increasing pressure. The evolvement of the B_{1u}/A_{1g} intensity ratio with pressure depicted in Fig. 4(c) can therefore be seen as a result of scanning through the relative intensities of the low-energy side of two resonance Raman profiles that have maxima at slightly different energies and that both move upwards in energy with increasing pressure. In analogy to the inset in Fig. 3(b) this is shown in the inset of Fig. 4(c) where the ratio of two exemplary RRPs demonstrates the effect.

V. CONCLUSION

Based on resonant Raman spectroscopy we find that the first optical transition energy E_{11} into the A exciton in WS_2 nanotubes is shown to be lower than the bulk value and to become smaller with decreasing nanotube diameter. The origin of this phenomenon is found in the downshift of the conduction band states caused by the bending of the S-W-S triple layers with respect to the flat parent material. Resonance Raman profiles reveal a strong enhancement of the A_{1g} and B_{1u} Raman mode intensities mainly in the A exciton region. For the thinner nanotubes the enhancement is of similar strength for both Raman modes; for thicker nanotubes a smaller maximum enhancement of the B_{1u} with respect to the maximum enhancement of the A_{1g} mode is observed. The B_{1u} mode is a silent mode in the bulk material; its activation in the nanomaterials is a result of a relaxation of Raman selection rules due to the gradual increase in strain and curvature of the triple layers with decreasing nanotube diameter. In the limit of a reference powder material with grain sizes in the μm regime we find that only the A_{1g} mode shows significant resonant behavior. The resonance Raman profiles of the two modes possess a small energy offset that is also diameter dependent and leads to strong variations of the $I(B_{1u})/I(A_{1g})$ ratio with excitation energy.

Under hydrostatic pressure the Raman modes of WS_2 nanotubes are linearly upshifted with pressure coefficients of $\delta\omega_{A_{1g}}/\delta P = 3.19 \pm 0.05\ \mathrm{cm}^{-1}/\mathrm{GPa}$ and $\delta\omega_{B_{1u}}/\delta P = 1.41 \pm 0.04\ \mathrm{cm}^{-1}/\mathrm{GPa}$. Once again it is the $I(B_{1u})/I(A_{1g})$ ratio in the Raman spectra that is influenced most by the applied pressure. Our results support the interpretation that the variations in the relative intensities stem from a gradual upshift and an eventual disappearance of the A exciton peak. In summary, we are able to consistently explain the unusual behavior of the $I(B_{1u})/I(A_{1g})$ ratio in WS_2 nanotubes for different diameters, excitation energies, and hydrostatic pressure.

ACKNOWLEDGMENT

We are grateful to the G.M.H Schmidt Minerva Center for Supramolecular Chemistry of the Weizmann Institute.

*mstaiger@physik.tu-berlin.de

[1] R. Tenne, L. Margulis, M. Genut, and G. Hodes, Nature (London) **360**, 444 (1992).

[2] M. Remškar, Z. Škraba, F. Cléton, R. Sanjinés, and F. Lévy, Appl. Phys. Lett. **69**, 351 (1996).

[3] A. Zak, L. Sallacan-Ecker, A. Margolin, M. Genut, and R. Tenne, NANO **4**, 91 (2009).

[4] K. Novoselov, D. Jiang, F. Schedin, T. Booth, V. Khotkevich, S. Morozov, and A. Geim, Proc. Natl. Acad. Sci. USA **102**, 10451 (2005).

[5]H. Matte, A. Gomathi, A. Manna, D. Late, R. Datta, S. Pati, and C. Rao, Angew. Chem. Int. Ed. **122**, 4153 (2010).
[6]B. Radisavljevic, A. Radenovic, J. Brivio, V. Giacometti, and A. Kis, Nat. Nanotechnol. **6**, 147 (2011).
[7]E. Zohar, S. Baruch, M. Shneider, H. Dodiuk, S. Kenig, D. Wagner, A. Zak, A. Moshkovith, L. Rapoport, and R. Tenne, Sensors Transducers **12**, 53 (2011).
[8]C. Reddy, A. Zak, and E. Zussman, J. Mater. Chem. **21**, 16086 (2011).
[9]C. Zhang, S. Wang, L. Yang, Y. Liu, T. Xu, Z. Ning, A. Zak, Z. Zhang, R. Tenne, and Q. Chen, Appl. Phys. Lett. **100**, 243101 (2012).
[10]Y. Tsverin, R. Popovitz-Biro, Y. Feldman, R. Tenne, M. R. Komarneni, Z. Yu, A. Chakradhar, A. Sand, and U. Burghaus, Mater. Res. Bull. **47**, 1653 (2012).
[11]F. L. C. Ballif and M. Regula, Sol. Energ. Mat. Sol. **57**, 189 (1999).
[12]C. Sourisseau, M. Fouassier, M. Alba, A. Ghorayeb, and O. Gorochov, Mater. Sci. Eng., B **3**, 119 (1989).
[13]P. M. Rafailov, C. Thomsen, K. Gartsman, I. Kaplan-Ashiri, and R. Tenne, Phys. Rev. B **72**, 205436 (2005).
[14]K. Gartsman, I. Kaplan-Ashiri, R. Tenne, P. Rafailov, and C. Thomsen, AIP Conf. Proc. **786**, 349 (2005).
[15]M. Virśek, A. Jesih, I. Milošević, M. Damnjanović, and M. Remškar, Surf. Sci. **601**, 2868 (2007).
[16]M. Krause, M. Virśek, M. Remškar, N. Salacan, N. Fleischer, L. Chen, P. Hatto, A. Kolitsch, and W. Möller, ChemPhysChem **10**, 2221 (2009).
[17]T. Sekine, T. Nakashizu, K. Toyoda, K. Uchinokura, and E. Matsuura, Solid State Commun. **35**, 371 (1980).
[18]E. Dobardžić, B. Dakić, M. Damnjanović, and I. Milošević, Phys. Rev. B **71**, 121405(R) (2005).
[19]E. Dobardžić, I. Milošević, B. Dakić, and M. Damnjanović, Phys. Rev. B **74**, 033403 (2006).
[20]C. Sourisseau, F. Cruege, M. Fouassier, and M. Alba, Chem. Phys. **150**, 281 (1991).
[21]A. Molina-Sánchez and L. Wirtz, Phys. Rev. B **84**, 155413 (2011).
[22]S. Yu, L. Chang, H. Yang, B. Liu, Y. Hou, L. Wang, M. Yao, T. Cui, and G. Zou, J. Phys.: Condens. Matter **19**, 425228 (2007).
[23]J. Chung, Z. Dai, K. Adib, and F. Ohuchi, Thin Solid Films **335**, 106 (1998).
[24]G. Huber, K. Syassen, and W. B. Holzapfel, Phys. Rev. B **15**, 5123 (1977).
[25]G. Piermarini, S. Block, J. Barnett, and R. Forman, J. Appl. Phys. **46**, 2774 (1975).
[26]T. Smeeton, M. Kappers, J. Barnard, M. Vickers, and C. J. Humphreys, Appl. Phys. Lett. **83**, 5419 (2003).
[27]J. Wilson and A. Yoffe, Adv. Phys. **18**, 193 (1969).
[28]M. Cardona, *Light Scattering in Solids II*, Topics in Applied Physics, Vol. 50 (Springer, 1982).
[29]T. Kohler, T. Frauenheim, Z. Hajnal, and G. Seifert, Phys. Rev. B **69**, 193403 (2004).
[30]G. Seifert, AIP Conf. Proc. **544**, 415 (2000).
[31]L. Scheffer, R. Rosentzveig, A. Margolin, R. Popovitz-Biro, G. Seifert, S. Cohen, and R. Tenne, PhysChemChemPhys **4**, 2095 (2002).
[32]M. Krause, M. Virśek, M. Remškar, A. Kolitsch, and W. Möller, Phys. Status Solidi B **246**, 2786 (2009).
[33]R. Coehoorn, C. Haas, and R. A. de Groot, Phys. Rev. B **35**, 6203 (1987).
[34]G. L. Frey, S. Elani, M. Homyonfer, Y. Feldman, and R. Tenne, Phys. Rev. B **57**, 6666 (1998).
[35]G. Radovsky, R. Popovitz-Biro, M. Staiger, K. Gartsman, C. Thomsen, T. Lorenz, G. Seifert, and R. Tenne, Angew. Chem. Int. Ed. **50**, 12316 (2011).
[36]X. Wu, Z. Xu, and X. Zeng, Nano Lett. **7**, 2987 (2007).
[37]E. Scalise, M. Houssa, G. Pourtois, V. Afanas'ev, and A. Stesmans, Nano Res. **5**, 43 (2012).
[38]Q. Fu, Z. Zhang, L. Kou, P. Wu, X. Han, X. Zhu, J. Gao, J. Xu, Q. Zhao, W. Guo, and D. Yu, Nano Res. **4**, 308 (2011).
[39]M. Remškar, Z. Škraba, M. Regula, C. Ballif, R. Sanjinés, and F. Lévy, Adv. Mater. **10**, 246 (1998).
[40]M. B. Sadan, M. Heidelmann, L. Houben, and R. Tenne, Appl. Phys. A **96**, 343 (2009).
[41]M. Krause, A. Mücklich, A. Zak, G. Seifert, and S. Gemming, Phys. Status Solidi B **248**, 2716 (2011).
[42]A. Bagnall, W. Liang, E. Marseglia, and B. Welber, Physica B&C **99**, 343 (1980).
[43]T. Wieting and J. Verble, Phys. Rev. B **3**, 4286 (1971).
[44]M. J. Peters, L. E. McNeil, J. P. Lu, and D. Kahn, Phys. Rev. B **61**, 5939 (2000).
[45]G. Connell, J. Wilson, and A. Yoffe, J. Phys. Chem. Solids **30**, 287 (1969).
[46]T. Livneh and E. Sterer, Phys. Rev. B **81**, 195209 (2010).
[47]A. Brothers and J. Brungardt, Phys. Stat. Sol. B **91**, 675 (1979).
[48]This value is for the 3R polytype of WS_2. For the 2H polytype that is found in most nanotubes the value is expected to be larger.

B.2. Physical Review B 91, 195419 (2015)

PHYSICAL REVIEW B **91**, 195419 (2015)

Splitting of monolayer out-of-plane A_1' Raman mode in few-layer WS_2

Matthias Staiger,[1,*] Roland Gillen,[1] Nils Scheuschner,[1] Oliver Ochedowski,[2] Felix Kampmann,[1] Marika Schleberger,[2] Christian Thomsen,[1] and Janina Maultzsch[1]

[1]*Institut für Festkörperphysik, Technische Universität Berlin, Eugene-Wigner-Building EW 5-4, Hardenbergstrasse 36, 10623 Berlin, Germany*

[2]*Fakultät für Physik and Cenide, Universität Duisburg-Essen, Lotharstrasse 1, 47057 Duisburg, Germany*

(Received 19 December 2014; revised manuscript received 31 March 2015; published 15 May 2015)

We present Raman measurements of mono- and few-layer WS_2. We study the monolayer A_1' mode around 420 cm^{-1} and its evolution with the number of layers. We show that with increasing layer number there are an increasing number of possible vibrational patterns for the out-of-plane Raman mode: in N-layer WS_2 there are N Γ-point phonons evolving from the A_1' monolayer mode. For an excitation energy close to resonance with the A excitonic transition energy, we were able to observe all of these N components, irrespective of their Raman activity. Density functional theory calculations support the experimental findings and make it possible to attribute the modes to their respective symmetries. The findings described here are of general importance for all other phonon modes in WS_2 and other layered transition-metal dichalcogenide systems in the few-layer regime.

DOI: 10.1103/PhysRevB.91.195419 PACS number(s): 78.30.−j, 78.67.−n, 63.22.Np, 71.35.Gg

I. INTRODUCTION

The last few years have seen a spectacular increase in interest in layered transition-metal dichalcogenides (TMDs). While the properties of the three-dimensional (3D) bulk materials have been well known for decades, the possibility of thinning them down towards the monolayer has given rise to an entirely new research area. Their structural formula MX_2 (with M being a transition metal and X being a chalcogenide) comprises metals, semimetals, semiconductors, and superconductors [1]. What they have in common is that, with approaching the two-dimensional (2D) limit, a whole world of intriguing properties such as extraordinarily large exciton binding energies [2], robust valley polarization [3], and large spin orbit splitting [4] opens up. These properties pave the way for potential use of TMDs for applications in digital electronics and optoelectronics [5], in energy conversion and storage [6], and in spintronics [7]. Most tungsten- and molybdenum-based TMDs exhibit a transition from an indirect to a direct band-gap semiconductor when being thinned down to the monolayer, resulting in high-intensity photoluminescence [8–10].

Raman spectroscopy is one of the most powerful tools in characterizing nanomaterials. For few-layer (FL) TMDs such as FL-WS_2 it allows us, for instance, to exactly determine the number of layers. To be able to extract all the information that the measured Raman spectra have to offer, it is of primary importance to have common ground on which to categorize the different Raman modes as a function of the number of layers. There is a large number of publications on monolayer TMDs [11–14] and the respective bulk materials [12,15,16], but only a few papers concentrate on the transition from monolayer to bulk, e.g., the evolvement of the Raman signatures with the number of layers. In these papers, moreover, many use the symmetry of the bulk to assign the Raman features [10,17–19]; only recently have there been some reports that take into account the different symmetries of TMDs with an even number of layers (even N) and an odd number of layers (odd N) [20,21]. However, these studies focus only on Raman modes that are allowed in first-order scattering.

In this work we will show that (i) it is important to distinguish between an even and odd number of layers and (ii) when the excitation energy is in resonance with the first optical transition of the investigated material, it is necessary to consider the full set of phonons. We study the splitting of the monolayer out-of-plane A_1' mode in FL-WS_2 in particular and are able to observe layer-dependent Raman signatures comprising Raman-active and -inactive modes. They allow for easy identification of the number of layers via Raman spectroscopy. Moreover a general systematic behavior for the splitting of the monolayer Raman modes is proven experimentally and is supported by density functional theory (DFT) calculations. The findings described in this work should be expandable to other FL-TMDs.

II. EXPERIMENT

The samples were prepared from a bulk WS_2 crystal (hq graphene, Groningen, Netherlands) using the mechanical exfoliation technique. To enhance the optical contrast, the crystals were exfoliated onto a 90-nm SiO_2/Si wafer. Raman measurements on WS_2 samples were done at room temperature in backscattering geometry with a Horiba Jobin Yvon LabRAM HR spectrometer using a confocal setup with a 100× objective and excitation wavelengths of 457 and 633 nm. To avoid sample heating the laser power was kept below a maximum of 120 μW; an 1800 lines mm^{-1} grid was used to ensure high spectral resolution of around 1 cm^{-1}. First, Raman spectra were taken with the setup described above and calibrated with neon lines. In the second step the measurements were repeated in subpixel (6sp) mode. There, each spectrum is taken a couple of times, and each time the spectrometer is shifted by a step size which is smaller than a pixel value. This technique does not increase the spectral resolution, however, by providing more data points per wave number; it reduces the signal-to-noise ratio significantly. The spectra acquired in subpixel mode were then shifted in frequency to match the calibrated Raman spectra obtained in the regular

*Corresponding author: mstaiger@physik.tu-berlin.de

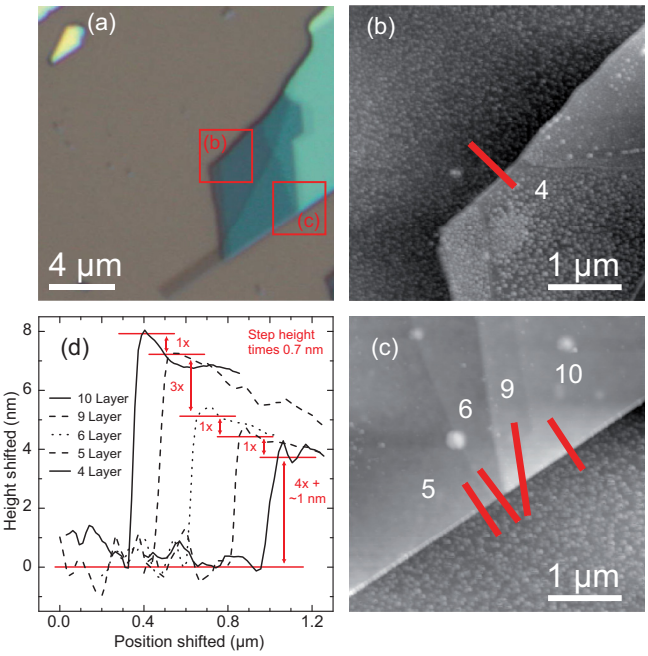

FIG. 1. (Color online) (a) Optical micrograph of a WS_2 flake with selected regions inspected by AFM [shown in (b) and (c)]. (b) and (c) AFM images of the selected regions with indication of layer numbers and lines showing where AFM height profiles were taken from. (d) AFM height profiles going from the substrate onto the flakes for different positions on the flake. Step heights in units of the observed interplanar spacing of ~0.7 nm are indicated.

single-window mode. For better comparison, in Figs. 2, 3, and 4, the spectra were normalized to the intensity of the out-of-plane mode.

Atomic force microscopy (AFM) images were acquired using a Park Systems XE-100 setup with commercial silicon tips in tapping-mode configuration. Images were taken with 256×256 pixel resolution (4×4 μm). An exemplary AFM analysis of a FL-WS_2 sample is shown in Fig. 1. Step heights between subsequent layer numbers were typically around 0.7 nm, close to the experimental value of the interplanar spacing of WS_2 layers [22]. Down to the monolayer, an offset of typically around 1 nm between substrate and sample was observed, which is probably due to the presence of adsorbates in between the substrate and the sample, and was taken into account in the analysis presented in Fig. 1.

The phonon frequencies of monolayer and FL-WS_2 at the Γ point were calculated in the frame of density functional (perturbation) theory on the level of the local-density approximation (LDA) as implemented in the CASTEP code [23]. We treated the $W(4d,5s)$ and the $S(3s,3p)$ states as valence electrons using norm-conserving pseudopotentials with a cutoff energy of 800 eV. All reciprocal space integrations were performed by a discrete k-point sampling of $18 \times 18 \times 1$ k points in the Brillouin zone. Starting from fully symmetric model geometries of one (1L) to five (5L) layers of AB-stacked WS_2, we fully optimized the lattice constants and atomic positions until the residual forces between atoms were smaller than 0.01 eV/Å and the stresses on the cell boundaries were smaller than 2.5×10^{-3} GPa. The obtained in-plane lattice constants slightly increased with layer number from a value of 3.141 Å for 1L-WS_2 to 3.143 Å for 5L-WS_2, in good agreement with the experimental in-plane lattice constant of 3.15 Å in bulk WS_2 [24]. Interactions of the sheet with residual periodic images due to the 3D boundary conditions were minimized by maintaining a vacuum layer of at least 20 Å.

III. RESULTS

WS_2, like MoS_2, crystallizes in the $2H$ trigonal prismatic structure where the tungsten atoms are sandwiched between two layers of sulfur atoms. Intralayer bonds are of covalent nature; the interlayer interaction is governed by weak van der Waals forces. Bulk WS_2 has the D_{6h} point group; the 6 atoms per unit cell result in 18 phonon modes at the Γ point of the hexagonal Brillouin zone [25]:

$$D_{6h}: \Gamma = A_{1g} + 2A_{2u} + B_{1u} + 2B_{2g} + E_{1g} + 2E_{1u} + E_{2u} + 2E_{2g}.$$

In the monolayer and for an odd number of layers (odd N), the symmetry is reduced to the D_{3h} point group. Therefore, odd N WS_2 do not have a center of inversion. The Γ-point phonon modes transform according to the following irreducible representation:

$$D_{3h}: \Gamma = \frac{3N-1}{2}(A_1' + A_2'' + E' + E'') + A_2'' + E', \quad N = 1,3,5,\ldots.$$

For an even number of layers (even N), WS_2 possesses a center of inversion; the symmetry is described by the point group D_{3d}:

$$D_{3d}: \Gamma = \frac{3N}{2}(A_{1g} + E_g + A_{2u} + E_u), \quad N = 2,4,6,\ldots.$$

Let us first consider the case where the excitation wavelength is far from resonance. Figure 2(a) shows Raman spectra of one to five WS_2 layers and the bulk material taken with an excitation wavelength of 457 nm. The two main Raman modes are the A_1' and A_{1g} modes around 420 cm^{-1} for odd and even N, respectively, and the E' and E_{2g}^1 modes around 355 cm^{-1} for odd N and even N, respectively. A clear upshift with increasing numbers of layers is seen for the out-of-plane A_1'/A_{1g} mode, whereas the in-plane E'/E_{2g}^1 mode slightly softens. This has been observed before for WS_2 [19,26] as well as for other TMDs [10,17,27,28]. The stiffening of the out-of-plane A mode is explained by the increasing interlayer interaction and the subsequent rise in restoring forces on the atoms with the number of layers [17]. The same should hold for the E mode, although to a lesser extent, as the atoms move in plane and the influence of interlayer interaction is thus expected to be smaller. However, the opposite trend is observed and has been attributed to dielectric screening of long-range Coulomb interactions [12]. Figure 2(b) depicts the change in frequency of the out-of-plane A and in-plane E mode with the number of layers and the frequency difference between the two modes, which increases from 60.4 to 65 cm^{-1} from the monolayer to the bulk.

If the exciting light is far from resonance, the spectra are dominated by Raman modes allowed in first-order scattering, as has been reported previously for WS_2 nanotubes [29]. If we

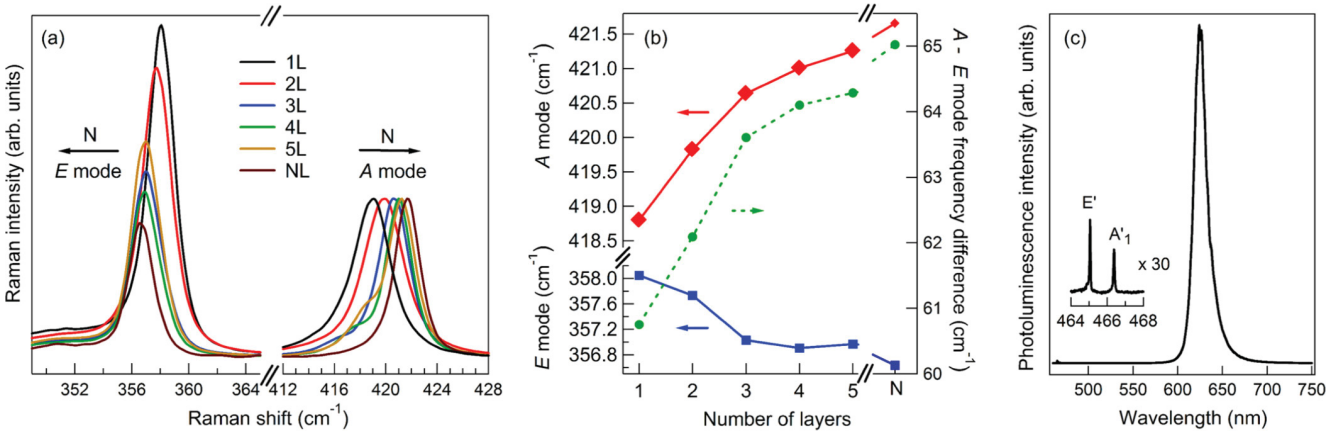

FIG. 2. (Color online) (a) Raman spectra of FL WS_2 from one (1L) to five (5L) layers and the bulk material (NL). Excitation wavelength is 457 nm. Spectra are normalized to the intensity of the A mode at 420 cm^{-1}. (b) Evolution of the frequency of the main E and A modes with the number of layers. The dashed line marks the increasing frequency difference between the modes with the number of layers. (c) Strong photoluminescence is observed for monolayer WS_2 at the direct excitonic transition energy around 625 nm. The inset shows a magnified image of the same spectrum in the region of the main 1L-WS_2 Raman peaks.

focus on the out-of-plane A modes, it is evident that the mono-, bilayer, and bulk spectra show a single peak, whereas for three or more layers there is at least another mode appearing as a low-energy shoulder of the dominant Raman feature. This apparent splitting of the out-of-plane mode is due to the fact that for monolayer and bulk WS_2 there is only one Raman-active A_1' mode and A_{1g} mode, respectively; for a few layers starting with three layers, more than one Raman mode becomes allowed (see also Ref. [21]).

To further explore these new Raman modes, we analyze the Raman spectra of the same samples taken under the resonance condition. Figure 2(c) shows a photoluminescence spectrum of monolayer WS_2 at 457-nm excitation wavelength. The photoluminescence signal is more than two orders of magnitude larger than the Raman signal and has maximum intensity around 625 nm. From previous experiments it is known that the first optical transition energy of bulk WS_2 is constituted by the A exciton around 633 nm [29]. Therefore, with 633-nm excitation wavelength, we are close to the A excitonic resonance for mono- and few-layer WS_2. In the remainder of this work we will focus on the out-of-plane A mode around 420 cm^{-1}. Of the four Raman modes allowed in bulk WS_2 D_{6h} symmetry, E^2_{2g} is too low in frequency to be observed here, the E_{1g} mode is not allowed in backscattering geometry, and the E^1_{2g} mode around 350 cm^{-1} overlaps with a second-order mode, which dominates the spectra in resonance [16]. As we will show below, the out-of-plane mode is clearly separated from other Raman features and shows sidebands that can readily be explained by the respective symmetries of even and odd numbers of layers.

Figure 3 shows the region of the out-of-plane Raman mode of few-layer WS_2 taken with 633-nm excitation wavelength. Similar to the spectra shown at 457-nm excitation wavelength, the upshift of the Raman mode with the number of layers is evident. More importantly, however, there are striking differences in the shape of the Raman mode. For FL-WS_2 the structure of the out-of-plane mode is complex. In contrast to the spectra described above, already the bilayer spectrum shows more than one component. More and more sidebands arise for an increasing number of layers, but they get weaker for $n > 5$ and vanish for very thick flakes ($n = N$). This again underlines the special role played by few-layer samples: for $n = 1$ and $n = N$ the symmetry of WS_2 allows only one

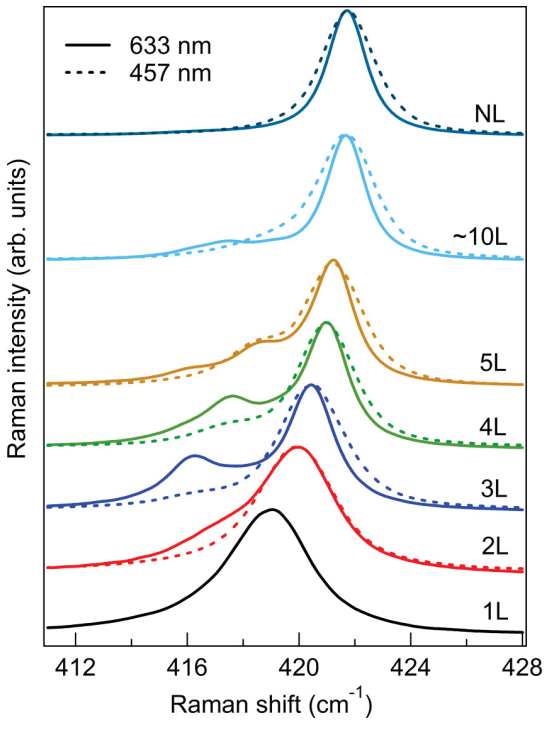

FIG. 3. (Color online) Experimental resonance Raman spectra (excitation wavelength 633 nm) of the A-mode region in FL-WS_2 from the bilayer (2L) to five layers (5L) and the bulk (NL). The monolayer spectrum (1L) is only shown with an excitation wavelength of 457 nm, as the Raman features are dominated by strong photoluminescence at 633-nm excitation spectrum (not shown). For FL-WS_2, spectra of the same region taken with the 457-nm excitation wavelength are overlaid and depicted with dashed lines. Spectra are normalized to the main Raman peak and are offset for clarity.

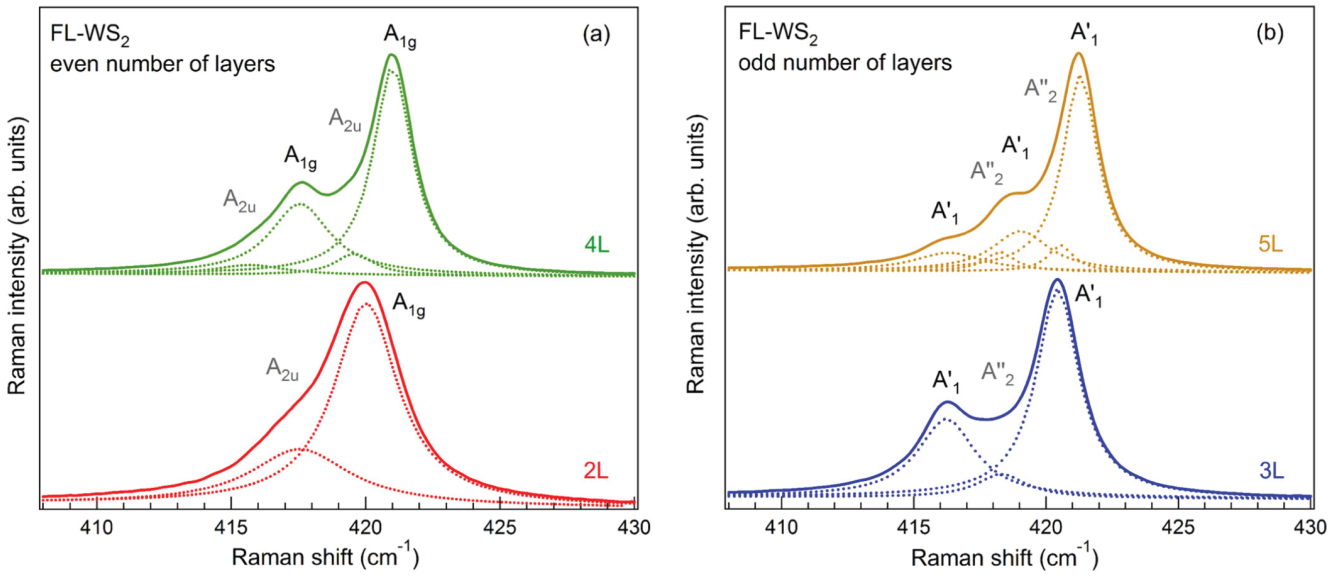

FIG. 4. (Color online) Experimental resonance Raman spectra of FL-WS_2. The Lorentzian fit curves are shown as well as the symmetry attributed to the individual modes. In general, there are N components for an N-layer spectrum. (a) For an even number of layers, Raman-active A_{1g} modes alternate with infrared-active A_{2u} modes. (b) For an odd number of layers, Raman-active A_1' modes alternate with infrared A_2'' modes. For both even and odd N, the Raman-active modes are more intense than the rather weak infrared-active modes.

A_1' ($n = 1$) and A_{1g} (bulk) Raman mode. The comparison with the out-of-resonance spectra (457-nm excitation wavelength) illustrates that, even though shoulders of the main Raman peak are observed at 457-nm excitation as well, an increased number of well-pronounced sidebands to the main Raman peak appears mainly for Raman measurements in resonance with the A exciton. We fit the spectra with Lorentzian profiles (see Fig. 4); for clarity spectra of even and odd N are shown in separate graphs. In Fig. 4(a) the bilayer A_{1g}-mode spectrum possesses a low-energy shoulder that has not previously been observed. Its appearance is surprising since the only expected Raman-active vibration is the A_{1g} mode, where both layers vibrate in phase according to the monolayer A_1' mode. We will show below that this second peak is indeed the infrared-active A_{2u} mode, where the two layers vibrate out of phase. In the four-layer (4L) spectrum the dominant A_{1g} mode shifts up with respect to the bilayer, and a prominent shoulder is seen at almost the same frequency as the shoulder in the bilayer spectrum. The 4L spectrum is best fitted with four Lorentzians to account for the Raman intensity between the two stronger Raman features. In the spectra of odd N WS_2, a similar pattern is revealed. In Fig. 4(b) the trilayer (3L) and five-layer (5L) spectra are shown. The former consists of the expected A_1' peak as the most significant contribution and a pronounced low-energy shoulder. A third Lorentzian fits the plateau between the main peaks. The 3L spectrum cannot be properly fitted with only two Lorentzians. From the experience gained from the spectra investigated above, the five-layer spectrum is fitted with five Lorentzians, two of which fill up the region between the main A_1' peak and the two low-energy shoulders. From the spectra for layer numbers of $n = 1$ to $n = 5$ it thus seems that there are always N components to the out-of-plane A mode, where N is the number of layers. We have observed sidebands on the lower-energy side of the dominant Raman peak also for higher layer numbers, as shown for the spectrum of an around ten-layer-thick flake. But they are rather weak and cannot be fitted following the pattern described above.

IV. DISCUSSION

Recently, careful analysis of few-layer TMDs has led to the observation of Raman modes that are seen neither in the bulk nor in the monolayer [10]. Some of them appear as shoulders to Raman modes that are allowed in first order for the bulk and monolayer, like the bulk A_{1g} mode discussed here. Others are Raman inactive or not allowed in backscattering geometry in the bulk and monolayer, like the bulk B_{2g} and E_{1g} modes [10,21,30,31]. For the first case, to the best of our knowledge, there is only one paper that explicitly shows a splitting of the first-order A_{1g} mode with the number of layers in few-layer $MoSe_2$ [10]. The 3L and 4L samples show two components; for the 5L sample a third component is seen. For WSe_2 the overlap of the bulk E_{2g}^1 and A_{1g} modes makes observation of such shoulders impossible [21,30], and for the case of $MoTe_2$ the intensity of the A_{1g} mode appears to be too small to resolve a multipeak structure [28]. For MoS_2 there is little information on resonance Raman spectra, and despite some asymmetry in the shape of the out-of-plane Raman mode, a splitting similar to the one investigated in this work is not observed [32,33]. Terrones *et al.* [21] calculate the optical phonons for a number of FL-TMDs, among them MoS_2 and WS_2, but do not discuss phonons other than the Raman-active ones.

In order to have a theoretical background on the experimentally observed appearance of more than just the Raman-active vibrational modes in the spectra of FL-WS_2, we have performed calculations employing DFT. Better insight into the atomic displacements corresponding to the phonon modes of FL-TMDs is given in Fig. 5, where schematic drawings

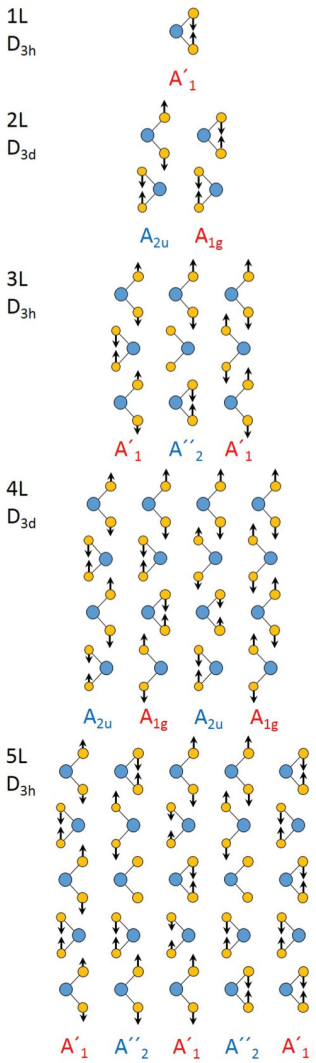

FIG. 5. (Color online) Schematic drawing for all possible vibrational modes in the out-of-plane mode region of FL-WS_2 (Raman and infrared) for one (1L) to five (5L) layers together with the symmetry assignments taken from our DFT calculations. The displacement patterns are ordered with increasing frequency from left to right. Taking into account the full set of possible vibrational patterns helps us to study the splitting of vibrational modes with increasing layer number and to attribute the modes to the features seen in the Raman spectra.

of all possible vibrations evolving from the monolayer A_1' mode in WS_2 from $n = 1$ to 5 are depicted based on the DFT calculations. While there is only one possibility in monolayer WS_2 for the sulfur atoms to vibrate against each other with a fixed tungsten atom in between, a splitting of this mode occurs for bilayer WS_2. Since bilayer WS_2 possesses a center of inversion, there is a Raman-active A_{1g} mode, where the two layers vibrate in phase, and an infrared-active A_{2u} mode, where the two layers vibrate out of phase. As the latter is not Raman active, it is not seen in Raman spectra taken with excitation wavelengths far from resonance [Fig. 2(a)]. However, it is observed for the resonance Raman spectrum (Figs. 3 and 4), albeit with weaker intensity than the dominant A_{1g} mode. Several possible reasons for this unusual behavior are discussed below. As the two layers interact more strongly for the in-phase vibration, the A_{1g} mode has a slightly higher frequency than its infrared-active counterpart. For 4L-WS_2, each of the two bilayer modes again splits up into a Raman-active A_{1g} mode and an infrared-active A_{2u} mode. The spectrum is still governed by the in-phase vibration of all four layers (A_{1g}), but there is a second Raman-active A_{1g} mode that has the outer layers vibrating out of phase with the inner ones, thus retaining the inversion symmetry of the overall structure. It is interesting to note that this lower-lying A_{1g} mode in the 4L spectrum has almost the same frequency as the infrared-active mode in the bilayer, a pattern that will also be observed for odd N (see below). In addition, we identify the two small shoulders on the lower-frequency side of the two Raman-active modes with the A_{2u} modes [Fig. 4(a)], the lowest lying with neighboring layers vibrating out of phase and the other one with the two upper layers vibrating out of phase with the two lower layers.

In odd N WS_2 there is obviously again the possibility of all layers vibrating in phase and out of phase. In contrast to even N WS_2, where the pure out-of-phase vibration is not Raman active, for odd N both in- and out-of-phase vibrations are Raman active and possess A_1' symmetry. For trilayer WS_2, the atomic displacement vectors of these two modes are shown on the right and left sides of the third panel in Fig. 5. In the spectrum depicted in Fig. 4(b), the lower-lying A_1' mode accounts for the strong shoulder at approximately 416 cm^{-1} of the main A_1' mode (in-phase vibration). In between the modes a plateau is evident that is not accounted for if the spectrum is fitted with only two Lorentzians. The origin of the plateau is attributed to an infrared-active A_2'' mode, with the middle layer fixed and the sulfur atoms of the top and bottom layers vibrating out of phase (see Fig. 5, third panel, middle). The same approach can now be used for the analysis of the five-layer WS_2 spectrum. Two shoulders to the main A_1' peak can be identified and, following the pattern of Fig. 5, can be attributed to another two Raman-active A_1' modes. In between the Raman-active modes two very weak features belong to infrared-active A_2'' vibrations. Coming from the trilayer WS_2, the two modes with the highest frequency in the five-layer material can be imagined as stemming from a splitting of the main Raman-active A_1' mode in the trilayer. The same can be said about the lower-frequency Raman-active mode in the trilayer that splits up into the low-frequency A_1' and A_2'' modes in five layers. The only infrared-active A_2'' mode in the trilayer spectrum changes symmetry in the five-layer spectrum and has the two outermost layers vibrating out of phase with the three inner ones.

To summarize, to analyze the Raman spectra of one to five layers of WS_2, it is necessary to take into account the full set of phonon modes. For the evolvement of the monolayer A_1' mode analyzed in detail here, the number of out-of-plane modes matches the number of layers. Raman-active modes alternate with modes that are infrared active and are now seen in the spectra of FL-WS_2. The pattern observed for the out-of-plane mode should also be valid for all other vibrational modes in FL-WS_2 and other FL-TMD materials. For even N, the monolayer mode splits up into $\frac{N}{2}$ Raman-active and $\frac{N}{2}$ infrared-active modes (the in-plane modes are always doubly degenerate). For odd N, the monolayer mode evolves into $\frac{N+1}{2}$

TABLE I. Experimental Raman frequencies (in cm^{-1}) of all vibrational modes observed in FL-WS_2 excited with 633 nm. For N layers the A_1' mode of the monolayer splits up into N components. The point group of FL-WS_2 is D_{3h} for an odd number of layers and D_{3d} for an even number of layers. The vibrational modes for every number of layers alternate between Raman (R) and infrared active (IR).

	1L	2L	3L	4L	5L
R	A_1'(418.8)	A_{1g} (420.0)	A_1' (420.5)	A_{1g} (421.0)	A_1'(421.3)
IR		A_{2u} (417.3)	A_2'' (418.5)	A_{2u} (419.9)	A_2'' (420.4)
R			A_1'(416.2)	A_{1g} (417.8)	A_1' (418.8)
IR				A_{2u} (416.0)	A_2''(418.0)
R					A_1' (416.2)

Raman-active and $\frac{N-1}{2}$ infrared-active components. In total, in N layers, each of the monolayer phonons splits up into N phonon modes [30,31].

Table I lists the experimentally obtained Raman frequencies of all out-of-plane vibrations derived from the A_1' mode at 418.8 cm^{-1} for few-layer WS_2. Where two or more samples with the same number of layers were measured, the average value is given in Table I. In all these cases deviations from the given frequencies are less than 0.3 cm^{-1}. Again, the table illustrates that Raman- and infrared-active modes are alternating irrespective of the layer number. Additionally, not only does the main Raman-active component with A_1'/A_{1g} symmetry for odd and even N appear to exhibit increased frequency with an increasing number of layers, but also the other components (second row and below in Table I) follow the same trend. This is illustrated in Fig. 6(a), where the tabulated frequencies are plotted against the number of layers. The main Raman peak in the spectra shown in Figs. 2–4 is seen stiffening in frequency from the monolayer to five layers (red circles, connected by a dashed line to guide the eye). Starting with the bilayer, an infrared-active mode comes into play that also appears for higher layer numbers. It also increases in frequency, thus following the behavior of the main Raman component due to increased force constants with an increasing number of layers (blue squares, connected by a dashed line to guide the eye). The same is seen for a second Raman-active feature starting with three layers and another infrared-active mode starting with four layers. Interestingly, the frequencies observed in the mono-, bi-, and trilayer are almost exactly repeated when the layer number is increased by two, underlining the close relation of the out-of-plane modes even though the symmetry and Raman/infrared activity changes with the layer number. In contrast, the position of the lowest-frequency mode stays almost constant from three layer onwards. This mode always has neighboring layers moving out of phase but neighboring sulfur atoms from adjacent layers moving in phase. As a result, the nearest-neighbor force constants determining the frequency of this mode will not change significantly for larger numbers of layers. In Fig. 6(b), the frequencies calculated with DFT are plotted against the layer number. Despite a slight overestimation of absolute frequencies and a smaller magnitude of the splitting of the modes, the experimental results are well reproduced. As a whole, the splitting of the out-of-plane monolayer A_1' mode in FL-WS_2 results in a fanlike shape showing similarity to Fig. 5 in Ref. [20]. Zhang *et al.* [20] investigated the evolvement of the low-frequency rigid layer C (displacement along the c direction) and LB (layer breathing) modes in FL-MoS_2 (another report on these interlayer modes in few-layer MoS_2

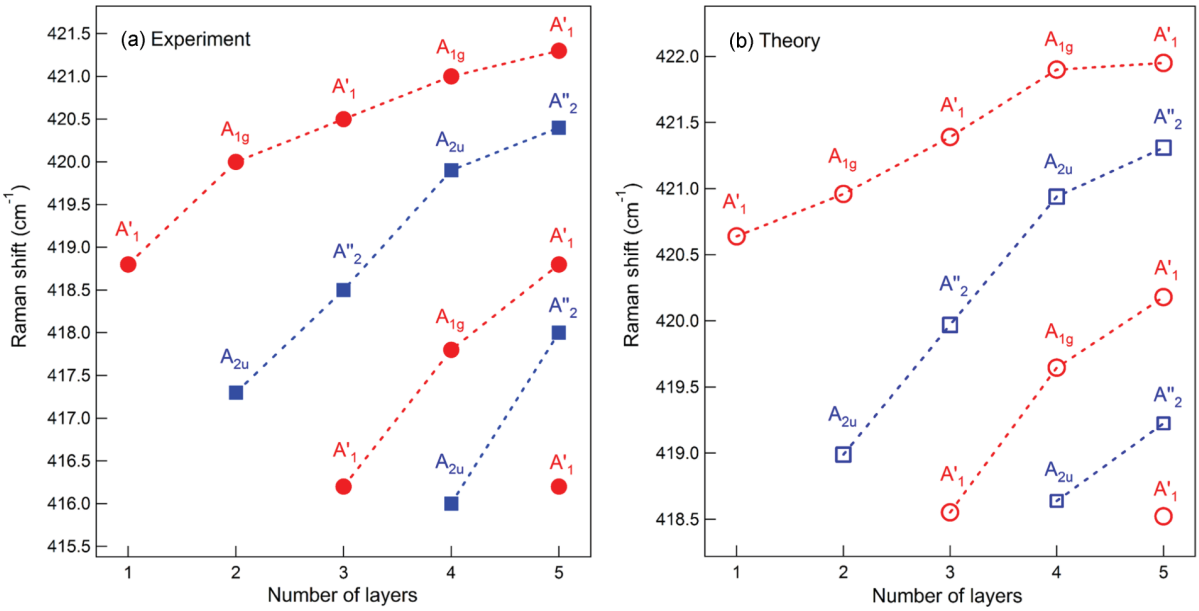

FIG. 6. (Color online) (a) Raman frequencies of the A-type modes in FL-WS_2. Red circles mark the Raman-active modes; blue squares denote the infrared-active modes also seen in the Raman spectra. Dashed lines are used to guide the eye. Starting from one layer, the splitting of the modes for FL-WS_2 produces a fanlike shape of the possible vibrational frequencies. (b) Theoretical calculations with DFT reproduce the observed trends. Raman-active modes are denoted with open red circles; infrared-active modes are marked with open blue squares.

can be found in Ref. [34]). With the support of a simple atomic chain model the authors found a behavior similar to the one described here for the out-of-plane vibration in WS_2. Obviously, rigid-layer vibrations appear starting only from the bilayer. Strictly speaking, the difference from all other optical modes in FL-TMDs is that there are, consequently, only $N-1$ possible vibrations (where N denotes the layer number) for the rigid-layer modes (E^2_{2g} and B_{2g} symmetry in bulk MoS_2). Of course, the "N modes for N layers rule" is restored again if one adds the acoustic modes. The acoustic E' and A''_2 modes of the monolayer are the origin of the low-frequency vibrations in FL-TMDs and will split up into N components for N layers (among them A- and E-type modes with zero frequency).

The behavior described above should, in principle, be observable in other 2H-TMDs as well. Terrones *et al.* [21] predict an increased splitting of the Raman-active components in the order WSe_2, $MoSe_2$, WS_2, and MoS_2. What distinguishes WS_2 from other prominent $2H$-TMDs such as WSe_2 and MoS_2 is that the bulk A_{1g} and E^1_{2g} modes are well separated in energy and that no second-order Raman features overlap with the A_{1g} mode, thus making it easier to resolve the splitting of the out-of-plane mode into Raman and infrared-active components. More importantly, measuring in resonance with the optical transition appears to be a necessary condition to observe the full set of vibrational modes. There is a lack of studies on Raman spectra of other FL-$2H$-TMDs measured under the resonance condition; often, the corresponding excitation wavelengths are avoided because in the monolayer case the Raman features are obscured by a strong photoluminescence signal. In FL-WS_2 in particular, the characteristic shape of the out-of-plane mode in resonance Raman spectra can be used as a fingerprint region to unambiguously identify the number of layers.

For WS_2 measured under the resonance excitation, even in the bulk material, the A_{1g} out-of-plane mode is accompanied by a small shoulder that is attributed to the silent B_{1u} mode [12,16,29]. It had been previously attributed to a $LA(K)+TA(K)$ combination mode [35], but the participation of two phonon modes involving acoustic phonons in this frequency region seems unlikely, especially in light of more recent DFT calculations showing that nowhere in the Brillouin zone do the acoustic phonons reach values above 200 cm^{-1} [12]. The in-phase and out-of-phase vibrational pattern of the A_{1g}/B_{1u} pair in bulk WS_2 finds its counterpart in the variety of in- and out-of-phase vibrations observed in FL-WS_2. In WS_2 nanomaterials, the B_{1u} mode gains in Raman intensity, and its evolvement can be followed in WS_2 nanomaterials under pressure [29,36], in different layer orientations in thin films [37], and in WS_2 nanotubes with different diameters [29,38]. In these cases, a strong resonance behavior is observed as well, much like in FL-WS_2: the modes not allowed in a first-order Raman process appear most strongly when the excitation energy is in or close to resonance with the optical transitions. In an earlier work on WS_2 nanotubes [29], we found that the curvature-induced strain and the resultant crystal symmetry distortion accounted for the activation of silent modes. Here, in quasi-2D materials, the situation in the absence of curvature effects is different; strain due to substrate-sample interaction is assumed to play only a very minor role in Raman spectroscopy on supported FL-TMDs [20].

Instead, a closer look at the nature of the excitonic transition leading to the resonantly enhanced Raman intensity in the spectra of FL-WS_2 can provide the means to elucidate the appearance of the infrared-active components of the A'_1/A_{1g} Raman mode around 420 cm^{-1}. For a 633-nm excitation wavelength, the phonons couple to the A exciton situated at the K point of the Brillouin zone. Owing to the structural relationship between strong intralayer bonding in two dimensions and weak interlayer interaction in the third dimension, like many properties of layered TMD systems, the wave functions of the excitons are expected to be very anisotropic. A recent work on the orientation of luminescent excitons in FL-MoS_2, isostructural to FL-WS_2, reveals them to be confined entirely in plane without significant expansion in the stacking direction of individual layers [39]. This was further substantiated by DFT calculations in the LDA that explicitly showed the wave function of the A exciton in multilayer MoS_2 to be spread out over a large area in two dimensions but with negligible density in neighboring layers [40]. For the resonant Raman process discussed here this means that even for a layer number of more than one, the phonon couples to an A exciton localized primarily in one of the layers. If the N layers in FL-WS_2 are to be treated approximately as N individual monolayers for the specific case of the A excitonic resonant Raman process, there are N Raman-allowed Raman modes to be expected in the region of the monolayer A'_1 Raman mode with similar Raman intensities. They are still split in frequency due to interlayer interaction. Here, all N components are identified in the Raman measurements presented in this paper, but the infrared-active components, speaking from the N-layer symmetry point of view, are always weaker in intensity than the Raman-active components. Thus, we conclude that Raman selection rules are at least weakened but not completely broken. This is supported by the fact that the Raman-active components gain in intensity relative to the main Raman peak but still appear as shoulders rather than as individual peaks.

Far from the A excitonic resonance, the few-layer WS_2 cannot be treated as N individual monolayers, and the Raman selection rules following from the few-layer symmetry strictly apply. This is also in agreement with recent findings on newly observed Raman modes in FL-MoS_2 in resonance with the C exciton [31].

V. CONCLUSION

In summary, we have shown experimentally as well as theoretically that the out-of-plane A'_1 mode of the WS_2 monolayer splits up in the few-layer regime into N components for N layers. Despite the fact that only $\frac{N}{2}$ of them for an even number of layers and $\frac{N+1}{2}$ for an odd number of layers are Raman active, the full set of phonon modes is observed when the laser excitation energy is close to the A excitonic transition energy. A possible explanation for this unusual behavior is presented by taking into account the in-plane orientation of the A exciton wave function involved in the resonant Raman scattering process. The stiffening of the main out-of-plane phonon mode with N is also followed by all other components successively added with an increasing number of layers. Using resonant Raman scattering measurements,

one can conclusively identify the number of layers in a specific sample by simply counting the number of components of the out-of-plane A mode. The detailed analysis of the evolvement of the A_1' mode of monolayer WS_2 presented here should, in principle, be applicable to (i) all other Raman modes of (ii) all layered materials in the few-layer regime.

ACKNOWLEDGMENTS

This work was supported by the Deutsche Forschungsgemeinschaft (DFG) in the Priority Programme SPP 1459 "Graphene" and by the European Research Council (ERC) through Grant No. 259286. We thank L. Madauß for his support with sample preparation.

[1] M. Chhowalla, H. S. Shin, G. Eda, L.-J. Li, K. P. Loh, and H. Zhang, Nat. Chem. **5**, 263 (2013).

[2] Z. Ye, T. Cao, K. O'Brien, H. Zhu, X. Yin, Y. Wang, S. G. Louie, and X. Zhang, Nature (London) **513**, 214 (2014).

[3] B. Zhu, H. Zeng, J. Dai, Z. Gong, and X. Cui, Proc. Natl. Acad. Sci. USA **111**, 11606 (2014).

[4] A. Ramasubramaniam, Phys. Rev. B **86**, 115409 (2012).

[5] Q. Wang, K. Kalantar-Zadeh, A. Kis, J. Coleman, and M. S. Strano, Nat. Nanotechnol. **7**, 699 (2012).

[6] H. Wang, H. Feng, and J. Li, Small **10**, 2165 (2014).

[7] B. Zhu, H. Zeng, J. Dai, and X. Cui, Adv. Mater. **26**, 5504 (2014).

[8] A. Splendiani, L. Sun, Y. Zhang, T. Li, J. Kim, C.-Y. Chim, G. Galli, and F. Wang, Nano Lett. **10**, 1271 (2010).

[9] K. F. Mak, C. Lee, J. Hone, J. Shan, and T. F. Heinz, Phys. Rev. Lett. **105**, 136805 (2010).

[10] P. Tonndorf, R. Schmidt, P. Böttger, X. Zhang, J. Börner, A. Liebig, M. Albrecht, C. Kloc, O. Gordan, D. R. T. Zahn, S. M. de Vasconcellos, and R. Bratschitsch, Opt. Express **21**, 4908 (2013).

[11] H. S. S. R. Matte, A. Gomathi, A. K. Manna, D. J. Late, R. Datta, S. K. Pati, and C. N. R. Rao, Angew. Chem. Int. Ed. **122**, 4153 (2010).

[12] A. Molina-Sanchez and L. Wirtz, Phys. Rev. B **84**, 155413 (2011).

[13] M. Thripuranthaka and J. Dattatray, ACS Appl. Mater. Interfaces **6**, 1158 (2014).

[14] A. A. Mitioglu, P. Plochocka, G. Deligeorgis, S. Anghel, L. Kulyuk, and D. K. Maude, Phys. Rev. B **89**, 245442 (2014).

[15] T. Wieting and J. Verble, Phys. Rev. B **3**, 4286 (1971).

[16] C. Sourisseau, M. Fouassier, M. Alba, A. Ghorayeb, and O. Gorochov, Mater. Sci. Eng. B **3**, 119 (1989).

[17] C. Lee, H. Yan, L. E. Brus, T. F. Heinz, J. Hone, and S. Ryu, ACS Nano **4**, 2695 (2010).

[18] G. Plechinger, S. Heydrich, J. Eroms, D. Weiss, C. Schüller, and T. Korn, Appl. Phys. Lett. **101**, 101906 (2012).

[19] A. Berkdemir, H. R. Gutiérrez, A. R. Botello-Méndez, N. Perea-López, A. L. Elías, C.-I. Chia, B. Wang, V. H. Crespi, F. López-Urías, J.-C. Charlier, H. Terrones, and M. Terrones, Sci. Rep. **3**, 1755 (2013).

[20] X. Zhang, W. P. Han, J. B. Wu, S. Milana, Y. Lu, Q. Q. Li, A. C. Ferrari, and P. H. Tan, Phys. Rev. B **87**, 115413 (2013).

[21] H. Terrones, E. Del Corro, S. Feng, J. M. Poumirol, D. Rhodes, D. Smirnov, N. R. Pradhan, Z. Lin, M. A. T. Nguyen, A. L. Elías, T. E. Mallouk, L. Balicas, M. A. Pimenta, and M. Terrones, Sci. Rep. **4**, 4215 (2014).

[22] J. Wilson and A. Yoffe, Adv. Phys. **18**, 193 (1969).

[23] S. J. Clark, M. D. Segall, C. J. Pickard, P. J. Hasnip, M. J. Probert, K. Refson, and M. Payne, Z. Kristallogr. **220**, 567 (2005).

[24] W. Schutte, J. D. Boer, and F. Jellinek, J. Solid. State Chem. **70**, 207 (1987).

[25] J. Verble and T. Wieting, Phys. Rev. Lett. **25**, 362 (1970).

[26] W. Zhao, Z. Ghorannevis, K. K. Amara, J. R. Pang, M. Toh, X. Zhang, C. Kloc, P. H. Tane, and G. Eda, Nanoscale **5**, 9677 (2013).

[27] D. Late, B. Liu, H. Matte, C. Rao, and V. Dravid, Adv. Funct. Mater. **22**, 1894 (2012).

[28] M. Yamamoto, S. T. Wang, M. Ni, Y.-F. Lin, S.-L. Li, S. Aikawa, W.-B. Jian, K. Ueno, K. Wakabayashi, and K. Tsukagoshi, ACS Nano **8**, 3895 (2014).

[29] M. Staiger, P. Rafailov, K. Gartsman, H. Telg, M. Krause, G. Radovsky, A. Zak, and C. Thomsen, Phys. Rev. B **86**, 165423 (2012).

[30] X. Luo, Y. Zhao, J. Zhang, Q. Xiong, and S. Y. Quek, Phys. Rev. B **88**, 075320 (2013).

[31] N. Scheuschner, R. Gillen, M. Staiger, and J. Maultzsch, Phys. Rev. B (to be published).

[32] N. Scheuschner, O. Ochedowski, M. Schleberger, and J. Maultzsch, Phys. Status Solidi B **249**, 2644 (2012).

[33] H. Li, Q. Zhang, C. C. R. Yap, B. K. Tay, T. H. T. Edwin, A. Olivier, and D. Baillargeat, Adv. Funct. Mater. **22**, 1385 (2012).

[34] H. Zeng, B. Zhu, K. Liu, J. Fan, X. Cui, and Q. M. Zhan, Phys. Rev. B **86**, 241301(R) (2012).

[35] C. Sourisseau, F. Cruege, M. Fouassier, and M. Alba, Chem. Phys. **150**, 281 (1991).

[36] S. D. Yu, L. X. Chang, H. B. Yang, B. B. Liu, Y. Y. Hou, L. Wang, M. G. Yao, T. Cui, and G. T. Zou, J. Phys. Condens. Matter **19**, 425228 (2007).

[37] J. Chung, Z. Dai, K. Adib, and F. Ohuchi, Thin Solid Films **335**, 106 (1998).

[38] M. Krause, M. Viršek, M. Remškar, N. Salacan, N. Fleischer, L. Chen, P. Hatto, A. Kolitsch, and W. Möller, ChemPhysChem **10**, 2221 (2009).

[39] J. A. Schuller, S. Karaveli, T. Schiros, K. He, S. Yang, I. Kymissis, J. Shan, and R. Zia, Nat. Nanotechnol. **8**, 271 (2013).

[40] A. Molina-Sánchez, D. Sangalli, K. Hummer, A. Marini, and L. Wirtz, Phys. Rev. B **88**, 045412 (2013).

B.3. Physical Review B 94, 035430 (2016)

PHYSICAL REVIEW B **94**, 035430 (2016)

Raman spectroscopy of intercalated and misfit layer nanotubes

Matthias Staiger,[1,*] Vladimir Bačić,[2] Roland Gillen,[1] Gal Radovsky,[3] Konstantin Gartsman,[4] Reshef Tenne,[3] Thomas Heine,[2,5] Janina Maultzsch,[1] and Christian Thomsen[1]

[1]*Institut für Festkörperphysik, Technische Universität Berlin, Hardenbergstr. 36, 10623 Berlin, Germany*
[2]*Department of Physics and Earth Sciences, Jacobs University Bremen gGmbH Campus Ring 1, 28759 Bremen, Germany*
[3]*Department of Materials and Interfaces, Weizmann Institute of Science, Rehovot 76100, Israel*
[4]*Electron Microscopy Unit, Weizmann Institute of Science, Rehovot 76100, Israel*
[5]*Wilhelm-Ostwald-Institut für Physikalische und Theoretische Chemie, Linnéstr. 2, 04103 Leipzig, Germany*

(Received 12 January 2016; revised manuscript received 23 June 2016; published 18 July 2016)

We present Raman spectra of misfit layer $(PbS)_{1.14}NbS_2$ nanotubes and lead intercalated NbS_2 nanotubes. They represent interesting model systems to investigate the nature of interlayer interaction in layered materials. A direct correlation to the Raman modes of the parent $2H$-NbS_2 compound exists, but some modes are seen drastically upshifted in frequency in the misfit layer and intercalated compound while others remain almost unchanged. On the basis of the Raman spectroscopic investigations and with the help of supporting calculations we examine different interlayer bonding mechanisms and contribute to the discussion as to why these frequency shifts occur.

DOI: 10.1103/PhysRevB.94.035430

I. INTRODUCTION

In recent years transition metal dichalcogenide nanostructures (TMDCs) attracted a lot of interest. TMDCs span a wide variety of structures and physical properties, ranging from isolators to semiconductors, metals, and superconductors. Like for carbon based compounds, dimensionality is an important factor determining the properties of TMDCs. Apart from mono- and few-layer quasi-two-dimensional structures a number of TMDC nanotubes has been successfully synthesized [1]. Recently, there were first reports on the synthesis and characterization of nanotubes consisting of alternating layers of SnS/PbS and SnS_2/NbS_2 rolled up so as to reduce the lattice mismatch between the two materials [2–4]. These nanotubes belong to the family of misfit layer compounds (MLCs) composed of transition metal dichalcogenides TX_2 (T = Ti, V, Cr, Nb, Ta and the main group metal Sn; X = S, Se) and layers MX and RX (M = Sn, Pb, Sb, Bi, R = rare earth metals).

In their bulk form MLCs have been investigated for decades [5–8], and research has made evident that the possibility of combining these very different classes of materials makes for a plethora of structures and physical properties. They all have in common that they crystallize in highly ordered anisotropic structures, as will be detailed below. Consequently, research has always been accompanied by the question as to why these structures are so remarkably stable. A diverse set of methods ranging from (angle-resolved) photoelectron spectroscopy [9,10], electron microprobe analysis [11], photoemission microspectroscopy [12], bond valence [13] and *ab initio* density functional calculations [14], and not least Raman spectroscopy [15–19] have all been dedicated to gain insight into the nature of interlayer interaction governing the overall stability of MLCs. Apart from the intrinsic importance of MLCs as a model system for studying interlayer interaction and how intercalation can change the electronic properties of the host structure in layered systems, MLCs exhibit interesting thermoelectric properties [20–23], and many of them are superconductors [24]. With current research on layered materials increasingly focusing on low-dimensional systems, an ever growing family of tubular misfit layer compounds has been recently synthesized [2–4,25–27], but studies on their electronic and optical properties are as yet scarce [28]. In this context the present study aims to revisit studies on the properties of bulk MLCs and apply the findings to their nanostructured counterparts. Here, Raman spectroscopy has been the method of choice as it not only uncovers the vibrational properties but provides information about the electronic structure of the investigated materials. As such, this study contributes to the deciphering of the nature of interlayer interaction in tubular misfit layer nanostructures. The focus lies on representatives of a larger family of nanotubes, $(PbS)_{1.14}$-NbS_2 and Pb-intercalated NbS_2 nanotubes, where both components are low temperature superconductors [29].

Structurally similar to their bulk counterparts, in the rolled up TX_2 layers, transition metal atoms are sandwiched between six chalcogenide atoms whereas the MX and RX layers commonly adopt a distorted rock salt structure. The layers are stacked along the c axis. With a few exceptions, the layers share a common b axis length. The a axes are incommensurate meaning that the ratio of the two a sublattice constants is irrational. This affects the stoichiometry of the overall system which is expressed by the index x in $(MX)_xTX_2$.

In $(PbS)_{1.14}NbS_2$, a two atoms thick part of the PbS bulk structure is cut out to form a planar composite structure alternating with NbS_2 layers. The cubic symmetry of the lead sulfide layer is broken in the misfit layer compound with the Pb atoms protruding into the van der Waals gap between the layered subsystems. Electronically, bulk PbS is a narrow-gap semiconductor (E_{gap} = 0.42 eV [30]). NbS_2 crystallizes in trigonal prismatic coordination, where the Nb atom is placed between six sulfur atoms forming two tetrahedrons. In contrast to other $2H$-dichalcogenides like MoS_2 and WS_2, which exhibit a transition from an indirect to a direct band gap material once the thickness has been reduced to

*Corresponding author: mstaiger@physik.tu-berlin.de

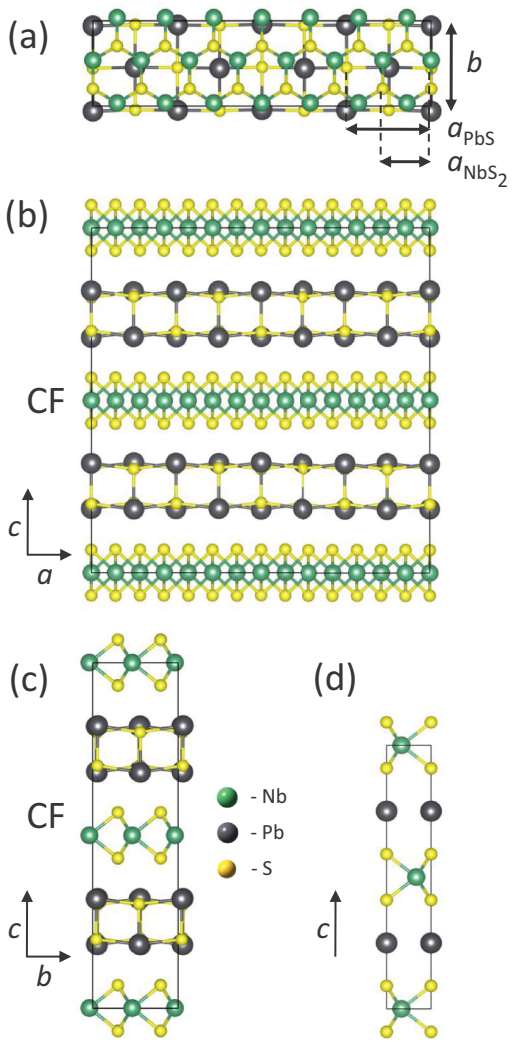

FIG. 1. (a) Structure of the misfit layer compound $(PbS)_{1.14}NbS_2$ in the *a*-*b* plane. The ratio of the *a* axes is irrational, therefore the compounds are classified as misfit layer compounds (MLC). (b) and (c): The structure of the misfit compound viewed along the commensurate *b* and the incommensurate *a* direction, respectively. (d) View along the normal to the (11.0) plane according to the pseudo-hexagonal system of labeling of the NbS_2 material intercalated with lead atoms in linear coordination to neighboring S atoms (ICSD col. code. 74698).

a monolayer, NbS_2 stays a metal even in the two-dimensional limit [31]. The metal character stems from a partially filled $4d_{z^2}$ Nb orbital around the Fermi energy. In the misfit layer compound (MLC) the NbS_2 layers remain fairly rigid and almost preserve the structure of the pristine $2H$-NbS_2 [14]. Figure 1(a) shows a view on the *a*-*b* plane of the $(PbS)_{1.14}NbS_2$ compound. In the simple orthorhombic conventional unit cell, the sublattices share a common *b* lattice constant, but the *a* lattice constants stay incommensurate with a lattice ratio of $a_{PbS}/a_{NbS_2} \approx \sqrt{3}$ which makes for $4a_{PbS} \approx 7a_{NbS_2}$ [32]. In Figs. 1(b) and 1(c) a view along the two in-plane lattice directions is depicted. Along the *c* direction, the CF stacking sequence is common in bulk $(PbS)_{1.14}NbS_2$ [7], but loses its validity in the misfit nanotubes. The conventional unit cell contains 28 units of NbS_2 and 32 units of PbS, which makes for the index of 1.14. Between the layers, besides the van der Waals interaction, some coordinative bonding may exist. In misfit layer compounds, the MX material is often characterized as the intercalant in between the TX_2 layers.

This is also the case in the second type of nanotubes investigated in this study, Pb-NbS_2 nanotubes, where the lead undoubtedly can be described as an intercalant. Here, the Pb atoms are, rather unusually, linearly coordinated to two S atoms of the adjacent NbS_2 slabs, as can be seen in Fig. 1(d). Thus in the *c* direction not the metal atoms but the S atoms are found on top of each other [4,33]. The expected atomic ratio of 1:1 between the niobium and the lead atoms was confirmed previously in Ref. [34]. Strictly speaking, the Pb-NbS_2 nanotubes are thus not misfit layer compounds but, as we will see, the intercalants have strikingly similar effect on the Raman spectra of the host NbS_2 layer as the lead sulfide layers in the MLC.

In this paper we present Raman spectra of $(PbS)_{1.14}NbS_2$ nanotubes and NbS_2 nanotubes intercalated with lead. While the vibrational properties of the former can be compared to its parent material, the latter has not been investigated before. Our focus lies on the changes in the Raman frequencies of the misfit layer and intercalated materials compared to the pristine compound. The different mechanisms of interlayer bonding are critically discussed on the basis of the results of the Raman spectroscopic investigation. The popular charge transfer hypothesis is challenged experimentally as well as theoretically, and we propose an alternative way to explain the drastic Raman frequency upshifts observed in both compounds.

A. Experiment

Pb-Nb-S tubular structures were synthesized via chemical vapor transport technique in evacuated quartz ampules as was described in Ref. [4]. Reference [4] also describes in detail the characterization process. Prior to Raman measurements (high resolution) TEM images were taken of each nanotube and the respective type was identified by determining the layer periodicities. In Fig. 2(a) this can be seen for a Pb-NbS_2 nanotube with 0.88 nm periodicity (NbS_2 layer and atomic Pb layers are alternating). The same is shown for a $(PbS)_{1.14}NbS_2$ misfit layer nanotube in Fig. 2(b). Here, PbS and NbS_2 layers are alternating, resulting in a 1.20 nm periodicity. Additionally, energy-dispersive x-ray (EDS) spectra and selected area electron diffraction (SAED) patterns were at hand and are described in Ref. [4]. Raman spectra of individual misfit layer nanotubes were recorded in backscattering geometry employing a frequency doubled Nd:YAG laser emitting at 532 nm. The scattered light was analyzed using a LabRam HR spectrometer with a 600/mm grating and a Peltier-cooled charge-coupled device. The spectral resolution was approximately 2 cm^{-1}. Laser power had to be limited to 130 μW so as to avoid burning the underlying thin carbon TEM substrate. Due to the investigated materials being rather poor Raman scatterers, accumulation times exceeded 20 minutes in most cases and several spectra recorded at the same position of the sample had to be summed to get appreciable signal.

Density functional theory (DFT) calculations were carried out using the local-density approximation (LDA), with

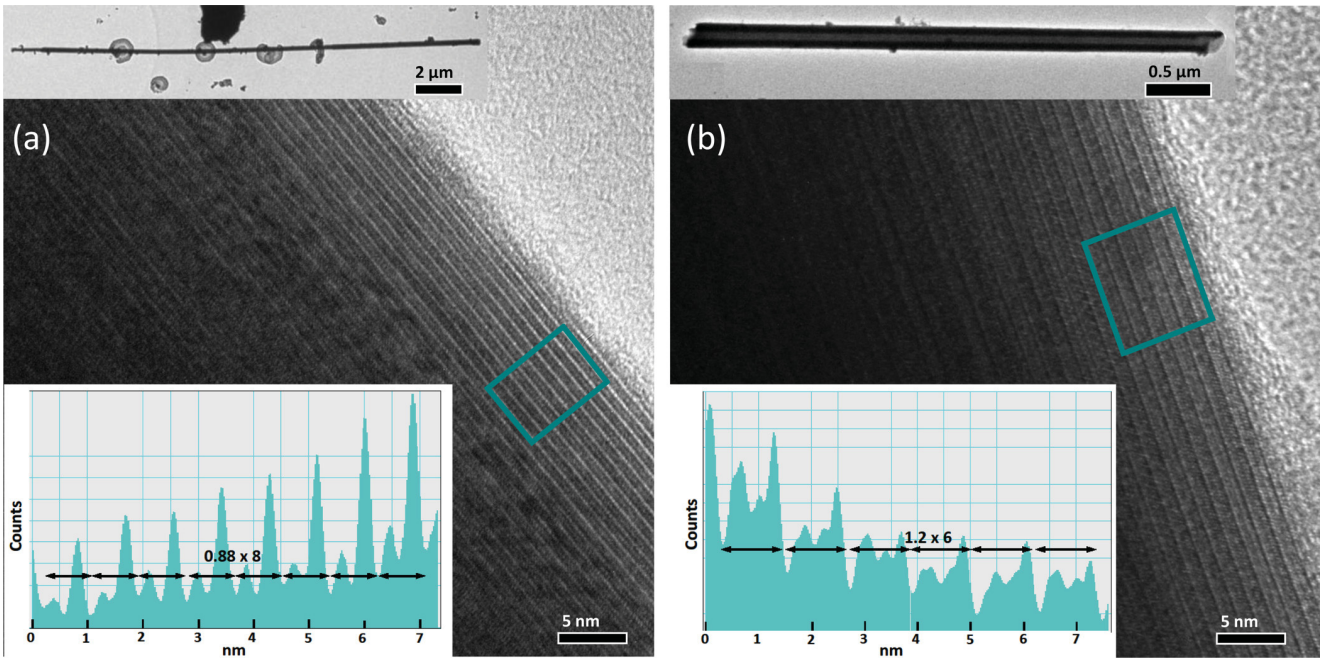

FIG. 2. Structural characterization of the nanotubes. (a) High and low (inset) TEM images of a Pb-NbS_2 nanotube investigated in this paper. The layer periodicity of 0.88 nm (alternating layers of Pb atoms and NbS_2) can be identified in a line profile (inset) of the nanotube area enclosed by the rectangle. (b) High and low (inset) TEM images of a $(PbS)_{1.14}NbS_2$ misfit layer nanotube investigated in this paper. The line profile (inset) taken from the area enclosed by the rectangle depicts the layer periodicity of 1.20 nm corresponding to alternating layers of PbS and NbS_2.

plane-wave basis and the projector-augmented wave (PAW) method, as implemented in the Quantum ESPRESSO (QE) package [35]. The Brillouin zone (BZ) was sampled using a $24 \times 24 \times 6$ Monkhorst-pack (MP) grid for NbS_2 and Pb-NbS_2, and a $3 \times 12 \times 3$ MP grid for $(PbS)_{1.14}NbS_2$. The cutoffs for plane-wave and charge-density expansion were set to 65 Ry and 650 Ry, respectively. Threshold for structural optimization was set to 2 (meV/Å)/atom in all three structures. Phonon frequencies were calculated using the linear-response (DFPT) technique, again within the QE package. To obtain the entire phonon dispersion in the case of NbS_2 and Pb-NbS_2, dynamical matrices were calculated on a $6 \times 6 \times 1$ MP grid in the BZ. Although the measurements were done on nanotubes, in the calculations a three-dimensional system, with the unit cells given in Fig. 1, was assumed. Since the studied nanotubes are $\gg$100 nm in diameter and the number of walls are well above ten in all cases studied, this is assumed to be a good approximation.

B. Results

Raman spectra of $2H$-NbS_2 were obtained by Nakashima *et al.* [36] thirty years ago. The two main Raman modes were observed at 379 cm^{-1} (A_{1g}) and 309 cm^{-1} (E^1_{2g}). In the regular $(PbS)_{1.14}NbS_2$ nanotubes, PbS and NbS_2 walls are alternating [4]. Coming from the bulk $2H$-NbS_2 D^4_{6h} structure, the symmetry of the NbS_2 part is at least reduced to the monolayer D_{3h} structure; additional distortion might occur due to charge transfer, covalent interlayer bonding, and nanotube curvature. However, in this paper, Raman mode assignments are based on the D_{3h} structure for simplicity. Due to the lack of a center of inversion, the bulk A_{1g} and B_{1u} modes reduce to A'_1 symmetry, and the E^1_{2g} and E_{1u} modes become in-plane E' modes. In backscattering geometry, the E'' mode (E_{1g} and E_{2u} in the bulk) is Raman forbidden. In total, the irreducible representations of the phonon modes in the symmetry group D_{3h} at the Γ point of the hexagonal Brillouin zone are $\Gamma = A'_1 + E'' + 2A''_2 + 2E'$.

From the bulk PbS structure, a two atoms thick part is cut out to form the PbS walls. They are significantly distorted compared to the NaCl type parent material with the lead atoms always protruding into the van der Waals gap. In contrast to the three-dimensional bonding network of bulk PbS, first-order Raman scattering becomes allowed [15].

Figure 3(a) shows Raman spectra of $(PbS)_{1.14}NbS_2$ nanotubes. Two regions can be singled out: below 200 cm^{-1} with Raman modes that have been attributed to the PbS layers in the literature [15,18,37] and above 340 cm^{-1}, where the two main peaks can be identified as the E' and A'_1 mode of the NbS_2 layer [15,38]. The A'_1 mode is situated at $\sim$378 cm^{-1} and thus only very weakly downshifted with respect to the A_{1g} mode of bulk NbS_2. A drastic change in Raman frequency on the other hand is observed for the E' mode that is upshifted by more than 40 wave numbers compared to the E_{2g} mode of bulk NbS_2 and lies at $\sim$353 cm^{-1}. The upshift is up to 12 wave numbers stronger than that found in bulk $(PbS)_{1.14}NbS_2$ [15,18,37,38]. Possible reasons for this rather unusual behavior, such as charge transfer from the MX to the TX_2 layer, strain effects, interlayer bonding, and the monolayer nature of the TX_2 part, will be discussed in detail in the next section. Typical full widths at half maximum (FWHMs) of the E' and A'_1 mode are 13 cm^{-1} and 15 cm^{-1}, respectively. Surprisingly, the relative intensities of the two

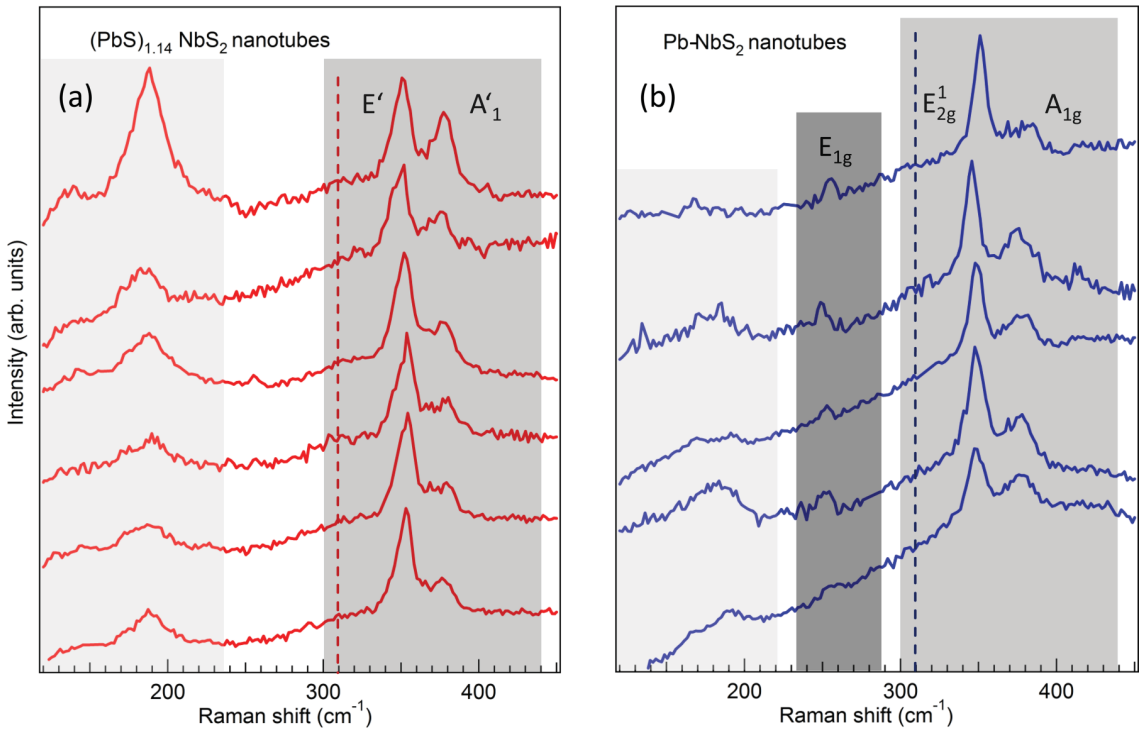

FIG. 3. (a) Raman spectra of all measured $(PbS)_{1.14}NbS_2$ nanotubes. The spectra of the different nanotubes have in common that they can be divided into two regions with modes associated with the PbS part below 200 cm^{-1} (light gray) and the main E' and A_1' Raman modes of the NbS_2 part between 300 and 400 cm^{-1} (darker gray). (b) Raman spectra of all measured Pb-NbS_2 nanotubes. Again, modes probably associated with the intercalant are found below 200 cm^{-1} and NbS_2 E_{2g}^1 and A_{1g} modes above 300 cm^{-1}. A Raman feature not seen in $(PbS)_{1.14}NbS_2$ nanotubes is the mode around 250 cm^{-1} (darkest gray). It is likely to be the E_{1g} mode of the NbS_2 part. Spectra depicted in (a) and (b) are taken with 532 nm excitation wavelength. They are normalized to the E mode around 350 cm^{-1} and offset for clarity. The solid lines represent the position of the E_{2g}^1 mode in the pristine $2H$-NbS_2 material (309 cm^{-1}) [36].

modes are different from the ones previously observed for the bulk MLC. For the nanotubes investigated in this paper the intensity ratio E'/A_1' has values close to 2.5, whereas for the bulk structures the ratio is almost reversed [15]. However, in the literature, the Raman spectra are recorded with 488 nm or 514 nm excitation wavelength [15,37] in contrast to the 532 nm laser light used here. In both the parent $2H$-NbS_2 material and the bulk $(PbS)_{1.14}NbS_2$ compound, strong two-phonon bands are identified [15,36] that are apparently absent in the misfit layer nanotubes. Between 100 and 200 cm^{-1} three modes can be distinguished in most of the Raman spectra (see Fig. 3); a rather strong peak at 187 cm^{-1} with a shoulder at 170 cm^{-1} and a weak broad feature around 140 cm^{-1}. The latter is close to the cutoff of the notch filter and thus possibly reduced in intensity.

The Raman spectra of Pb-NbS_2 nanotubes are shown in Fig. 3(b). They can be easily related to the spectra of $(PbS)_{1.14}NbS_2$ nanotubes described above. There are, however, subtle differences between the two cases. Even though the original structure of the $2H$-NbS_2 parent material is changed both by the intercalated Pb atoms and the resulting stacking arrangement, the high D_{6h}^4 symmetry is retained. The vibrational modes of the material as a whole can thus be decomposed into the following irreducible representations at the Γ point of the Brillouin zone: $\Gamma = A_{1g} + 2A_{2u} + 2B_{2g} + B_{1u} + E_{1g} + 2E_{1u} + 2E_{2g} + E_{2u}$.

Two of the four Raman active modes can be easily identified in the measured Raman spectra. The A_{1g} mode is broadened compared to the closely related A_1' mode in $(PbS)_{1.14}NbS_2$ (∼378 cm^{-1}) and slightly downshifted to ∼377 cm^{-1}; the E_{2g}^1 mode is always located at lower Raman frequencies than the corresponding E' mode in the $(PbS)_{1.14}NbS_2$ nanotubes (∼353 cm^{-1}), namely at ∼348 cm^{-1}. The relative intensities are $E_{2g}^1/A_{1g} = 1.5$ in average. In the lower-wave-number region, weak Raman features appear at almost the same frequency as in the misfit compound, namely at ∼187 and 169 cm^{-1}. In comparison with the Raman spectra of $(PbS)_{1.14}NbS_2$, the peak at 169 cm^{-1}, which is only seen as a shoulder of a stronger peak in $(PbS)_{1.14}NbS_2$, is of higher relative intensity in Pb-NbS_2. Most importantly, a feature that allows for the easy identification of NbS_2 nanotubes with intercalated lead atoms is the appearance of a new Raman feature at around 253 cm^{-1} that is not observed in the spectra of the $(PbS)_{1.14}NbS_2$ nanotubes.

II. DISCUSSION

A. Raman modes between 100 and 200 cm^{-1}

It is commonly accepted in the literature on misfit layer compounds that the Raman spectra can be divided into a higher-frequency part with Raman modes belonging to the host material and a lower-lying part with Raman modes of the intercalant. Whereas the NbS_2 modes in the Raman spectra of $(PbS)_{1.14}NbS_2$ and Pb-NbS_2 can be easily identified by

comparison with the bulk parent material, this cannot be said about the MX part of the structure. First-order Raman scattering is not allowed for the original three-dimensional bulk PbS structure but becomes possible in the distorted double-layer structure of PbS in $(PbS)_{1.14}NbS_2$. In principle, three sources for the Raman features between 100 and 200 cm^{-1} are conceivable in the MLC: (i) phonons stemming from the PbS part of the MLC, (ii) second-order modes and two-phonon density of states, or (iii) defect, disorder-induced modes.

(i) The main peak at 189 cm^{-1} in the Raman spectra of the MLC nanotubes is observed in the Raman spectra of the bulk MLC as well [15,18,37] and has been identified as one of two PbS modes of A type symmetry. By comparison with a work by Kisoda *et al.* [17] on misfit layer compounds of $2H$-TaS_2 it is likely to be the symmetric layer breathing mode of PbS; the frequency of the other A type mode of PbS was reported to be around 80 cm^{-1} [15], too low-lying to be observed in this paper. As a rather surprising result, the mode at 189 cm^{-1} that could be related to PbS still occurs in the spectra of Pb-NbS_2 nanotubes (albeit with only weak Raman intensity), despite the assumption that no lead sulfide layers are present in the structure. This raises the question whether there are "pockets" of PbS still present in the structure of the Pb-NbS_2 nanotubes that result in PbS modes depending on the local environment. This would also explain the different intensities observed for different Pb-NbS_2 nanotubes. Another idea would be that a nearly covalent bonding of Pb atoms to the neighboring NbS_2 layers could give rise to a PbS-like phonon density of states.

(ii) The peak at 189 cm^{-1} is rather broad, which is unusual for a first order Raman mode but typical for a two-phonon band. Very broad two-phonon bands appear in the spectra of bulk $2H$-NbS_2 at higher wave numbers between 200–300 cm^{-1} [36] and are unlikely to be accountable for the features just below 200 cm^{-1} in the MLC. It seems possible that second order modes of the intercalant appear in the spectra of the MLC as well as in Pb-NbS_2. The phonon dispersion of Pb-NbS_2 is shown in Fig. 4(b); for comparison the phonon dispersion of the parent $2H$-NbS_2 is depicted in Fig. 4(a). At the Γ point one can see the two first order Pb-NbS_2 modes at 364 and 388 cm^{-1}, but there are also lower-lying modes at 66, 98, and 103 cm^{-1}. The atomic displacement patterns (not shown) reveal for the second of these modes that the Pb atoms and NbS_2 vibrate against each other as rigid layers; for the third mode NbS_2 layers perform breathinglike motions while the Pb layer is not vibrating. Second-order scattering of both of these modes could in principle be responsible for the Raman features seen at 189 and 170 cm^{-1} in Pb-NbS_2. The question then arises if similar patterns would be observable in the misfit layer compound with the PbS layer playing the role of the intercalant atoms in Pb-NbS_2.

(iii) Raman spectra of the $3R$-NbS_2 polytype exhibit a broad phonon band centered around 160 cm^{-1} [36,39]. McMullan *et al.* [39] attribute it to an impurity or defect mode possibly resulting from the expected nonstoichiometry of $3R$-NbS_2 with some extra Nb atoms located in the van der Waals gap [40]. One might argue that the situation here is similar. Both $3R$-NbS_2 and Pb-NbS_2 as well as the misfit layer compound have different stacking orders compared to $2H$-NbS_2, and all three of the compounds exhibit a strong upshift of the E^1_{2g} mode compared to $2H$-NbS_2. As we will discuss later, there is strong likelihood of metal cross substitution in the misfit layer compound [12]. The exchange of Pb atoms in the PbS layer with Nb atoms of the NbS_2 layer and vice versa could indeed lead to an impurity-induced Raman mode in the spectra of the $(PbS)_{1.14}NbS_2$ nanotubes. The feature at around 140 cm^{-1}

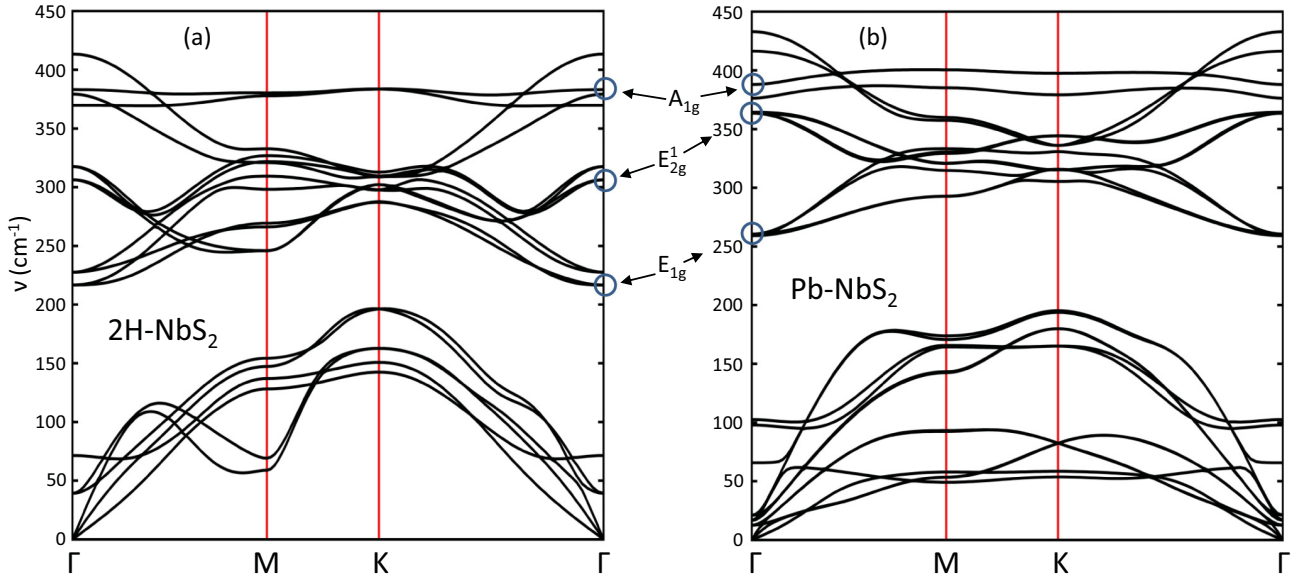

FIG. 4. (a) Phonon dispersion of the parent $2H$-NbS_2 bulk material. Above 200 cm^{-1} at the Γ point, three first order Raman modes, the E_{1g}, E^1_{2g}, and A_{1g} mode, are marked with blue circles and their calculated frequencies are listed in Table I. (b) The main features of the dispersion are reproduced in the dispersion of lead intercalated NbS_2. The three main Γ-point Raman modes are seen above 250 cm^{-1}, with the two E type modes considerably upshifted compared to their frequency in NbS_2. The frequency of the A_{1g} mode, on the other hand, stays nearly the same. Modes with contributions from the intercalant lead atoms are found around 100 cm^{-1}.

in the $(PbS)_{1.14}NbS_2$ nanotubes has not been conclusively attributed in the literature [37]. A feature observed at 165 cm^{-1} in the misfit layer compound $(LaS)_{1.2}NbS_2$ [16] is ascribed to a mode induced by the interaction of the two components; that is, the modulation along the a axis in the LaS layer. The fact that the 140 cm^{-1} mode has no significant intensity in Pb-NbS_2 indeed is evidence of this mode being a Raman mode inherent to the misfit compound.

B. Raman modes belonging to NbS_2 in the $(PbS)_{1.14}NbS_2$ and Pb-NbS_2 nanotubes

Both NbS_2 and PbS Raman modes are observed in the spectra of the misfit layer nanotubes. In particular, the character of the two prominent NbS_2 modes is preserved as has been shown by polarization dependent Raman measurements on bulk $(PbS)_{1.14}NbS_2$ and other similar compounds [16,37]. Hence, the Raman spectra can be considered as a superposition of contributions from their constituents. In the investigated wave-number region, no new Raman modes were observed that would point to structural changes or significant electronic interaction between the layers of the two materials. Neither did we observe Raman bands that could be assigned to Raman inactive modes or phonons in violation of the $q = 0$ selection rule. Despite this apparent independence of the alternation of layers, some modes are found to be considerably shifted in frequency from those of the pristine crystals. Most prominently, the E'/E^1_{2g} mode of the NbS_2 material is upshifted by more than 40 wave numbers to 353 and 348 cm^{-1} in $(PbS)_{1.14}NbS_2$ and Pb-NbS_2 nanotubes, respectively. Possible strain effects would be expected to be much smaller. The cell parameter of the NbS_2 part in the commensurate b direction is slightly increased in the MLC with respect to 2H-NbS_2 to match the cell parameter of the PbS part [32]. In fact, a softening of Raman frequencies from the resulting tensile strain would be expected, opposite to what is observed here.

In Fig. 5(a) the region of the in-plane E mode and the out-of-plane A mode is shown for exemplary nanotubes of both types. Again, the A'_1/A_{1g} mode is rather broad and has similar frequency in the two compounds, whereas the E'/E^1_{2g} is of smaller FWHM especially in the Pb-NbS_2 nanotubes. While the E mode is shifted drastically with respect to the 2H-NbS_2 parent compound (309 cm^{-1}), the shift is a few wave numbers smaller in Pb-NbS_2 than in $(PbS)_{1.14}NbS_2$. Although there is some spreading in the absolute frequencies of the E and A modes, the frequency difference between the two modes is always bigger in Pb-NbS_2 than in $(PbS)_{1.14}NbS_2$, as is shown in Fig. 5(b). Hence the two types of nanotubes investigated in this study can be easily distinguished. We have calculated the frequencies of the first order Raman modes of bulk 2H-NbS_2, Pb-NbS_2, and $(PbS)_{1.14}NbS_2$ as detailed in the experiment section and present them in Table I. The calculated frequencies of 2H-NbS_2 are in excellent agreement with the experimentally obtained frequencies taken from Ref. [36]. The calculated E_{1g} NbS_2 mode is not reported in Ref. [36] because it is forbidden in the employed backscattering configuration. Employing the same method to the Pb-NbS_2 and $(PbS)_{1.14}NbS_2$ bulk compounds, we find a good agreement between measured and calculated frequencies. The calculations confirm the strong upshift of the E^1_{2g}/E' in Pb-NbS_2 and $(PbS)_{1.14}NbS_2$ as compared to the 2H-NbS_2 parent material and the only small changes in the A_{1g}/A'_1 frequency. The calculations on the misfit compound reveal a splitting of the mentioned modes into several components which could account for the experimentally observed broadening of the modes with respect to the parent material. For the misfit compound we can also see that the calculations are in excellent agreement with bulk literature values. However, even though

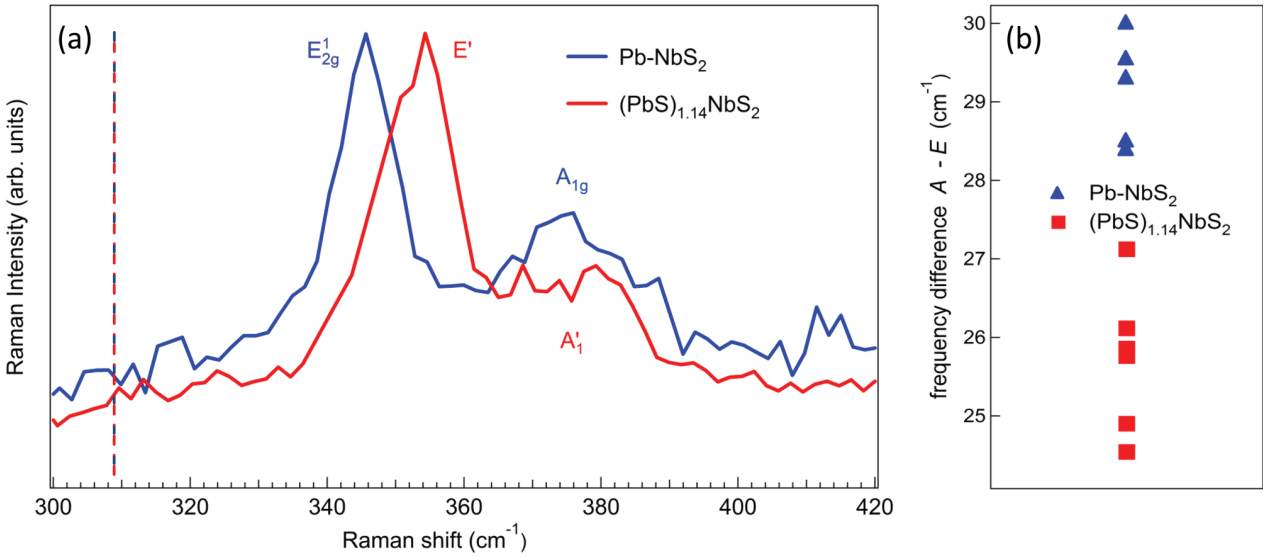

FIG. 5. (a) Raman features in the region between 300 and 420 cm^{-1} of exemplary Pb-NbS_2 and $(PbS)_{1.14}NbS_2$ nanotubes. The most prominent intralayer NbS_2 modes in the investigated compounds are shown with the in-plane E' of $(PbS)_{1.14}NbS_2$ (red line) always at slightly higher frequencies than the E^1_{2g} mode of Pb-NbS_2 (blue line). Again, the dashed line represents the position of the E^1_{2g} mode in the pristine 2H-NbS_2 material (see Fig. 3) [36]. In contrast, the A'_1 mode of $(PbS)_{1.14}NbS_2$ is found at nearly the same frequency as the A_{1g} mode in Pb-NbS_2. (b) The frequency difference between the above described modes clearly distinguishes the two types of nanotubes, with $\omega(A\text{-}E)$ between 24–27 cm^{-1} for all of the measured $(PbS)_{1.14}NbS_2$ nanotubes and 28–30 cm^{-1} for all of the Pb-NbS_2 nanotubes.

TABLE I. Calculated and experimentally obtained Raman frequencies (in cm^{-1}) of the bulk $2H$-NbS_2 structure, the lead intercalated NbS_2 material, and the misfit layer $(PbS)_{1.14}NbS_2$ compound. Where available, literature bulk values are added. The in-plane E modes shift up in frequency from the parent material to Pb-NbS_2 and $(PbS)_{1.14}NbS_2$, whereas the out-of-plane A mode remains almost constant.

D^4_{6h} symm.	2H-NbS_2 bulk calc.	2H-NbS_2 bulk exp. [36]	Pb-NbS_2 bulk calc.	Pb-NbS_2 NT exp.	D_{3h} symm.	$(PbS)_{1.14}NbS_2$ bulk calc.	$(PbS)_{1.14}NbS_2$ bulk exp. [37]	$(PbS)_{1.14}NbS_2$ NT exp.
E_{1g}	217		260	253	E''	237, 241		
E^1_{2g}	306	309	364	348	E'	333-340	342	353
A_{1g}	383	380	388	377	A'_1	372-379	375	378

the nanotubes investigated in this paper are hundreds of nanometers in diameter, have a large number of walls, and thus can be considered as bulklike, the measured Raman frequencies in the nanotube deviate somewhat from the bulk values. This is even more so for the intercalated Pb-NbS_2 nanotubes. There is no literature on the Raman spectrum of the Pb-NbS_2 bulk, but bulk calculations and measured nanotube frequencies differ more strongly than in the calculated and measured MLCs. The calculations also show that the E^1_{2g}/E' mode is not the only mode exhibiting an upshift but that similar frequency shifts can be expected for the E_{1g} mode of $2H$-NbS_2 in the intercalated and the misfit compounds. This is in disagreement with Ref. [39], where the authors identify a Raman feature in $2H$-NbS_2 around 260 cm^{-1} as the E_{1g} mode, although they describe their assignment as somewhat tentative as it deviates strongly from their calculated $2H$-NbS_2 phonon frequencies. On the other hand, the Raman mode observed at 258 cm^{-1} in the stage-2 MLC $(LaS)_{0.6}NbS_2$ [16] perfectly fits the picture presented here, as it is also likely to stem from an upshifted $2H$-NbS_2 E_{1g} phonon mode.

Most of the works dealing with Raman spectroscopy on intercalated transition metal dichalcogenides or misfit layer compounds commonly agree that the drastic frequency shifts originate from charge transfer (CT) from the intercalated layer to the TX_2 layer [15,17,18,37]. The MX layer acts as the donor part of the structure, donating electrons to the half-filled d_{z^2} conduction band orbital (one electron per T atom) of the trigonal prismatic TX_2 layer (T = Nb, Ta). Apart from the band filling and resulting shift of the Fermi level to higher energies, following the rigid band model, the electronic band structure closely resembles the superposition of the band structure of the constituent materials. However, no final conclusion has been reached as to why only certain Raman modes are affected strongly by the CT whereas other Raman modes are barely influenced. Pereira *et al.* [41] note that the lobes of the d_{z^2} orbital are oriented in the z direction, perpendicular to the layers. As the atomic displacement vectors for the E-type phonons are in the layer plane, there will be changes in the overlap of the sulfur valence orbitals with the d_{z^2} orbital of the T atom. Therefore, the CT will have a bigger influence on the Raman frequency than for the A'_1 mode, where sulfur atoms from the TX_2 layer move along z. Another way to investigate the consequences of the band filling by the charge transfer is to look at the changes of the intralayer central and noncentral forces. While the former are increased as a result of the CT, the latter angle bending force constants are decreased, affecting the E-type modes in particular [42]. Looking at the magnitude of the charge transfer one has to differentiate between compounds where the TX_2 layer is not stable in itself and only exists in MLCs because it is stabilized by the charge transfer (for instance LaS-CrS_2 [25]), compounds with a stable TX_2 layer and R = La, Ce, Gd (rare earth metals, which are often trivalent in the RX layer of the MLCs) and compounds with a stable TX_2 layer and M = Sn, Pb (post-transition metals that take a divalent state in MX). In the first two cases, a charge transfer mechanism seems well established both experimentally and theoretically, and its magnitude is of considerable strength with up to 0.9 electrons being donated to the d_{z^2} orbital [43–46]. In the case we are dealing with here, however, the charge transfer appears to be weaker. Using a variety of experimental and theoretical methods, a charge transfer of up to 0.4 electrons/Nb atom is reported by a number of authors [18,47,48], while others find no evidence or are in doubt whether there is charge transfer at all [49,50]. This is in agreement with our calculations, which show no sign of charge transfer but, as detailed above, yield Raman frequencies in excellent agreement with literature values. Nonetheless, assuming that charge transfer is responsible for the strong upshift of the E' mode in $(PbS)_{1.14}NbS_2$, the magnitude of this shift should be in some way related to the amount of charge transfer. Indeed, Hangyo *et al.* [38] find that the upshift is stronger by some 20 cm^{-1} for RS-NbS_2 (R = La, Ce) than for MS-NbS_2 (M = Sn, Pb). Furthermore, they substantiate their argument by looking at the Raman spectra of stage-1 and stage-2 compounds, where the MX layer is inserted every TX_2 layer and every second TX_2 layer, respectively. The weaker frequency shift in the stage-2 compounds is attributed to only half the charge being transferred to the NbS_2 layer in the stage-2 compounds as there are only half as many MX layers [37]. Following this picture, the charge transfer should be expected to be of similar strength for both the investigated materials in the present work or even a little weaker for Pb-NbS_2 than for $(PbS)_{1.14}NbS_2$, as evidenced by the slightly smaller frequency shift in the Raman spectra of the former compound. However, Eppinga *et al.* [51] as well as Dijkstra *et al.* [52] made a convincing case that the transferred charge for compounds, where post-transition metal atoms are intercalated between dichalcogenide layers (such as in Pb-NbS_2), is one electron per post-transition metal atom. The NbS_2 d_{z^2} band is then completely filled, and one can instead expect metallic conduction of the remaining electrons in the intercalated layer. Photoelectron spectra of the valence bands as well as the Nb ($3d$) core levels exhibit shifts and increased band filling with respect to the host material spectra, which clearly indicates that charge transfer takes place. The transfer of one electron per Pb atom leads to an "unusual

(formal) valency" of Pb^{+}, but there is evidence that a rapid valency fluctuation between Pb^{0} and Pb^{2+} can account for this average valency [53]. Our QE calculations on the other hand, similarly to the calculations on the misfit compound, show little to no charge transfer from the intercalated atoms to the transition metal dichalcogenide layer.

In summary, the charge transfer process is very important for misfit compounds with rare earth metal chalcogenide layers RX, and there is experimental evidence that it is important for Pb-NbS_2 as well, although this is not supported by our calculations. The same, however, can not be said about $(PbS)_{1.14}NbS_2$ and other MX-TX_2 misfit compounds, where experimental and theoretical evidence points to little to no charge transfer at all. This means that charge transfer alone can not sufficiently explain the strong upshift of the E modes in misfit layer compounds. For $(PbS)_{1.14}NbS_2$ and Pb-NbS_2 more specifically, the amount of suspected charge transfer does not correlate with the magnitude of the Raman frequency upshifts, furthermore rendering improbable the charge transfer mechanism as a way to explain the observed shifts.

Nonetheless, it is the change of interlayer interaction from the pristine to the misfit layer compounds that is not only the key to an understanding of the remarkable stability of MLCs [12] but will also define their vibrational properties. Some of these interlayer interaction mechanisms shall be discussed here.

(i) Among the different possible bonding mechanisms between neighboring MLC layers, Kalläne *et al.* [12] find experimental evidence from photoemission microspectroscopy on the core levels of the system $(PbS)_{1.13}TaS_2$ of metal cross substitution of Ta atoms into the PbS layer and Pb atoms into the TaS_2 layer, thus charging the planes and binding them together via Coulomb interaction. They argue that stoichiometry is not a necessary condition for the stabilization of the MLCs. In contrast, in a more recent paper that references the work by Kalänne *et al.*, Kabliman *et al.* [14] use *ab initio* DFT calculations to compare the metal cross substitution mechanism for stoichiometric and nonstoichiometric $(PbS)_{1.14}TaS_2$. The obtained formation energies clearly favor nonstoichiometry and indicate that stoichiometric metal cross substitution cannot stabilize the investigated MLCs. A minimum in the formation energy is reached for an impurity concentration of $n_{\mathrm{Ta_{imp}}} = 0.15$ in the PbS layer. To sustain overall neutrality the substitution of cationic sites within the MX layer by Nb 3^{+} atoms must be balanced by an equal amount of reduced trivalent Nb atoms in the NbS_2 layer. As a result, neighboring layers are electrostatically bound with an interlayer interaction that might be called "cationic coupling" [54]. As a result of this redistribution of charge there is an increase in the electronic population in the NbS_2 layers able to further fill the Nb d_{z^2} band without actually transferring charge from PbS to NbS_2. This could explain the shifts seen in optical reflection spectra and photoelectron spectra without using the concept of charge transfer. Moëlo *et al.* [54] find a substitution of up to 12%, which makes the MLC compound a $(Pb_{0.991}Nb_{0.126}S_{1.136})NbS_2$. This pseudo charge transfer, however, is also unlikely to be responsible for the frequency upshift of the E mode. Our calculations on Pb-NbS_2 and $(PbS)_{1.14}NbS_2$ reproduce the experimentally observed shift and are intrinsically performed on the pure stoichiometric compound. Assuming that the reason is the same in both of the investigated compounds, it can thus be concluded that the reason for the upshift has to be found somewhere else.

(ii) Another mechanism that comes into play as soon as the PbS and the NbS_2 layer are combined and could play a role in stabilizing the MLCs is the coordinative interlayer bonding. The Pb atoms in the PbS layers possess a lone pair of electrons in an orbital that extends in the interlayer van der Waals gap. This enables the Pb atoms to covalently bond to one or two S atoms in the -2 oxidation state of the neighboring NbS_2 layer depending on their relative position along the incommensurate a axis [8]. In fact, it is observed that the Pb atoms in $(PbS)_{1.14}NbS_2$ always protrude into the van der Waals gap [55] in between layers and that interlayer Pb-S distances from Pb atoms in the PbS layer to S atoms in the NbS_2 layer are well within range of normal PbS intralayer bond lengths [56]. Based on the 0.88 nm periodicity observed in Pb-NbS_2 [4], the interlayer Pb-S distance is even shorter than a normal intralayer PbS bond length in the case of the intercalated NbS_2 nanotubes. However, to the best of our knowledge there has been no direct proof of covalent interlayer bonding so far. This idea has only been surfaced in the absence of another mechanism that could explain the stability of misfit layer compounds [10,49] or from theoretical considerations [47]. In addition, it is doubtful that covalent bonds would have a larger influence on the E modes than on the A mode. Instead, one would assume that the out-of-plane movement of sulfur atoms in the latter is more strongly affected than the in-plane movement of the E modes.

(iii) In the context of discussing possible reasons for the upshift of the E modes in intercalated and the MLC compound, it is also interesting to look at other related compounds where frequency shifts occur. In $3R$-NbS_2, for instance, two E modes are seen upshifted considerably compared to $2H$-NbS_2 [39,57]; again the A mode is barely shifted. We have calculated the Raman frequencies of pristine $3R$-NbS_2 and found close to no difference between the Raman frequencies in $2H$- and $3R$-NbS_2. We can thus conclude that the layer stacking order in NbS_2 does not affect the frequency of the phonon modes, contrary to the assumption made in Ref. [36] for explaining the experimentally obtained Raman frequencies in $3R$-NbS_2. Instead, we think that $3R$-NbS_2 is indeed normally nonstoichiometric [40,58] with extra Nb atoms occupying octahedral sites in between the layers. These excess Nb atoms add an additional interlayer force to the weak van der Waals interaction and could be responsible for the observed upshift. As there are only a few of them, the frequency of the in-plane mode highly depends on the local composition and is therefore rather broad. An upshift is seen for Fe_xNbS_2 as well [59] and can be explained along similar lines.

(iv) A yet unexplored way to account for the frequency shift of the in-plane modes in particular combines the charge transfer mechanism with an ionic interlayer coupling. Even in semiconducting intercalant layers like PbS, a non-negligible amount of charge transfer will leave some empty states that enable metallic conduction. Because of the layered nature of the intercalants, this conduction will primarily take place in the a-b plane. In the context of the rigid band model that explains the properties of the MLC as a combination of the properties

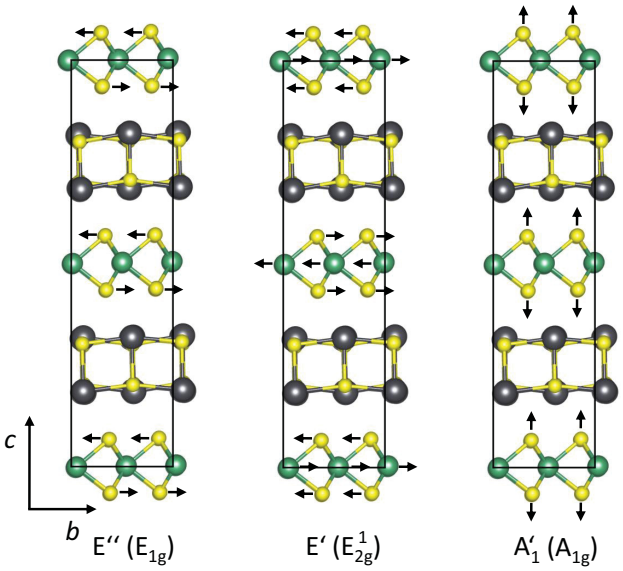

FIG. 6. Atomic displacement patterns of the three main Raman modes in $(PbS)_{1.14}NbS_2$ discussed in the text and listed in Table I. They are derived from the $2H$-NbS_2 E_{1g}, E^1_{2g}, and A_{1g} modes (in brackets) and have E'', E', and A'_1 symmetry, respectively, in the $(PbS)_{1.14}NbS_2$ misfit layer material.

of the two constituents, for the first-order Raman modes of the NbS_2 layer, the atoms in the intercalant layer (here Pb or PbS) do not move (see Fig. 6). With the displacement of atoms in the NbS_2 layer, the charge at the sulfur atoms is moving in-plane for the E modes. As a result, in the neighboring intercalant layer, there will be some in-plane electron charge redistribution. In order to regain minimal energy, this longitudinal charge redistribution will be followed by a restoring force acting on the phonon modes, hence lead to a stiffening of the phonon frequency compared to the parent compound. For the out-of-plane A mode (see Fig. 6), on the other hand, the movement of sulfur atoms will not have the same effect, as charge inside the intercalant layer will not be redistributed significantly along the stacking c direction. The A mode is thus unaffected or even exhibits a slight downshift due to the lack of interlayer interaction with a neighboring NbS_2 layer, much like the redshift seen in few-layer transition metal dichalcogenides compared to the bulk material [60,61]. This charge redistribution model represents a new take on the hitherto unexplained phenomenon of drastic frequency upshifts of Raman modes in intercalated and misfit materials with respect to the respective Raman modes in the transition metal dichalcogenide parent compounds. However, elaborate work is still needed to further support this model and to gain more insight into the reasons for the experimentally observed Raman shifts.

III. CONCLUSION

We have taken Raman measurements of a number of misfit layer $(PbS)_{1.14}NbS_2$ as well as of Pb-NbS_2 nanotubes. Their Raman spectra have in common that they can be interpreted in terms of a superposition of Raman modes of the constituents: First order Raman modes of the transition metal dichalcogenide are found above 250 cm^{-1}, and Raman modes of the intercalant and second order modes of NbS_2 are situated below 200 cm^{-1}. We have calculated the phonon dispersions of the lead intercalated NbS_2 bulk material and the pristine $2H$-NbS_2 as well as the Γ-point phonons of the misfit layer compound to help us attribute the measured Raman modes. Most strikingly, the E^1_{2g}/E' mode of Pb-NbS_2 and $(PbS)_{1.14}NbS_2$, respectively, is shifted up in frequency by more than 30 wave numbers compared to the parent material. The calculations reveal that a similar upshift for the E_{1g}/E'' mode exists. Although this mode is forbidden in the employed backscattering geometry, it can be detected as a peculiarity in the spectra of the Pb-NbS_2 nanotubes. In contrast to the in-plane E type modes, the frequency of the out-of-plane A_{1g}/A'_1 mode in the intercalated and misfit nanotubes stays almost the same as in the parent compound. There are small differences in the magnitude of the measured E^1_{2g}/E' Raman mode upshifts in Pb-NbS_2 and $(PbS)_{1.14}NbS_2$ nanotubes that are used as a starting point for a discussion about the underlying mechanisms for the drastic frequency shifts. We find evidence contradicting the charge transfer model that is brought forward by most of the literature discussing Raman spectra of misfit layer materials in the past. Other interlayer bonding mechanisms such as metal cross substitution and coordinative interlayer bonding are presented and discussed regarding their likelihood of being responsible for the frequency upshifts. We introduce a charge redistribution model that could account for the phenomenon but has yet to be put on solid theoretical ground. Our results will guide future investigations of interlayer interlayer bonding mechanisms in intercalated and misfit layer transition metal dichalcogenides.

ACKNOWLEDGMENTS

We acknowledge financial support of the German-Israeli Foundation (research Grant No. I-1233-302.5/2014) and the European Commission for the Marie S. Curie International Training Network MoWSeS (GA 317451).

[1] R. Tenne and G. Seifert, Annu. Rev. Mater. Res. **39**, 387 (2009).
[2] G. Radovsky, R. Popovitz-Biro, M. Staiger, K. Gartsman, C. Thomsen, T. Lorenz, G. Seifert, and R. Tenne, Angew. Chem. Int. Ed. **50**, 12316 (2011).
[3] G. Radovsky, R. Popovitz-Biro, and R. Tenne, Chem. Mater. **24**, 3004 (2012).
[4] G. Radovsky, R. Popovitz-Biro, D. Stroppa, L. Houben, and R. Tenne, Accts. Chem. Res. **47**, 406 (2014).
[5] J. Rouxel, A. Meerschaut, and G. A. Wiegers, J. Alloys Compd. **229**, 144 (1995).
[6] A. Meerschaut, R. Roesky, A. Lafond, C. Deudon, and J. Rouxel, J. Alloys Compd. **219**, 157 (1995).

[7] G. Wiegers and A. Meerschaut, Mater. Sci. Forum **100-101**, 101 (1992).
[8] G. Wiegers, Prog. Solid St. Chem. **24**, 1 (1996).
[9] J. Brandt, L. Kipp, M. Skibowski, E. E. Krasovskii, W. Schattke, E. Spiecker, C. Dieker, and W. Jäger, Surf. Sci. **532-535**, 705 (2003).
[10] A. R. H. F. Ettema, C. Haas, and T. S. Turner, Phys. Rev. B **47**, 12794 (1993).
[11] A. Meerschaut, Y. Moëlo, L. Cario, A. Lafond, and C. Deudon, Mol. Cryst. Liq. Cryst. Sci. Technol., Sect. A **341**, 1 (2000).
[12] M. Kalläne, K. Rossnagel, M. Marczynski-Bühlow, L. Kipp, H. I. Starnberg, and S. E. Stoltz, Phys. Rev. Lett. **100**, 065502 (2008).
[13] C. Deudon, A. Lafond, O. Leynaud, Y. Moëlo, and A. Meerschaut, J. Solid State Chem. **155**, 1 (2000).
[14] E. Kabliman, P. Blaha, and K. Schwarz, Phys. Rev. B **82**, 125308 (2010).
[15] M. Hangyo, S. Nakashima, Y. Hamada, T. Nishio, and Y. Ohno, Phys. Rev. B **48**, 11291 (1993).
[16] M. Hangyo, K. Kisoda, T. Nishio, S. Nakashima, T. Terashima, and N. Kojima, Phys. Rev. B **50**, 12033 (1994).
[17] K. Kisoda, M. Hangyo, S. Nakashima, K. Suzuki, T. Enoki, and Y. Ohno, J. Phys.: Condens. Matter **7**, 5383 (1995).
[18] K. Kisoda, M. Hangyo, J. Kuroda, H. Harima, and S. Nakashima, Sol. St. Comm. **103**, 597 (1997).
[19] C. Sourisseau, R. Cavagnat, and J. L. Tirado, J. Raman Spectrosc. **23**, 647 (1992).
[20] Q. Lin, C. L. Heideman, N. Nguyen, P. Zschack, C. Chiritescu, D. G. Cahill, and D. C. Johnson, Eur. J. Inorg. Chem. **2008**, 2382 (2008).
[21] P. Jood, M. Ohta, H. Nishiate, A. Yamamoto, O. I. Lebedev, D. Berthebaud, K. Suekuni, and M. Kunii, Chem. Mater. **26**, 2684 (2014).
[22] P. Jood, M. Ohta, O. I. Lebedev, and D. Berthebaud, Chem. Mater. **27**, 7719 (2015).
[23] D. R. Merrill, D. B. Moore, S. R. Bauers, M. Falmbigl, and D. C. Johnson, Materials **8**, 2000 (2015).
[24] D. Reefman, J. Bank, H. B. Brom, and G. A. Wiegers, Solid State Commun. **75**, 47 (1990).
[25] L. Panchakarla, R. Popovitz-Biro, L. Houben, R. Dunin-Borkowski, and R. Tenne, Angew. Chem. Int. Ed. **53**, 6920 (2014).
[26] G. Radovsky, R. Popovitz-Biro, and R. Tenne, Chem. Mater. **26**, 3757 (2014).
[27] G. Radovsky, R. Popovitz-Biro, T. Lorenz, J.-O. Oswig, G. Seifert, L. Houben, R. E. Dunin-Borkowski, and R. Tenne, J. Mater. Chem. C **4**, 89 (2016).
[28] T. Lorenz, J.-O. Oswig, and G. Seifert, Beilstein J. Nanotechnol. **5**, 2171 (2014).
[29] F. Qin, W. Shi, T. Ideue, M. Yoshida, A. Zak, R. Tenne, T. Kikitsu, D. Inoue, D. Hashizume, and Y. Iwasa (unpublished).
[30] O. Madelung, *Semiconductors: Data Handbook*, 3rd ed. (Springer, Berlin, Heidelberg, 2004).
[31] A. Kuc, N. Zibouche, and T. Heine, Phys. Rev. B **83**, 245213 (2011).
[32] D. Bernaerts, S. Amelinckx, G. V. Tendeloo, and J. V. Landuyt, J. Cryst. Growth **172**, 433 (1997).
[33] R. Eppinga and G. Wiegers, Mat. Res. Bull. **12**, 1057 (1977).
[34] G. Radovsky, R. Popovitz-Biro, D. Stroppa, L. Houben, and R. Tenne, Accts. Chem. Res. (2014), see supporting information in Ref. 4.
[35] P. Giannozzi, S. Baroni, N. Bonini, M. Calandra, R. Car *et al.*, J. Phys.: Condens. Matter **21**, 395502 (2009).
[36] S. Nakashima, Y. Tokuda, and A. Mitsuishi, Sol. Stat. Commun. **42**, 601 (1982).
[37] M. Hangyo, K. Kisoda, S. Nakashima, A. Meerschaut, and J. Rouxel, Physica B **219–220**, 481 (1996).
[38] M. Hangyo, T. Nishio, S. Nakashima, Y. Ohno, T. Terashima, and N. Kojima, Jpn. J. Appl. Phys. Suppl. **32**, 581 (1993).
[39] W. McMullan and J. Irwin, Sol. Stat. Commun. **45**, 557 (1983).
[40] M. Fisher and M. Sienko, Inorg. Chem. **19**, 39 (1980).
[41] C. Pereira and W. Liang, J. Phys. C: Solid State Phys. **18**, 6075 (1985).
[42] K. Shirai, K. Kisoda, M. Hangyo, and S. Nakashima, Sol. St. Comm. **103**, 131 (1997).
[43] A. R. H. F. Ettema, S. van Smaalen, C. Haas, and T. S. Turner, Phys. Rev. B **49**, 10585 (1994).
[44] C. Rüscher, C. Haas, S. van Smaalen, and G. Wiegers, J. Phys.: Condens. Matter **6**, 2117 (1994).
[45] Y. Ohno, Phys. Rev. B **48**, 5515 (1993).
[46] C. M. Fang, S. van Smaalen, G. A. Wiegers, C. Haas, and R. A. de Groot, J. Phys.: Condens. Matter **8**, 5367 (1996).
[47] C. M. Fang, A. R. H. F. Ettema, C. Haas, G. A. Wiegers, H. van Leuken, and R. A. de Groot, Phys. Rev. B **52**, 2336 (1995).
[48] Y. Ohno, Phys. Rev. B **44**, 1281 (1991).
[49] A. R. H. F. Ettema and C. Haas, J. Phys.: Condens. Matter **5**, 3817 (1993).
[50] A. R. H. F. Ettema, G. Wiegers, and C. Haas, Surf. Sci. **269–270**, 1161 (1992).
[51] R. Eppinga, G. Wiegers, and C. Haas, Physica B **105**, 174 (1981).
[52] J. Dijkstra, E. A. Broekhuizen, C. F. van Bruggen, C. Haas, R. A. de Groot, and H. P. van der Meulen, Phys. Rev. B **40**, 12111 (1989).
[53] R. Eppinga, G. Sawatzky, C. Haas, and C. van Bruggen, J. Phys. C: Solid State Phys. **9**, 3371 (1976).
[54] Y. Moëlo, A. Meerschaut, J. Rouxel, and C. Auriel, Chem. Mater. **7**, 1759 (1995).
[55] M. Garbrecht, E. Spiecker, K. Tillmann, and W. Jäger, Ultramicroscopy **111**, 245 (2011).
[56] G. Wiegers, A. Meetsma, R. Haange, S. van Smaalen, and J. de Boer, Acta Cryst. **B46**, 324 (1990).
[57] S. Onari and T. Arai, Sol. Stat. Commun. **31**, 577 (1979).
[58] D. Powell and R. Jacobson, J. Solid State Chem. **37**, 140 (1981).
[59] K. Nagao, M. Koyano, S. Katayama, Y. Yamamura, and T. Tsuji, Phys. Stat. Sol. (b) **223**, 281 (2001).
[60] C. Lee, H. Yan, L. E. Brus, T. F. Heinz, J. Hone, and S. Ryu, ACS Nano **4**, 2695 (2010).
[61] M. Staiger, R. Gillen, N. Scheuschner, O. Ochedowski, F. Kampmann, M. Schleberger, C. Thomsen, and J. Maultzsch, Phys. Rev. B **91**, 195419 (2015).

Acknowledgements

I would like to thank the many people who contributed to this thesis in various ways.

- First of all Prof. Dr. Christian Thomsen, who gave me the opportunity to do exciting science in his wonderful working group. Thank you for the academic supervision, the insightful and to-the-point discussions and for giving me the freedom and independence to develop my own ideas and follow through with them.
- Prof. Dr. Janina Maultzsch for being my co-supervisor, for always finding time to support me with whatever questions I had, for thoroughly reading all my manuscripts and for the persistent motivation even after I had left the group.
- Prof. Dr. Reshef Tenne for the close collaboration with his group at the Weizmann Institute of Science, for inviting me to Israel, and for his ability boost motivation with just a few encouraging words.
- Konstantin Gartsman for the continuous collaboration and for the numerous ideas and discussions we had during the visits in Berlin and Israel.
- Gal Radovsky for providing me with samples, for his dedicated work especially in the field of misfit layer nanotubes and for being the person I most closely worked together with.
- Vladimir Bačić for his theoretical work and ideas in the last stage of my thesis that helped me to get closer to deciphering the structures and properties of misfit layer nanotubes.
- My fellow PhD students and members of the working group, especially Patrick May, Jan Laudenbach, Nils Scheuschner and René Meinke, with whom I shared an office with. Thank you for the perfect atmosphere both on a professional and on a personal level.
- Hagen Telg for being the person to show me around and introducing me to the PhD world during the first months of my time at the institute.
- Roland Gillen for big parts of the theoretical calculations and Felix Kampmann and Emanuele Poliani for the support on the atomic force microscopic measurements.
- Anja Sandersfeld not only for handling all the bureaucratic matters but also for the nice chats whenever there was time.
- And last but not least Cora Rott for her patience, her encouragement and for pushing me towards the end of this thesis.

Eidesstattliche Erklärung

Hiermit erkläre ich, dass ich die vorgelegte Dissertation selbständig und ohne unzulässige fremde Hilfe angefertigt und verfasst habe, dass alle Hilfsmittel und sonstigen Hilfen angegeben und dass alle Stellen, die ich wörtlich oder dem Sinne nach aus anderen Veröffentlichungen entnommen habe, kenntlich gemacht worden sind; ferner, dass die Dissertation in der vorgelegten oder einer ähnlichen Fassung noch nicht zu einem früheren Zeitpunkt an der Technischen Universität Berlin oder einer anderen in- oder ausländischen Hochschule als Dissertation eingereicht worden ist.

(Matthias Staiger)

List of Figures

Bibliography

[1] J. Wilson and A. Yoffe, "The transition metal dichalcogenides discussion and interpretation of the observed optical, electrical and structural properties", Adv. Phys. **18**, 193–335 (1969).

[2] M. Fisher and M. Sienko, "Stoichiometry, Structure, and Physical Properties of Niobium Disulfide", Inorg. Chem. **19**, 39–43 (1980).

[3] D. Powell and R. Jacobson, "The Crystal Structure of 3-R $Nb_{1.06}S_2$", J. Solid State Chem. **37**, 140–143 (1981).

[4] M. Garbrecht, E. Spiecker, K. Tillmann, and W. Jäger, "Quantitative atom column position analysis at the incommensurate interfaces of a $(PbS)_{1.14}NbS_2$ misfit layered compound with aberration-corrected HRTEM", Ultramicroscopy **111**, 245–250 (2011).

[5] G. Radovsky, R. Popovitz-Biro, M. Staiger, K. Gartsman, C. Thomsen, *et al.*, "Synthesis of Copious Amounts of SnS_2 and SnS_2/SnS Nanotubes with Ordered Superstructures", Angew. Chem. Int. Ed. **50**, 12 316–12 320 (2011).

[6] G. Radovsky, R. Popovitz-Biro, D. Stroppa, L. Houben, and R. Tenne, "Nanotubes from Chalcogenide Misfit Compounds: Sn-S and Nb-Pb-S", Accts. Chem. Res. **47**, 406–416 (2014).

[7] G. Radovsky, R. Popovitz-Biro, and R. Tenne, "Study of tubular structures of the misfit layered compound SnS_2/SnS", Chem. Mater. **24**, 3004–3015 (2012).

[8] G. Wiegers, A. Meetsma, R. Haange, S. van Smaalen, J. de Boer, *et al.*, "The Incommensurate Misfit Layer Structure of $(PbS)_{l.14}NbS_2$, $PbNbS_3$ and $(LaS)_{1.14}NbS_2$, 'LaNbS3': an X-ray Diffraction Study", Acta Cryst. **B46**, 324–332 (1990).

[9] G. Wiegers and A. Meerschaut, "Misfit layer compounds $(MS)_nTS_2$ (M=Sn,Pb,Bi, rare earth metals; T=Nb,Ta,Ti,V,Cr; 1.08<n<1.23): structures and physical properties", Mater. Sci. Forum **100-101**, 101–172 (1992).

[10] A. Jobst and S. van Smaalen, "Intersubsystem chemical bonds in the misfit layer compounds $(LaS)_{1.13}TaS_2$ and $(LaS)_{1.14}NbS_2$", Acta Cryst. B **58**, 179–190 (2002).

[11] J. Rouxel, A. Meerschaut, and G. Wiegers, "Chalcogenide misfit layer compounds", J. Alloys Compd. **229**, 144–157 (1995).

[12] D. Bernaerts, S. Amelinckx, G. V. Tendeloo, and J. V. Landuyt, "Microstructure and formation mechanism of cylindrical and conical scrolls of the misfit layer compounds $PbNb_nS_{2n+l}$", J. Cryst. Growth **172**, 433–439 (1997).

[13] G. Wiegers, "Misfit layer compounds: structures and physical properties", Prog. Solid St. Chem. **24**, 1–139 (1996).

[14] R. Eppinga and G. Wiegers, "A generalized scheme for niobium and tantalum dichalcogenides intercalated with post-transition elements", Physica B **99**, 121–127 (1980).

[15] R. Mitchell, Y. Fujiki, and Y. Ishizawa, "Structural polytypism of SnS_2", Nature **247**, 537–538 (1974).

[16] S. v. Smaalen, A. Meetsma, G. Wiegers, and J. de Boer, "Determination of the Modulated Structure of the Inorganic Misfit Layer Compound $(PbS)_{1.18}TiS_2$", Acta Cryst. B **47**, 314–325 (1991).

[17] M. Kalläne, "Towards Angle and Space Resolved Photoemission: Bonding in Layered Misfit Compounds and Development of Reflective Photon Sieves", Dissertation (2007).

[18] A. Lafond, C. Deudon, A. Meerschaut, and A. Sulpice, "X-ray structure determination and magnetic properties of a new misfit layered compound - yttrium chromium sulfide - $(Y_{0.93}[]_{0.07}S)1.28CrS_2$, journal = Eur. J. Solid State Inorg. Chem.", **31**, 967–978 (1994).

[19] J. Wulff, A. Meetsma, R. Haange, J. de Boer, and G. Wiegers, "Structure and electrical transport properties of the misfit-layer compound $(BiS)_{1.08}TaS_2$", Synth. Met. **39**, 1–12 (1990).

[20] M. Hangyo, K. Kisoda, T. Nishio, S. Nakashima, T. Terashima, and N. Kojima, "Staging and interlayer interaction in the misfit-layer compounds $(RS)_nNbS_2$ (R =La,Ce; n=0.6, 1.2) studied by Raman and infrared spectroscopies, journal = Phys. Rev. B", **50**, 12 033–12 043 (1994).

[21] S. Iijima, "Helical microtubules of graphitic carbon", Nature **354**, 56–58 (1991).

[22] R. Tenne, L. Margulis, M. Genut, and G. Hodes, "Polyhedral and cylindrical structures of tungsten disulphide", Nature **360**, 444–446 (1992).

[23] R. Tenne and G. Seifert, "Recent Progress in the Study of Inorganic Nanotubes and Fullerene-Like Structures", Annu. Rev. Mater. Res. **39**, 387–413 (2009).

[24] G. Seifert, T. Köhler, and R. Tenne, "Stability of Metal Chalcogenide Nanotubes", J. Phys. Chem. B **106**, 2497–2501 (2002).

[25] Y. Zhu, W. Hsu, H. Terrones, N. Grobert, B. Chang, *et al.*, "Morphology, structure and growth of WS_2 nanotubes", J. Mater. Chem. **10**, 2570–2577 (2000).

[26] M. Krause, M. Viršek, M. Remškar, N. Salacan, N. Fleischer, *et al.*, "Diameter and morphology dependent Raman signatures of WS_2 nanostructures", ChemPhysChem **10**, 2221–2225 (2009).

[27] L. Scheffer, R. Rosentzveig, A. Margolin, R. Popovitz-Biro, G. Seifert, S. Cohen, and R. Tenne, "Scanning tunneling microscopy study of WS_2 nanotubes", Phys. Chem. Chem. Phys. **4**, 2095–2098 (2002).

[28] M. Remškar, Z. Škraba, M. Regula, C. Ballif, R. Sanjinés, and F. Lévy, "New Crystal Structures of WS_2: Microtubes, Ribbons, and Ropes", Adv. Mater. **10**, 246–249 (1998).

[29] M. Remškar, Z. Škraba, C. Ballif, R. Sanjinés, and F. Lévy, "Stabilization of the rhombohedral polytype in MoS_2 and WS_2 microtubes: TEM and AFM study", Surf. Sci. **433-435**, 637–641 (1999).

[30] M. Remškar, "Inorganic Nanotubes", Adv. Mat. **16**, 1497–1504 (2004).

[31] A. Margolin, R. Rosentsveig, A. Albu-Yaron, R. Popovitz-Biro, and R. Tenne, "Study of the growth mechanism of WS_2 nanotubes produced by a fluidized bed reactor", J. Mater. Chem. **14**, 617–624 (2004).

[32] M. B. Sadan, L. Houben, A. Enyashin, G. Seifert, and R. Tenne, "Atom by atom: HRTEM insights into inorganic nanotubes and fullerene-like structures", Proc. Nat. Acad. U. S. A. **105**, 15 643–15 648 (2008).

[33] M. B. Sadan, M. Heidelmann, L. Houben, and R. Tenne, "Inorganic WS_2 nanotubes revealed atom by atom using ultra-high resolution transmission electron microscopy", Appl. Phys. A **96**, 343–348 (2009).

[34] A. Rothschild, R. Popovitz-Biro, O. Lourie, and R. Tenne, "Morphology of Multiwall WS_2 Nanotubes", J. Phys. Chem. B **104**, 8976–8981 (2000).

[35] K. Tibbetts, R. Doe, and G. Ceder, "Polygonal model for layered inorganic nanotubes", Phys. Rev. B **80**, 014 102 (2009).

[36] M. Krause, A. Mücklich, A. Zak, G. Seifert, and S. Gemming, "High resolution TEM study of WS_2 nanotubes", Phys. Status Solidi B **248**, 2716–2719 (2011).

[37] L. Houben, A. Enyashin, Y. Feldman, R. Rosentsveig, D. Stroppa, and M. Bar-Sadan, "Diffraction from Disordered Stacking Sequences in MoS_2 and WS_2 Fullerenes and Nanotubes", J. Phys. Chem. C **116**, 24 350–24 357 (2012).

[38] H. Deniz and L.-C. Qin, "Determination of the chiral indices of tungsten disulfide (WS_2) nanotubes by electron diffraction", Chem. Phys. Lett. **552**, 92–96 (2012).

[39] M. Remškar, Z. Škraba, P. Stadelmann, and F. Lévy, "Structural Stabilization of New Compounds: MoS_2 and WS_2 Micro- and Nanotubes Alloyed with Gold and Silver", Adv. Mater. **12**, 814–818 (2000).

[40] R. Rosentsveig, A. Margolin, Y. Feldmann, R. Popovitz-Biro, and R. Tenne, "Bundles and foils of WS_2 nanotubes", Appl. Phys. A **74**, 367–369 (2002).

[41] S. Hong, R. Popovitz-Biro, Y. Prior, and R. Tenne, "Synthesis of SnS_2/SnS Fullerene-like Nanoparticles: A Superlattice with Polyhedral Shape", J. Am. Chem. Soc. **125**, 10 470–10 474 (2003).

[42] A. Yella, E. Mugnaioli, H. Therese, M. Panthöfer, U. Kolb, and W. Tremel, "Bismuth-Catalyzed Growth of SnS_2 Nanotubes and Their Stability", Angew. Chem. Int. Ed. **48**, 6426–6430 (2009).

[43] A. Yella, E. Mugnaioli, H. Therese, M. Panthöfer, U. Kolb, and W. Tremel, "Synthesis of Fullerene- and Nanotube-Like SnS_2 Nanoparticles and Sn/S/Carbon Nanocomposites", Chem. Mater. **21**, 2474–2481 (2009).

[44] R. Hazen and L. Finger, "The crystal structures and compressibilities of layer minerals at high-pressure. I. SnS_2, Berndtite", Am. Mineral. **63**, 289–292 (1978).

[45] L. Panchakarla, G. Radovsky, L. Houben, R. Popovitz-Biro, R. Dunin-Borkowski, and R. Tenne, "Nanotubes from Misfit Layered Compounds: A New Family of Materials with Low Dimensionality", J. Phys. Chem. Lett. **5**, 3724–3736 (2014).

[46] G. Radovsky, R. Popovitz-Biro, and R. Tenne, "Nanotubes from the Misfit Layered Compounds MS-TaS_2, Where M = Pb, Sn, Sb, or Bi: Synthesis and Study of Their Structure", Chem. Mater. **26**, 3757–3770 (2014).

[47] A. Geim and K. Novoselov, "The rise of graphene", Nat. Mater. **6**, 183–191 (2007).

[48] M. Chhowalla, H. Shin, G. Eda, L.-J. Li, K. Loh, and H. Zhang, "The chemistry of two-dimensional layered transition metal dichalcogenide nanosheets", Nat. Chem. **5**, 263–275 (2013).

[49] R. Friend and A. Yoffe, "Electronic properties of intercalation complexes of the transition metal dichalcogenides", Adv. Phys. **36**, 1–94 (1987).

[50] A. Reshak and S. Auluck, "Electronic and optical properties of the 1T phases of TiS_2, $TiSe_2$, and $TiTe_2$", Phys. Rev. B **68**, 245 113 (2003).

[51] C. Julien, M. Eddrief, I. Samaras, and M. Balkanski, "Optical and electrical characterization of SnSe, SnS_2 and $SnSe_2$ single crystals", Mater. Sci. Eng. **B15**, 70–72 (1992).

[52] A. Kuc, N. Zibouche, and T. Heine, "Influence of quantum confinement on the electronic structure of the transition metal sulfide TS_2", Phys. Rev. B **83**, 245 213 (2011).

[53] M. Leroux, M. L. Tacon, M. Calandra, L. Cario, M.-A. Méasson, *et al.*, "Anharmonic suppression of charge density waves in 2H-NbS_2", Phys. Rev. B **86**, 155 125 (2012).

[54] J. Kačmarčik, Z. Pribulová, C. Marcenat, T. Klein, P. Rodière, L. Cario, and P. Samuely, "Specific heat measurements of a superconducting NbS_2 single crystal in an external magnetic field: Energy gap structure", Phys. Rev. B **82**, 014 518 (2010).

[55] R. Coehoorn, C. Haas, J. Dijkstra, C. Flipse, R. de Groot, and A. Wold, "Electronic structure of $MoSe_2$, MoS_2, and WSe_2. I. Band-structure calculations and photoelectron spectroscopy", Phys. Rev. B **35**, 6195–6202 (1987).

[56] L. Panchakarla, L. L. R. Popovitz-Biro, R. Tenne, and R. Arenal, "Atomic Structural Studies on Thin Single-Crystalline Misfit-Layered Nanotubes of TbS-CrS_2", J. Phys. Chem. C **120**, 15 600–15 607 (2016).

[57] H. Jiang, "Electronic Band Structures of Molybdenum and Tungsten Dichalcogenides by the GW Approach", J. Phys. Chem. C **116**, 7664–7671 (2012).

[58] C. Ballif, M. Regula, P. Schmid, M. Remškar, R. Sanjinés, and F. Lévy, "Preparation and characterization of highly oriented, photoconducting WS_2 thin films", Appl. Phys. A **62**, 543–546 (1996).

[59] K. Kam and A. Parkinson, "Detailed Photocurrent Spectroscopy of the Semiconducting Group VI Transition Metal Dichalcogenides", J. Phys. Chem. **86**, 463–467 (1982).

[60] D. Braga, I. G. Lezama, H. Berger, and A. Morpurgo, "Quantitative Determination of the Band Gap of WS_2 with Ambipolar Ionic Liquid-Gated Transistors", Nano Lett. **12**, 5218–5223 (2012).

[61] A. Klein, S. Tiefenbacher, V. Eyert, C. Pettenkofer, and W. Jaegermann, "Electronic band structure of single-crystal and single-layer WS_2: Influence of interlayer van der Waals interactions", Phys. Rev. B **64**, 205 416 (2001).

[62] R. Coehoorn, C. Haas, and R. de Groot, "Electronic structure of $MoSe_2$, MoS_2, and WSe_2. II. The nature of the optical band gaps", Phys. Rev. B **35**, 6203–6206 (1987).

[63] F. L. C. Ballif, M. Regula, "Optical and electrical properties of semiconducting WS_2 thin films: From macroscopic to local probe measurements", Sol. Energ. Mat. Sol. **57**, 189–207 (1999).

[64] L. Schmidt, "Superconductivity in $PbNbS_3$ and $PbTaS_3$", Phys. Lett. A **31**, 551–552 (1970).

[65] W. Sterzel and J. Horn, "Thiotitanat, Thiozirkonat und Thiohafnat des Bleis mit der Zusammensetzung $PbMe^{IV}S_3$", Z. Anorg. Allgem. Chem. **376**, 254–260 (1970).

[66] L. Cario, D. Johrendt, A. Lafond, C. Felser, A. Meerschaut, and J. Rouxel, "Stability and charge transfer in the misfit compound $(LaS)(SrS)_{0.2}CrS_2$: Ab initio band-structure calculations", Phys. Rev. B **55**, 9409–9414 (1997).

[67] G. Wiegers, "Charge transfer between layers in misfit layer compounds", J. All. Comp. **219**, 152–156 (1995).

[68] P. Bongers, C. van Bruggen, J. Koopstra, W. Omloo, G. Wiegers, and F. Jellinek, "Structure and magnetic properties of some metal (i) chromium (iii) sulfides and selenides", J. Phys. Chem. Sol. **29**, 977–984 (1968).

[69] C. Auriel, A. Meerschaut, C. Deudon, G. Wiegers, J. Baas, J. Chen, and P. Monceau, "Electrical transport properties of mono- and bilayer misfit compounds $(MX)_{1+x}(TX_2)_m$, M = Sn, Pb; T = Ti, Nb; X = S, Se", Eur. J. Solid State Inorg. Chem. **38**, 565 (1995).

[70] J. Brandt, "Geometric and electronic structure of misfit layered compounds and epitaxial thin films of PbS on transition metal dichalcogenides", Dissertation (2003).

[71] Y. Ohno, "Electronic structure of the misfit-layer compounds $PbTiS_3$ and $SnNbS_3$", Phys. Rev. B **44**, 1281–1291 (1991).

[72] Y. Ohno, "Interlayer interaction in misfit layer compounds MTS_3 (M=Sn, Pb, La; T=Ti, Nb)", Solid State Commun. **79**, 1081–1084 (1991).

[73] A. Ettema, G. Wiegers, and C. Haas, "A LEED and photoemission spectroscopy study of the surface of the incommensurate misfit layer compound $(SnS)_{1.16}TaS_2$", Surface Science **269/270**, 1161–1666 (1992).

[74] A. Ettema and C. Haas, "An x-ray photoemission spectroscopy study of interlayer charge transfer in some misfit layer compounds", J. Phys.: Condens. Matter **5**, 3817–3826 (1993).

[75] A. Ettema, C. Haas, and T. Turner, "Strong multiple resonances in the photoemission spectra of transition-metal-layer and misfit-layer compounds", Phys. Rev. B **47**, 794–805 (1993).

[76] C. Fang, A. Ettema, C. Haas, G. Wiegers, H. van Leuken, and R. de Groot, "Electronic structure of the misfit-layer compound $(SnS)_{1.17}NbS_2$ deduced from band-structure calculations and photoelectron spectra", Phys. Rev. B **52**, 2336–2347 (1995).

[77] J. Brandt, J. Kanzow, K. Roßnagel, L. Kipp, M. Skibowski, *et al.*, "Band structure of the misfit compound $(PbS)NbS_2$ compared to $NbSe_2$: experiment and theory", J. Electron Spectrosc. **114-116**, 555–561 (2001).

[78] J. Brandt, L. Kipp, M. Skibowski, E. Krasovskii, W. Schattke, *et al.*, "Charge transfer in misfit layered compounds", Surf. Sci. **532-535**, 705–710 (2003).

[79] T. Lorenz, J.-O. Joswig, and G. Seifert, "Combined SnSSnS2 double layers: charge transfer and electronic structure", Semicond. Sci. Technol. **29**, 064 006 (2014).

[80] C. Fang, S. van Smaalen, G. Wiegers, C. Haas, and R. de Groot, "Electronic structure of the misfit layer compound $(LaS)_{1.14}NbS_2$: band-structure calculations and photoelectron spectra", J. Phys.: Condens. Mat. **8**, 5367–5382 (1996).

[81] C. Fang, G. Wiegers, and C. Haas, "Photoelectron spectra of the late rare-earth compounds $(LnS)_{1+x}TS_2$ (Ln = Tb, Dy, Ho;T = Nb, Ta)", Physica B **233**, 134–138 (1997).

[82] K. Suzuki, T. Enoki, and H. Tajima, "Optical reflectivity and carrier localization in incommensurate misfit layer compounds $(MS)_xTaS_2$(M =rare-earth metal, Pb, Sn)", Phys. Rev. B **52**, 400–409 (1995).

[83] C. Rüscher, C. Haas, S. van Smaalen, and G. Wiegers, "Investigation of the optical reflectivity of misfit layer compounds: $(MS)_nTS_2$ (T=Ta, Nb; M=Sn,Pb,Sm, Tb, La; $1.08 < n < 1.23$)", Inorg. Chem. **33**, 3358–3363 (1994).

[84] J. Rouxel, Y. Moëlo, A. Lafond, F. DiSalvo, A. Meerschaut, and R. Roesky, "Role of Vacancies in Misfit Layered Compounds: The Case of the Gadolinium Chromium Sulfide Compound", Inorg. Chem. **33**, 3358–3363 (1994).

[85] Y. Ren, J. Baas, A. Meetsma, J. de Boer, and G. Wiegers, "Vacancies and Electron Localization in the Incommensurate Intergrowth Compound $(La_{0.95}Se)_{1.21}VSe_2$", Acta Cryst. **52**, 398–405 (1996).

[86] Y. Moëlo, A. Meerschaut, J. Rouxel, and C. Auriel, "Precise Analytical Characterization of Incommensurate Sandwiched Layered Compounds $[(Pb,Sn)S]_{1+x}[(Nb,Ti)S_2]_m$, ($0.08 \leq x \leq 0.28$, m = 1-3). Role of the Cationic Coupling on the Properties and the Structural Modulation", Chem. Mater. **7**, 1759–1771 (1995).

[87] A. Meerschaut, Y. Moëlo, L. Cario, A. Lafond, and C. Deudon, "Charge Transfer in Misfit Layer Chalcogenides, $[(MX)_n]_{1+x}(TX_2)_m$: a Key for Understanding their Stability and Properties", Mol. Cryst. und Liq. Cryst. **341**, 1–8 (2000).

[88] M. Kalläne, K. Rossnagel, M. Marczynski-Bühlow, L. Kipp, H. Starnberg, and S. Stoltz, "Stabilization of the Misfit Layer Compound $(PbS)_{1.13}TaS_2$ by Metal Cross Substitution", Phys. Rev. Lett. **100**, 065 502 (2008).

[89] E. Kabliman, P. Blaha, and K. Schwarz, "Ab initio study of stabilization of the misfit layer compound $(PbS)_{1.14}TaS_2$", Phys. Rev. B **82**, 125 308 (2010).

[90] S. van Smaalen, "Renormalization of bond valences: application to incommensurate intergrowth crystals", Acta Cryst. A **48**, 408–410 (1992).

[91] R. Eppinga, G. Sawatzky, C. Haas, and C. van Bruggen, "Photoelectron spectra of 2H-TaS_2 and Sn_xTaS_2", J. Phys. C: Solid State Phys. **9**, 3371–3380 (1976).

[92] R. Eppinga, G. Wiegers, and C. Haas, "Photoelectron spectra and transport properties of intercalates of Nb and Ta Dichalcogenides with Sn and Pb", Physica B **105**, 174–178 (1981).

[93] J. Dijkstra, E. Broekhuizen, C. van Bruggen, C. Haas, R. de Groot, and H. van der Meulen, "Band structure, photoelectron spectroscopy, and transport properties of $SnTaS_2$", Phys. Rev. B **40**, 12 111–12 125 (1989).

[94] C. Fang, G. Wiegers, A. Meetsma, R. de Groot, and C. Haas, "Crystal structure and band structure calculations of $Pb_{1/3}TaS_2$ and $Sn_{1/3}NbS_2$", Physica B **226**, 259–267 (1996).

[95] H. Zeng, G.-B. Liu, J. Dai, Y. Yan, B. Zhu, *et al.*, "Optical signature of symmetry variations and spin-valley coupling in atomically thin tungsten dichalcogenides", Sci. Rep. **3**, 1608 (2013).

[96] R. Peierls, "Quelques proprietes typiques des corpses solides", Ann. I. H. Poincaré **5**, 177–222 (1935).

[97] L. Landau, "Zur Theorie der Phasenumwandlungen II.", Phys. Z. Sowjetunion **11**, 26–35 (1937).

[98] K. Novoselov, D. Jiang, F. Schedin, T. Booth, V. Khotkevich, S. Morozov, and A. Geim, "Two-dimensional atomic crystals", Proc. Nat. Acad. Sci. U. S. A. **102**, 10 451–10 453 (2005).

[99] K. Mak, C. Lee, J. Hone, J. Shan, and T. Heinz, "Atomically Thin MoS_2: A New Direct-Gap Semiconductor", Phys. Rev. Lett. **105**, 136 805 (2010).

[100] A. Splendiani, L. Sun, Y. Zhang, T. Li, J. Kim, *et al.*, "Emerging Photoluminescence in Monolayer MoS_2", Nano Lett. **10**, 1271–1275 (2010).

[101] Y. Ding, Y. Wang, J. Ni, L. Shi, S. Shi, and W. Tang, "First principles study of structural, vibrational and electronic properties of graphene-like MX_22 (M = Mo, Nb,W,Ta; X = S, Se,Te) monolayers", Physica B **406**, 2254–2260 (2011).

[102] A. Kumar and P. Ahluwalia, "Effect of quantum confinement on electronic and dielectric properties of niobium dichalcogenides NbX_2 (X = S, Se, Te)", J. Alloy Compd. **550**, 283–291 (2013).

[103] H. Gutiérrez, N. Perea-López, A. Elías, A. Berkdemir, B. Wang, *et al.*, "Extraordinary Room-Temperature Photoluminescence in Triangular WS_2 Monolayers", Nano Lett. **13**, 3447–3454 (2013).

[104] W. Zhao, Z. Ghorannevis, L. Chu, M. Toh, C. Kloc, P.-H. Tan, and G. Eda, "Evolution of Electronic Structure in Atomically Thin Sheets of WS_2 and WSe_2", ACS Nano **7**, 791–797 (2013).

[105] H. Matte, A. Gomathi, A. Manna, D. Late, R. Datta, S. Pati, and C. Rao, "MoS_2 and WS_2 Analogues of Graphene", Angew. Chem. Int. Ed. **122**, 4153–4156 (2010).

[106] T. Li and G. Galli, "Electronic Properties of MoS_2 Nanoparticles", J. Phys. Chem. **111**, 16 192–16 196 (2007).

[107] Z. Zhu, Y. Cheng, and U. Schwingenschlögl, "Giant spin-orbit-induced spin splitting in two-dimensional transition-metal dichalcogenide semiconductors", Phys. Rev. B **84**, 153 402 (2011).

[108] R. Roldán, J. Silva-Guillén, M. López-Sancho, F. Guinea, E. Cappelluti, and P. Ordejón, "Electronic properties of single-layer and multilayer transition metal dichalcogenides MX_2 (M = Mo, W and X = S, Se)", Ann. Phys. **526**, 347–357 (2014).

[109] T. Cheiwchanchamnangij and W. Lambrecht, "Quasiparticle band structure calculation of monolayer, bilayer, and bulk MoS_2", Phys. Rev. B **85**, 205 302 (2012).

[110] T. Heine, "Transition Metal Chalcogenides: Ultrathin Inorganic Materials with Tunable Electronic Properties", Acc. Chem. Res. **48**, 65–72 (2015).

[111] A. Molina-Sánchez, D. Sangalli, K. Hummer, A. Marini, and L. Wirtz, "Effect of spin-orbit interaction on the optical spectra of single-layer, double-layer, and bulk MoS_2", Phys. Rev. B **88**, 045 412 (2013).

[112] A. Hanbicki, M. Currie, G. Kioseoglou, A. Friedman, and B. Jonker, "Measurement of high exciton binding energy in the monolayer transition-metal dichalcogenides WS_2 and WSe_2", Sol. St. Commun. **203**, 16–20 (2015).

[113] A. Ramasubramaniam, "Large excitonic effects in monolayers of molybdenum and tungsten dichalcogenides", Phys. Rev. B **86**, 115 409 (2012).

[114] K. Mak, K. He, C. Lee, G. Lee, J. Hone, T. Hein, and J. Shan, "Tightly bound trions in monolayer MoS_2", Nature Mat. **12**, 207–211 (2013).

[115] K. Hao, L. Xu, P. Nagler, A. Singh, K. Tran, *et al.*, "Coherent and Incoherent Coupling Dynamics between Neutral and Charged Excitons in Monolayer $MoSe_2$", Nano Lett. **16**, 5109–5113 (2016).

[116] G. Plechinger, P. Nagler, J. Kraus, N. Paradiso, C. Strunk, C. Schüller, and T. Korn, "Identification of excitons, trions and biexcitons in single-layer WS_2", Phys. Status Solidi RRL **9**, 457–461 (2015).

[117] G. Plechinger, P. Nagler, A. Arora, R. Schmidt, A. Chernikov, *et al.*, "Trion fine structure and coupled spin-valley dynamics in monolayer tungsten disulfide", Nat. Commun. **7**, 12 715 (2016).

[118] J. Schuller, S. Karaveli, T. Schiros, K. He, S. Yang, *et al.*, "Orientation of luminescent excitons in layered nanomaterials", Nature Nanotech. **8**, 271–276 (2013).

[119] P. Rafailov, C. Thomsen, K. Gartsman, I. Kaplan-Ashiri, and R. Tenne, "Orientation dependence of the polarizability of an individual WS_2 nanotube by resonant Raman spectroscopy", Phys. Rev. B **72**, 205 436 (2005).

[120] L. Benedict, S. Louie, and M. Cohen, "Static polarizabilities of single-wall carbon nanotubes", Phys. Rev. B **52**, 8541–8549 (1995).

[121] G. Seifert, H. Terrones, M. Terrones, G. Jungnickel, and T. Frauenheim, "On the electronic structure of WS_2 nanotubes", Sol. St. Comm. **114**, 245–248 (2000).

[122] G. Seifert, H. Terrones, M. Terrones, G. Jungnickel, and T. Frauenheim, "Structure and Electronic Properties of MoS_2 Nanotubes", Phys. Rev. Lett **85**, 146–149 (2000).

[123] I. Milošević, B. Nikolić, E. Dobardšić, M. Damnjanović, I. Popov, and G. Seifert, "Electronic properties and optical spectra of MoS_2 and WS_2 nanotubes", Phys. Rev B **76**, 233 414 (2007).

[124] N. Zibouche, A. Kuc, and T. Heine, "From layers to nanotubes: Transition metal disulfides TMS_2", Eur. Phys. J. B **85**, 49–55 (2012).

[125] G. Frey, S. Elani, M. Homyonfer, Y. Feldman, and R. Tenne, "Optical-absorption spectra of inorganic fullerenelike MS_2 (M=Mo, W)", Phys. Rev. B **57**, 6666–6671 (1998).

[126] M. Staiger, P. Rafailov, K. Gartsman, H. Telg, M. Krause, *et al.*, "Excitonic resonances in WS_2 nanotubes", Phys. Rev. B **86**, 165 423 (2012).

[127] N. Zibouche, M. Ghorbani-Asl, T. Heine, and A. Kuc, "Electromechanical Properties of Small Transition-Metal Dichalcogenide Nanotubes", Inorganics **2**, 155–167 (2014).

[128] G. Seifert, "On the electronic structure of non carbon nanotubes", AIP Conf. Proc. **544**, 415–418 (2000).

[129] V. Ivanovskaya and G. Seifert, "Tubular structures of titanium disulfide TiS_2", Solid State Comm. **130**, 175–180 (2004).

[130] H. Chang, E. In, K. Kong, J.-O. Lee, Y. Choi, and B.-H. Ryu, "First-Principles Studies of SnS_2 Nanotubes: A Potential Semiconductor Nanowire", J. Phys. Chem. Lett. B **109**, 30–32 (2005).

[131] G. Seifert, H. Terrones, M. Terrones, and T. Frauenheim, "Novel NbS_2 metallic nanotubes", Sol. St. Comm. **115**, 635–638 (2000).

[132] A. Ettema, S. van Smaalen, C. Haas, and T. Turner, "Study of the valency of rare-earth atoms in the misfit layer compound $(RS)_{1+\delta}NbS_2$ (R=La,Ce,Sm) using resonant photoemission and x-ray absorption spectra", Phys. Rev. B **49**, 10 585–10 590 (1994).

[133] M. Staiger, V. Bačić, R. Gillen, G. Radovsky, K. Gartsman, *et al.*, "Raman spectroscopy of misfit layer nanotubes and misfit layer nanotubes", Phys. Rev. B **94**, 035 430 (2016).

[134] H. Telg, J. Duque, M. Staiger, X. Tu, F. Hennrich, *et al.*, "Chiral Index Dependence of the G^+ and G^- Raman Modes in Semiconducting Carbon Nanotubes", ACS Nano **6**, 904–911 (2012).

[135] M. Staiger, R. Gillen, N. Scheuschner, O. Ochedowski, F. Kampmann, *et al.*, "Splitting of monolayer out-of-plane A_1' Raman mode in few-layer WS_2", Phys. Rev. B **91**, 195 419 (2015).

[136] N. Scheuschner, R. Gillen, M. Staiger, and J. Maultzsch, "Interlayer resonant Raman modes in few-layer MoS_2", Phys. Rev. B **91**, 235 409 (2015).

[137] J. Verble and T. Wieting, "Lattice mode degeneracy in MoS_2 and other layer compounds", Phys. Rev. Lett. **25**, 362–365 (1970).

[138] P. Tonndorf, R. Schmidt, P. Böttger, X. Zhang, J. Börner, *et al.*, "Photoluminescence emission and Raman response of monolayer MoS_2, $MoSe_2$, and WSe_2", Optics. Expr. **4**, 4908–4916 (2013).

[139] C. Lee, H. Yan, L. Brus, T. Heinz, J. Hone, and S. Ryu, "Anomalous Lattice Vibrations of Single and Few-Layer MoS_2", ACS Nano **4**, 2695–2700 (2010).

[140] A. Berkdemir, H. Gutiérrez, A. Botello-Méndez, N. Perea-López, A. Elías, *et al.*, "Identification of individual and few layers of WS_2 using Raman Spectroscopy", Sc. Rep. **3**, 1755 (2013).

[141] W. Zhao, Z. Ghorannevis, K. Amara, J. Pang, M. Toh, *et al.*, "Lattice dynamics in mono- and few-layer sheets of WS_2 and WSe_2", Nanoscale **5**, 9677–9683 (2013).

[142] D. Late, B. Liu, H. Matte, C. Rao, and V. Dravid, "Rapid Characterization of Ultrathin Layers of Chalcogenides on SiO_2/Si Substrates", Adv. Funct. Mater. **22**, 1894–1905 (2012).

[143] M. Yamamoto, S. Wang, M. Ni, Y.-F. Lin, S.-L. Li, *et al.*, "Strong Enhancement of Raman Scattering from a Bulk-Inactive Vibrational Mode in Few-Layer $MoTe_2$", ACS Nano **8**, 3895–3903 (2014).

[144] A. Molina-Sánchez and L. Wirtz, "Phonons in single-layer and few-layer MoS_2 and WS_2", Phys. Rev. B **84**, 155 413 (2011).

[145] X. Wang, C. Zheng, and J. Ning, "Influence of curvature strain and Van der Waals force on the interlayer vibration mode of WS_2 nanotubes: A confocal micro-Raman spectroscopic study", Sci. Rep. **6**, 33 091 (2016).

[146] S. Yu, L. Chang, H. Yang, B. Liu, Y. Hou, *et al.*, "Study of the hydrostatic pressure dependence of the Raman spectrum of W/WS_2 fullerene-like nanosphere with core-shell structure", J. Phys.: Condens. Matter **19**, 425 228 (2007).

[147] D. Mead and J. Irwin, "Raman spectra of SnS_2 and $SnSe_2$", Sol. State Comm. **20**, 885–887 (1976).

[148] A. Smith, P. Meek, and W. Liang, "Raman scattering studies of SnS_2 and $SnSe_2$", J. Phys. C: Solid State Phys. **10**, 1321–1333 (1977).

[149] A. Cingolani, M. Lugará, and G. Scamarcio, "Second-Order Raman Scattering and Infrared Absorption in SnS_2", Il Nuovo Cimento **10**, 519–528 (1988).

[150] C. Julien, H. Mavi, K. Jain, M. Balkanski, C. Perez-Vicente, and J. Morales, "Resonant Raman scattering studies of SnS_2 crystals", Mater. Sc. Eng. **B23**, 98–104 (1994).

[151] G. Lucovsky, J. Mikkelsen, W. Liang, R. White, and R. Martin, "Optical phonon anisotropies in the layer crystals SnS_2 and $SnSe_2$", Phys. Rev. B **14**, 1663–1669 (1976).

[152] H. Chandrasekhar, R. Humphreys, U. Zwick, and M. Cardona, "Infrared and Raman spectra of IV-VI compuds SnS and SnSe", Phys. Rev. B **15**, 2177–2183 (1977).

[153] P. Nikolić, L. Miljković, P. Mihajlović, and B. Lavrenčic, "Splitting and coupling of lattice modes in the layer compound SnS", J. Phys. C: Solid State Phys. **10**, 289–292 (1977).

[154] G. Radovsky, R. Popovitz-Biro, M. Staiger, K. Gartsman, C. Thomsen, *et al.*, "Synthesis of Copious Amounts of SnS_2 and SnS_2/SnS Nanotubes with Ordered Superstructures: Supporting Information", Angew. Chem. Int. Ed. **50**, 12 316–12 320 (2011).

[155] K. Trentelmann, "A note on the characterization of bismuth black by Raman microspectroscopy", J. Raman Spectrosc. **40**, 585–589 (2009).

[156] S. Nakashima, H. Katahama, and A. Mitsuishi, "The effect of polytypism on the vibrational properties of SnS_2", Physica B **105**, 343–346 (1981).

[157] P. Klipstein, C. Pereira, and R. Friend, "Transport and Raman studies of the group IV layered compounds and their lithium intercalates: Li_xTiS_2, Li_xTiSe_2, Li_xZrS_2, Li_xZrSe_2, Li_xHfS_2 and Li_xHfSe_2", Philos. Mag. B **56**, 531–559 (1987).

[158] C. Julien and C. Perez-Vicente, "Vibrational studies of lithium-intercalated SnS_2", Solid State Ionics **89**, 337–343 (1996).

[159] S. Nakashima, Y. Tokuda, and A. Mitsuishi, "Raman scattering from 2H-NbS_2 and intercalated NbS_2", Sol. Stat. Commun. **42**, 601–604 (1982).

[160] M. Hangyo, S. Nakashima, Y. Hamada, T. Nishio, and Y. Ohno, "Raman scattering from the misfit-layer compounds $SnNbS_3$, $PbNbS_3$, and $PbTiS_3$", Phys. Rev. B **48**, 11 291–11 297 (1993).

[161] M. Hangyo, T. Nishio, S. Nakashima, Y. Ohno, T. Terashima, and N. Kojima, "Raman and Infrared Spectra of Misfit Layer Compounds $MNbS_3$ (M=Sn, Pb, La, Ce)", Jpn. J. Appl. Phys. Suppl. **32**, 581–583 (1993).

[162] M. Hangyo, K. Kisoda, S. Nakashima, A. Meerschaut, and J. Rouxel, "Stage dependence of phonons in misfit layer compounds $(MS)(NbS_2)_n$ (M = Sn,Pb; n = 1,2)", Physica B **219/220**, 481–483 (1996).

[163] K. Kisoda, M. Hangyo, S. Nakashima, K. Suzuki, T. Enoki, and Y. Ohno, "Raman scattering from misfit layer compounds $(RS)_xTaS_2$ (R = La, Ce, Sm or Gd; S = sulphur; x≈1.2)", J. Phys.: Condens. Matter **7**, 5383–5393 (1995).

[164] K. Kisoda, M. Hangyo, S. Nakashima, T. Terashima, and N. Kojima, "Charge transfer and phonons in misfit layer compounds $(RS)_xNbS_2$ (R = rare earth; x≈1.2)", Physica B **219/220**, 565–567 (1996).

[165] K. Kisoda, M. Hangyo, J. Kuroda, H. Harima, and S. Nakashima, "Optical reflection and Raman studies on mixed crystals of misfit layer compounds", Sol. St. Comm. **103**, 597–602 (1997).

[166] K. Nagao, M. Koyano, S. Katayama, Y. Yamamura, and T. Tsuji, "Raman Scattering from Intercalation Compounds Fe_xNbS_2 under High Pressure", Phys. Status Solidi B **223**, 281–285 (2001).

[167] S. Ovsyannikov, V. Shchennikov, A. Cantarero, A. Cros, and A. Titov, "Raman spectra of $(PbS)_{1.18}(TiS_2)_2$ misfit compound", Mater. Sci. Eng. A **462**, 422–426 (2007).

[168] C. Pereira and W. Liang, "Raman study of iron-intercalated niobium selenide", J. Phys. C: Solid State Phys. **18**, 6075–6082 (1985).

[169] K. Shirai, K. Kisoda, M. Hangyo, and S. Nakashima, "On the Raman shift in misfit layer compounds of metal-dichalcogenides $(MX)(TX_2)$ - an effect of the charge transfer on the intralayer noncentral forces", Sol. St. Comm. **103**, 131–135 (1997).

[170] S. Onari, T. Arai, R. Aoki, and S. Nakamura, "Raman scattering in 3R-NbS_2", Sol. Stat. Commun. **31**, 577–579 (1979).

[171] W. McMullan and J. Irwin, "Raman scattering from 2H and 3R-NbS_2", Sol. Stat. Commun. **45**, 557–560 (1983).

[172] W. McMullan and J. Irwin, "An Interpolytypical Transition in NbS_2", Phys. Status Solidi B **129**, 465–469 (1985).

[173] V. Bačić, private communication.

[174] G. Radovsky, R. Popovitz-Biro, T. Lorenz, J.-O. Joswig, G. Seifert, *et al.*, "Tubular structures from the LnS-TaS_2 (Ln=La, Ce, Nd, Ho, Er) and LaSe-$TaS2_2$ misfit layered compounds", J. Mat. Chem. C **4**, 89–98 (2016).

[175] L. Panchakarla, R. Popovitz-Biro, L. Houben, R. Dunin-Borkowski, and R. Tenne, "Lanthanide-Based Functional Misfit-Layered Nanotubes", Angew. Chem. Int. Ed. **53**, 6920–6924 (2014).

[176] K. O'Neal, J. Cherian, A. Zak, R. Tenne, Z. Liu, and J. Musfeldt, "High Pressure Vibrational Properties of WS_2 Nanotubes", Nano Lett. **16**, 993–999 (2016).

[177] C. Raman and K. Krishnan, "A New Type of Secondary Radiation", Nature **121**, 501–502 (1928).

[178] C. Raman, "A Change of Wave-length in Light Scattering", Nature **121**, 619–619 (1928).

[179] P. Yu and M. Cardona, *Fundamentals of Semiconductors Physics and Materials Properties* (Springer, 2010).